

**NOVEL METHODS OF DIMENSIONALITY REDUCTION  
APPLIED TO A TWO-DIMENSIONAL FLUID FLOW**

A Thesis  
Presented to  
The Academic Faculty

by

Jeffrey Tithof

In Partial Fulfillment  
of the Requirements for the Degree  
Doctor of Philosophy in the  
School of Physics

Georgia Institute of Technology  
August 2016

Copyright © 2016 by Jeffrey Tithof

# **NOVEL METHODS OF DIMENSIONALITY REDUCTION APPLIED TO A TWO-DIMENSIONAL FLUID FLOW**

Approved by:

Professor Michael F. Schatz, Advisor  
School of Physics  
*Georgia Institute of Technology*

Professor Konstantin Mischaikow  
School of Mathematics  
*Rutgers University*

Professor Predrag Cvitanović  
School of Physics  
*Georgia Institute of Technology*

Professor Kurt Wiesenfeld  
School of Physics  
*Georgia Institute of Technology*

Professor Peter Yunker  
School of Physics  
*Georgia Institute of Technology*

Date Approved: 20 June 2016

*To my wife, Sarah*

## Acknowledgments

There are several people I would like to acknowledge who together have made my graduate school experience tremendously rewarding, both professionally and personally. I am very grateful for the opportunity to have worked under the guidance of my advisor, Mike Schatz. Mike has been a tremendous mentor who is very effective in guiding his students to become successful scientists. Mike is a natural leader, and his patience and passion for science provide a nurturing environment for professional development. I deeply appreciate the numerous opportunities Mike has provided for interacting with the wider scientific community, and his emphasis on the importance of knowing your audience and communicating ideas simply and clearly are invaluable lessons. I am also very fortunate for the opportunity to have worked so closely with Roman Grigoriev, who in many ways has been my co-advisor. Roman has a clear vision for how to perform high-quality, successful scientific research, and his physical intuition is unparalleled. Roman is also a wonderful teacher whose pattern formation class was one of the best classes I've ever taken.

The fellow graduate students in our research group have helped provide an enjoyable and productive work atmosphere. Bala Suri, who I have worked with side-by-side since day one, is a deep thinker and has proven to be a great friend who can find humor in any situation. Bala's contributions to our research have been tremendous. Daniel Borrero has always been a great mentor and friend; his immense patience and knowledge helped tremendously in my first few years of grad school. Radford Mitchell is one of the most unique and interesting people I've ever met and a great source for dozens of funny stories. Sam Raben taught me a great amount about PIV and was a good running buddy in the evenings. Chris Crowley has been an excellent addition to the lab and his knowledge of metrology has proven tremendously useful. It has been a pleasure to collaborate with Ravi Pallantla in research, and I look forward to

seeing his future accomplishments on this project. Finally, Michael Krygier has been a good friend and a valuable part of our research group.

Our homology group has been an exemplary source of fruitful discussion and an ideal interdisciplinary collaboration. Konstantin Mischaikow's ability to illustrate abstract mathematical concepts and his encouragement of the exploration of new ideas have been crucial assets. We've always been able to count on Mark Paul for his physical insight and comprehensive knowledge of pattern formation. Miro Kramár has been relied upon often as a source of mathematical intuition and knowledge, Mu Xu has been a vital and very reliable part of the team, and Jacek Cyranka has brought some additional mathematical rigor to the group. Finally, Rachel Levanger has been a very hard-working and enthusiastic collaborator who has consistently received our data on a Friday afternoon but still had results ready for discussion in our Monday morning Skype meetings.

I've had several enjoyable interactions with many faculty members. Predrag Cvitanović was always a source of wisdom and dry wit. Jim Gole kept us on our toes on the 3rd floor. Ed Greco always had funny stories and was an excellent mentor for TAs. I also would like to thank the faculty members who served on my thesis committee, including Kurt Wiesenfeld and Peter Yunker.

My family and friends have been a tremendous source of love and support throughout my graduate career. I am forever grateful to my mother for instilling in me a love of science from the time I was a small child. My sisters, Kristen and Taylor, are two of the funniest people I know who have been a tremendous source of emotional support. My mother- and father-in-law, Marjorie and Bill Lacy, have been incredibly kind and supportive. I'd like to thank Josh Lester and Patrick Fox for their loyal friendship throughout this headlong flight. I've made close friends with several fellow grad students over the past 6 years. Notably, Matt Kinsey and I had some great times as roommates, and Martin Anquez was always a great lunch, gym, and concert

buddy. Finally, I would like to thank my wife Sarah for her unwavering love and support, patience when “just 20 more minutes” turned into 2 more hours, and general tolerance of my research-induced mood swings. I very much look forward to the next chapter of our lives together in Rochester, New York.

## TABLE OF CONTENTS

<b>DEDICATION</b> . . . . .	iii
<b>ACKNOWLEDGMENTS</b> . . . . .	iv
<b>LIST OF TABLES</b> . . . . .	x
<b>LIST OF FIGURES</b> . . . . .	xi
<b>SUMMARY</b> . . . . .	xviii
<b>I INTRODUCTION</b> . . . . .	1
1.1 Turbulent Flows are Chaotic and High-Dimensional . . . . .	1
1.2 Insight from Chaos Theory . . . . .	3
1.3 A Low-Dimensional Description of Turbulence . . . . .	4
1.4 Dimensionality Reduction Methods for Characterizing Turbulence . .	6
1.4.1 Time Delay Embedding . . . . .	6
1.4.2 Proper Orthogonal Decomposition . . . . .	7
1.4.3 Exact Coherent Structures . . . . .	9
1.4.4 Topological Data Analysis . . . . .	10
1.5 Thesis Organization . . . . .	11
<b>II BACKGROUND</b> . . . . .	12
2.1 Exact Coherent Structures . . . . .	12
2.1.1 Overview of ECS . . . . .	12
2.1.2 Previous Work in 3D Periodic Domains . . . . .	14
2.1.3 Previous and Present Work in 2D Domains . . . . .	15
2.2 Persistent Homology . . . . .	16
2.2.1 Computational Homology . . . . .	16
2.2.2 Overview of Persistent Homology . . . . .	18
2.2.3 Previous and Present Work . . . . .	23
2.3 Experiments in Quasi-Two-Dimensional Flows . . . . .	24
2.3.1 Kolmogorov flow . . . . .	25

2.3.2	Setup Variations in Thin Electrolyte Layers . . . . .	26
2.3.3	How Two-Dimensional Are Flows in Thin Electrolyte Layers? . . . . .	28
<b>III</b>	<b>EXPERIMENTAL REALIZATION AND MODELING OF KOLMOGOROV-LIKE FLOW . . . . .</b>	<b>30</b>
3.1	Experimental Realization . . . . .	30
3.1.1	Constructing the Experimental Apparatus . . . . .	30
3.1.2	Setting Up the Experiment . . . . .	34
3.1.3	Constant Current Control Circuit . . . . .	38
3.1.4	Measuring the Experimental Velocity Fields . . . . .	40
3.1.5	Verification of Quasi-Two-Dimensionality . . . . .	42
3.2	Theoretical Modeling . . . . .	43
3.2.1	Discussion of the Model Derivation . . . . .	43
3.2.2	Nondimensionalization . . . . .	47
3.2.3	Velocity Profile in Two Immiscible Layers . . . . .	48
3.2.4	Evaluation of Parameters from Experimental Quantities . . .	51
3.3	Numerical Modeling . . . . .	51
3.3.1	Magnetic Field Modeling . . . . .	51
3.3.2	Boundary Conditions for Direct Numerical Simulations . . .	54
<b>IV</b>	<b>PRIMARY AND SECONDARY INSTABILITIES OF KOLMOGOROV-LIKE FLOW . . . . .</b>	<b>57</b>
4.1	Straight Flow . . . . .	59
4.2	Linear Stability Analysis . . . . .	60
4.3	Primary Instability and Modulated Flow . . . . .	63
4.4	Secondary Instability and Time-Periodic Flow . . . . .	67
4.5	Discussion . . . . .	70
<b>V</b>	<b>EXACT COHERENT STRUCTURES IN WEAKLY TURBULENT KOLMOGOROV-LIKE FLOW . . . . .</b>	<b>72</b>
5.1	Weakly Turbulent Dynamics . . . . .	72
5.2	Calculating Unstable Equilibria . . . . .	76

5.3	Forecasting Weak Turbulence . . . . .	78
5.4	Discussion . . . . .	83
<b>VI</b>	<b>APPLICATION OF PERSISTENT HOMOLOGY . . . . .</b>	<b>86</b>
6.1	The Dynamical Regimes Studied . . . . .	86
6.2	Generating and Interpreting PDs . . . . .	87
6.3	Applying Metrics to the Space of PDs . . . . .	94
6.3.1	Comparing Flow Fields . . . . .	95
6.3.2	Estimating the Number of Changes in Small-Scale and Large-Scale Features . . . . .	96
6.3.3	Measuring the Rate of Evolution . . . . .	99
6.4	Analyzing a Point Cloud . . . . .	101
6.4.1	Introduction to the Analysis of Point Clouds . . . . .	102
6.4.2	Distinguishing Flow Fields . . . . .	110
6.4.3	Identifying Periodic Dynamics . . . . .	112
6.5	Discussion . . . . .	114
<b>VII</b>	<b>CONCLUSIONS . . . . .</b>	<b>116</b>
<b>APPENDIX A</b>	<b>— PARTICLE IMAGE VELOCIMETRY . . . . .</b>	<b>121</b>
<b>APPENDIX B</b>	<b>— UNIDIRECTIONAL FLOW . . . . .</b>	<b>129</b>
<b>APPENDIX C</b>	<b>— NUMERICAL METHODS . . . . .</b>	<b>133</b>
<b>BIBLIOGRAPHY . . . . .</b>		<b>153</b>

## LIST OF TABLES

6.1	Distances between selected persistence diagrams (rounded to 3 decimal places) in Figure 6.5, corresponding to the vorticity fields shown in Figure 6.4. . . . .	96
6.2	The coordinate of the dominant point in the persistence diagram $\text{PD}_1(X, d_*)$ for $*$ = $B, W^2, W^1$ , its life span, and the second largest life span. . .	114

## LIST OF FIGURES

1.1	(a) An example 2D flow field resolved by $n \times m$ vectors, and (b) a high-dimensional vector which can be used to specify the flow field shown in (a). The color contour in (a) corresponds to the vorticity, and is only included for visualization purposes. . . . .	3
1.2	A cartoon showing a turbulent trajectory evolving in state space. . .	5
2.1	(a) A cartoon showing a turbulent trajectory (black line) which visits the neighborhoods of ECS embedded in or near the inertial manifold. Here the red circles represent unstable equilibria, which are the simplest class of ECS. (b) A network of heteroclinic connections (red lines) between ECS, which guide the evolution of the chaotic trajectory. . .	13
2.2	Example 1D and 2D patterns with Betti numbers (a) $\beta_0 = 2$ , (b) $\beta_0 = 9$ , (c) $\beta_0 = 4$ , $\beta_1 = 3$ , and (d) $\beta_0 = 42$ , $\beta_1 = 8$ . . . . .	17
2.3	Example 3D shapes that when analyzed using homology yield the following Betti numbers: (a) $\beta_0 = 1$ , $\beta_1 = 1$ , and $\beta_2 = 0$ for an open ended cylinder, (b) $\beta_0 = 1$ , $\beta_1 = 0$ , $\beta_2 = 1$ for a hollow sphere, and (c) $\beta_0 = 1$ , $\beta_1 = 2$ , $\beta_2 = 1$ for a hollow torus. . . . .	18
2.4	A 1D function (left) with three local minima and three local maxima. The critical points are paired as indicated to form three points in the persistence diagram (right). This figure is adapted from reference [1].	20
2.5	An example illustrating how persistent homology handles noisy data. (a) Smooth and noisy 1D functions shown in black and red, respectively. (b) The PDs superimposed on top of each other with the same color convention as the functions. Notice that the dominant far-from-diagonal points do not change much, but the red function generates several additional points near the diagonal which correspond to the noisy features. . . . .	21
2.6	An illustration of how distances are computed between PDs. (a) Two PDs represented by red circles and blue squares, with black lines indicating the least cost bijection. (b) A graphical representation of all possible bijections (gray lines) and the most efficient bijections (black lines). Any point on a PD can be matched to the diagonal, denoted $\Delta$ . This figure is adapted from reference [2]. . . . .	22

3.1 A schematic diagram of the two-immiscible-layer Kolmogorov-like flow experimental setup viewed (a) from above and (b) from the transverse cross section. The fluid flow is driven by Lorentz forces arising from the interaction of a direct current density  $\mathbf{J}$ , which is passed through the electrolyte in the  $y$ -direction, with a spatially varying magnetic field  $\mathbf{B}$  pointed in the  $\pm z$ -direction, generated by an array of permanent magnets located below the fluid layers (dashed lines in (a); black and white rectangles in (b)). The resulting forcing  $\mathbf{F}$  is in the  $\pm x$ -direction. The flow is bounded by two end walls, two side walls (electrodes), and a solid, bottom surface, while the top surface of the fluid is a free electrolyte-air interface. This container is mounted on an aluminum plate which is leveled and submerged in a water bath that is regulated such that the electrolyte is maintained at  $23^\circ\text{C} \pm 0.2^\circ\text{C}$ . . . . . 33

3.2 An image of the calibration grid placed inside the flow domain allows for careful optical alignment and a coordinate transformation from pixels to cm. The red circles and blue squares indicate the pairs of cross hairs which are used for determining the pixel-to-cm scaling constant. . . . . 36

3.3 (a) A schematic diagram of the elementary component of the constant current control circuit. By adjusting the resistance  $R$  of the  $1\text{ k}\Omega$  digipot (AD8400) using MATLAB, the voltage regulator (LM317) produces a constant output current of  $\mathcal{I} = 1.25\text{ V}/R$ . (b) A plot showing the current through the experimental apparatus as a function of the wiper position for an elementary component of the circuit. . . . . 39

3.4 An illustration of the velocity profile in the two-immiscible-layer configuration. Under the Q2D approximation, the full 3D velocity  $\mathbf{v}(x, y, z, t)$  can be decomposed as the 2D in-plane velocity at the free surface  $\mathbf{u}(x, y, t)$  times a 1D profile  $P(z)$ . . . . . 45

3.5 Magnetic field measurements (black circles) taken above the center of the magnet array at height  $z = 0.394$ , which corresponds to roughly the middle of the electrolyte layer. A sinusoidal fit to the data, shown by the black curve, suggests that the magnetic field is indeed close to sinusoidal here. Uncertainties are the size of the symbols or smaller. . . . . 49

3.6 (a) Analytical results for the vertical profile of the horizontal flow field in both layers. The ratio of the velocities, as defined by equation (3.13), is  $S = 1.08$ . (b) Experimental measurements of the horizontal flow profile taken separately at the electrolyte free surface (red circles) and at the electrolyte-dielectric interface (blue squares). PIV measurements are plotted for the time-independent laminar flow near the center of the magnet array. A sine wave with fixed periodicity is fit to each data set. In both (a) and (b),  $h_d = h_e = 0.236$  and the electrolyte layer has viscosity  $\mu_e = 6.06\text{ mPa}\cdot\text{s}$ . Uncertainties in (b) are the size of the symbols or smaller. . . . . 50

3.7	(a) Experimental measurements of the $z$ -component of the magnetic field, $B_z$ , as a function of $y$ at the longitudinal center of the domain ( $x = 0$ ), and (b) experimental measurements of $B_z$ along the magnet centerlines at $y = \pm\{0.5, 1.5, 2.5, 3.5, 4.5, 5.5, 6.5\}$ . Measurements in (a) are taken at a height just above the dielectric-electrolyte interface at $z = 0.236$ and just below the electrolyte free surface at $z = 0.472$ . A least-squares fit has been performed using the data in (a) to determine the scaling factor for the dipole summation; the scaled dipole summation magnetic field is shown in red. The experimental uncertainties are the size of the symbols or smaller. . . . .	53
4.1	Straight flow fields at $Re = 8.1$ for the (a) DPS, (b) SPS, (c) NPS, and (d) experiment. The dashed lines in (d) indicate the locations of velocity profiles that are compared to the simulations in Figure 4.2. The vorticity color scale plotted for (a) also applies to (b-d). The velocity vectors are downsampled in each direction by a factor of 8 for the simulations and a factor of 4 for the experiment. . . . .	58
4.2	Profiles of the longitudinal velocity and longitudinal velocity differences at $Re = 8.1$ . (a) $u_x^{exp}$ as a function of $y$ at the longitudinal center ( $x = 0$ ), (b) the difference between the longitudinal velocity in the simulations and the experiment, $u_x^{sim} - u_x^{exp}$ , as a function of $y$ at the longitudinal center ( $x = 0$ ); note that the curves corresponding to the DPS and SPS are virtually indistinguishable, (c) $u_x^{exp}$ as a function of $x$ at the centerline of a middle magnet ( $y = -0.5$ ), and (d) the difference between the longitudinal velocity of the simulations and the experiment, $u_x^{sim} - u_x^{exp}$ , as a function of $x$ at the centerline of a middle magnet ( $y = -0.5$ ); note that the curves corresponding to the DPS and SPS are virtually indistinguishable in the region $ x  < 4$ , where the DPS is defined. Experimental uncertainties are the size of the symbols or smaller. . . . .	61
4.3	Neutral stability curves (4.1) showing the Reynolds number $Re_n$ at which the straight flow in an unbounded domain goes unstable when subjected to a perturbation of longitudinal wavenumber $q$ . The red dashed line corresponds to $\alpha = 0.064 \text{ s}^{-1}$ and $\beta = 1.00$ , while the blue dot-dashed line corresponds to $\alpha = 0.064 \text{ s}^{-1}$ and $\beta = 0.83$ . The black circle shows the corresponding measurement from the experiment. In all cases, $\bar{\nu} = 3.26 \times 10^{-6} \text{ m}^2/\text{s}$ is held constant. . . . .	63
4.4	Modulated flow fields at $Re = 14$ for the (a) DPS, (b) SPS, (c) NPS, and (d) experiment. The vorticity color scale plotted for (a) also applies to (b-d). The velocity vectors are downsampled in each direction by a factor of 8 for the simulations and a factor of 4 for the experiment. . . . .	65

4.5	(a) A bifurcation diagram showing the primary instability for the experiment and simulations, and (b) the spatial average of the longitudinal wavelength, $\bar{\lambda}_x$ , as a function of $Re$ for the modulated flow regime. At each $Re$ , wavelength measurements are made for $ y  < 4$ then averaged; the uncertainty bars indicate one standard deviation in the spatial measurements. . . . .	66
4.6	(a) A bifurcation diagram showing the power spectrum peak intensity $I$ as a function of $Re$ , and (b) the temporal power spectrum $P$ as a function of the frequency $f$ for the experiment (top) and NPS (bottom) as $Re$ is increased. The temporal power spectrum is averaged over the region $ x  < 4$ and $ y  < 4$ before calculating the intensity $I$ . This transition, which occurs at $Re_s = 17.6$ in the experiment and $Re_s = 17.0$ in the NPS, corresponds to the flow transitioning from the modulated flow to a time-periodic flow. . . . .	68
4.7	Two snapshots of the experimental (left) and NPS (right) flow fields in the time-periodic regime. The vorticity color scale plotted for (b) also applies to (a). The velocity vectors are downsampled in each direction by a factor of 8 for the simulations and a factor of 3 for the experiment.	69
5.1	Four sequential weakly turbulent flow fields from the experiment, separated by $\Delta t = 8.0$ . . . . .	74
5.2	The spatially-averaged power spectrum for a long (1 hour) experimental time series. . . . .	75
5.3	The experimental velocity field autocorrelation function $C(\Delta t)$ . . . . .	75
5.4	The rate of flow evolution, $s(t) = \ \partial\mathbf{u}/\partial t\ $ , as a function of normalized time, in the experiment. . . . .	77
5.5	Three experimental snapshots (left column) which correspond to local minima of $s(t)$ ; when used as initial conditions for a Newton solver, each flow field converges to an unstable equilibrium (right column). . . . .	79
5.6	The vorticity field associated with the seven eigenfunctions of the unstable equilibrium used for forecasting. (a) The leading real eigenfunction, (b-c) the real and imaginary part of the first complex conjugate pair, (d-e) the real and imaginary part of the second complex conjugate pair, (f-g) the real and imaginary part of the third complex conjugate pair. . . . .	81
5.7	A projection showing an unstable equilibrium (red sphere) with its dominant unstable submanifold (red curve). Both the experimental (blue curve) and numerical (green curve) turbulent trajectories follow this submanifold as they depart from the neighborhood of this unstable equilibrium. . . . .	82

5.8 Representative flow fields from the experimental turbulent trajectory (left column), 1D dominant submanifold (middle column), and the numerical turbulent trajectory (right column) at three different instances of time separated by about $0.7\tau$ . Each instance is indicated in Figure 5.7 by (a) a circle, (b) a triangle, and (c) a square. . . . .	84
6.1 (a) Three-dimensional projections of a stable RPO at $Re = 23.55$ from the DPS using the imaginary part of the three dominant Fourier modes, $I_1$ , $I_2$ , and $I_3$ . The gray line indicates the evolution of a RPO; three snapshots sampled from that orbit are indicated by a red diamond, a red circle, and a red square, which are analyzed below. (b) Three-dimensional projections of a turbulent trajectory, at $Re = 24.90$ , using the real parts of the three dominant Fourier modes, $R_1$ , $R_2$ , and $R_3$ . The gray line indicates the chaotic evolution of the flow, which is influenced by the presence of unstable equilibria, indicated by red circles, which are also analyzed below. . . . .	88
6.2 A snapshot of the $z$ -component of the vorticity field $\omega$ for the Kolmogorov-like flow DPS. This flow field is sampled from the stable relative periodic orbit found at $Re = 23.55$ . . . . .	89
6.3 (a-d) Sublevel sets $C(\omega, \theta) = \{x \in D : \omega(x) \leq \theta\}$ of the vorticity field shown in Figure 6.2, for different values of $\theta$ , depicted in black. (e) $PD_0(\omega)$ and (f) $PD_1(\omega)$ persistence diagrams of the vorticity field indicate the values of $\theta$ at which the connected components and holes appear and disappear (merge together). Every point $(\theta_b, \theta_d)$ in the $PD_0(\omega)$ ( $PD_1(\omega)$ ) persistence diagram corresponds to a connected component (hole) that is present in every set $C(\omega, \theta)$ , for $\theta_b \leq \theta < \theta_d$ . A connected component disappears by merging with a previously existing component and a hole disappears when it is filled in. . . . .	91
6.4 Three snapshots of the vorticity fields $\omega$ from the stable RPO of the Kolmogorov-like flow found at $Re = 23.55$ . The vorticity fields correspond to the (a) diamond, (b) square, and (c) circle in Figure 6.1 (a). The persistence diagrams for these three snapshots are generated and compared in Figure 6.5. Differences between the persistence diagrams are qualitatively measured by the distances shown in Table 6.1. . . .	96
6.5 $PD_0$ persistence diagrams $PD^a$ , $PD^b$ , and $PD^c$ for the vorticity fields shown in Figure 6.4. The points in $PD^a$ and $PD^b$ are almost identical because the corresponding vorticity fields are related by a symmetry operation. The points in $PD^c$ are more spread out and do not resemble the points in $PD^a$ as well. The same is true for the $PD_1$ persistence diagrams. Consequently, $d_*(PD^a, PD^b) < d_*(PD^a, PD^c)$ , for $* \in \{B, W^2, W^1\}$ , as indicated by Table 6.1. . . . .	97
6.6 Contributions to the $d_{W^1}(PD^a, PD^c)$ distance. . . . .	98

6.7	The speed $s_*$ , estimated from the distances $d_*$ between the consecutive sample points along the stable RPO, plotted for almost four periods. Distances are normalized by their maximum value which is 0.0654 for $d_B$ , 0.2266 for $d_{W2}$ , and 1.9143 for $d_{W1}$ . The speed is not uniform along the orbit. Instead, there are parts of the orbit where the dynamics are slow, separated by relatively fast evolution. . . . .	100
6.8	A distance matrix $\mathcal{M}$ , generated by the $d_{W2}$ metric, for approximately three periods of the stable RPO. The large black patches correspond to the parts of the orbit with slow dynamics. Equally spaced black lines parallel to the diagonal suggest periodicity of the orbit with period equal to the distance between these lines. . . . .	101
6.9	(a) A distance matrix representing the pairwise Euclidean distances $d_E$ between the points in (b), which is a point cloud $X$ . (c-e) The balls (blue shaded regions) indicate the sublevel sets $C(X, \theta)$ for $\theta = 0, 0.1755, 0.5135$ , and $0.816$ , while the points, lines, and triangles indicate the Vietoris-Rips complexes $R(X, \theta)$ . For $\theta = 0.1755$ , as shown in (c), the set $C(g, \theta)$ consist of three distinct connected clusters; the same is true for $R(X, \theta)$ . The three components remain distinct until $\theta = 0.5135$ , shown in (d), at which point two components of $C(g, \theta)$ merge and a line connecting the points in the merged components appears in $R(X, \theta)$ . The last merger occurs at $\theta = 0.816$ , as shown in (e). . . . .	104
6.10	Persistence diagram $PD_0(X, d_E)$ corresponding to the distance matrix shown in Figure 6.9 (a). . . . .	105
6.11	(a) A distance matrix representing the pairwise Euclidean distances $d_E$ between the points in (b), which is a point cloud $X$ . (c-e) Sets $C(f, \theta)$ for $\theta = 0, 0.177, 0.343$ , and $0.596$ . The homology of $C(f, \theta)$ can be approximated using the Vietoris-Rips complex $R(X, \theta)$ given by the points, lines, and triangles shown in (b-e). The first hole in $C(f, \theta)$ is created at $\theta = 0.177$ (corresponding to (c)). This hole is due to the noisy sampling and is filled in almost immediately. The dominant hole is born at $\theta = 0.343$ (corresponding to (d)) and persists until $\theta = 0.596$ (corresponding to (e)). . . . .	107
6.12	Persistence diagrams (a) $PD_0(X, d_E)$ and (b) $PD_1(X, d_E)$ corresponding to the distance matrix in Figure 6.11 (a). The persistence diagram $PD_1(X, d_E)$ contains a dominant point $(0.343, 0.596)$ corresponding to the robust loop whose birth is shown in Figure 6.11 (d), while the point $(0.177, 0.25)$ represents the small loop whose birth is shown in Figure 6.11 (c). . . . .	108

- 6.13 (a) Pairwise  $d_B$  distances between the EQ and REQ points in  $X = \{\text{PD}(\omega_n) \mid n = 1, \dots, 67\}$  found at  $Re = 24.90$  using a Newton solver.  
 (b) The corresponding persistence diagram  $\text{PD}_0(X, d_B)$  shows a clear gap between the points with death value  $\theta_d = 0.1215$  and  $\theta_d = 0.0285$ . This gap is interpreted as the separation between the signal and noise. . . . . 111
- 6.14 (a) The persistence diagram  $\text{PD}_0(X, d_B)$  for RPO at  $Re = 24.90$ . Since all points with finite death coordinates die before 0.025, there is only a single dominant point. (b) The persistence diagram  $\text{PD}_1(X, d_B)$ , showing the single dominant generator at  $(0.0215, 0.1559)$ . . . . . 113
- B.1 Analytical results for the vertical profile of the horizontal flow field in both layers, with  $h_d = h_e = 0.236$ . The Kolmogorov flow corresponds to the solid line, while the unidirectional flow corresponds to the dashed line. The ratios of the velocities, as defined by equation (3.13), are:  $S = 1.10$  for unidirectional flow and  $S = 1.08$  for Kolmogorov flow. . . . . 131

## SUMMARY

Fluid turbulence is ubiquitous in nature and technology. Despite the fact that fluid flows are governed by the deterministic Navier-Stokes equation, turbulent phenomena are notoriously difficult to characterize and predict. The difficulty largely arises because turbulence is chaotic, i.e., it exhibits extreme sensitivity to initial conditions; practical limitations in knowing the precise initial conditions render long-term predictions impossible. Furthermore, turbulent flows have a very large number of degrees of freedom because of their continuous dependence on space and time. However, a growing body of recent research suggest that turbulent dynamics are effectively low-dimensional. Hence, an effective tool is needed which can both perform dimensionality reduction and offer insight into the inherent chaos of turbulent flows.

In this dissertation, two methods of dimensionality reduction are explored in the context of a quasi-two-dimensional (Q2D) fluid flow. This Q2D flow can be treated as effectively 2D, making the experimental and numerical aspects of the study more tractable than that of a fully three-dimensional flow. The first method explored involves the calculation of exact, unstable solutions of the Navier-Stokes equation. These solutions, often called “exact coherent structures” (ECS), exist in the same parameter regime as turbulence and play an important role in guiding the dynamics. In this work, experimental evidence for the existence and dynamical relevance of ECS is provided, as well as the first experimental demonstration of how ECS can be used to forecast weak turbulence. The second method, known as “persistent homology,” provides a powerful mathematical formalism in which unique geometric features of a flow field are encoded in a so-called “persistence diagram.” Persistence diagrams exist

in a well-defined metric space which enables one to make quantitative comparisons between flow fields. The results herein demonstrate how persistent homology can be used to characterize individual flow fields, make pairwise comparisons, and identify dynamical structures in ensembles of data. The substantial progress presented in this dissertation suggests that Q2D flows provide an excellent platform for testing new approaches to understanding turbulence.

# CHAPTER I

## INTRODUCTION

Fluid turbulence is a ubiquitous phenomenon present over a vast range of scales, from the airflow around a hummingbird’s wings to the oceanic currents that make up the Gulf Stream. Such flows are characterized by the irregular motion of eddies and vortices (i.e., swirling flow structures) across different length and time scales. Due to its universal presence throughout nature and technology, turbulence has been studied for hundreds of years. In fact, in 1507 Leonardo da Vinci was the first person to refer to swirling fluids as “la turbolenza” [3, 4]. In 1822, Claude Navier derived the Navier-Stokes equation which governs incompressible fluids. Despite the nearly 200 years that the equation governing fluid flows has been known, turbulence still remains a very active area of scientific and engineering research today.

### 1.1 *Turbulent Flows are Chaotic and High-Dimensional*

The Navier-Stokes equation for an incompressible fluid ( $\nabla \cdot \mathbf{v} = 0$ ) is given by:

$$\partial_t \mathbf{v} + \mathbf{v} \cdot \nabla \mathbf{v} = -\frac{1}{\rho} \nabla p + \nu \nabla^2 \mathbf{v} + \frac{1}{\rho} \mathbf{F}, \quad (1.1)$$

where  $\mathbf{v} = (v_x, v_y, v_z)$  is the three-dimensional (3D) velocity,  $\rho$  is the density of the fluid under consideration,  $p$  is the pressure,  $\nu$  is the kinematic viscosity, and  $\mathbf{F}$  is the force per unit volume. The Navier-Stokes equation is *deterministic* in that once a set of parameters and initial conditions are specified, the evolution of the flow is completely determined. Nevertheless, the Navier-Stokes equation is challenging to solve because of its *nonlinearity*, which appears in the *advection* term  $\mathbf{v} \cdot \nabla \mathbf{v}$  and is associated with the fluid’s inertia. As a consequence of this nonlinearity, one cannot find an analytic solution that describes the evolution of turbulent flow. In

particular, because of this nonlinearity, solutions of the Navier-Stokes equation may exhibit *chaos*. Chaos refers to extreme sensitivity to initial conditions, in which two identical systems evolving from very similar initial conditions will eventually diverge to vastly different states. Since infinite precision in determining initial conditions is not possible in real world scenarios (due to, e.g., numerical truncation or experimental uncertainty), long-term prediction of chaotic evolution is considered impossible. The atmosphere is a common example of a system for which weather forecasting is limited due to the chaotic nature of turbulence.

In addition to exhibiting chaos, turbulent fluid flows are *high-dimensional*. This high-dimensionality does not refer to the four (three spatial plus one temporal) dimensions that fluid flows evolve in, but rather their continuous dependence on space and time which gives rise to a high number of degrees of freedom. Consider, for example, a snapshot of a fluid flow shown in Figure 1.1 (a). Suppose this flow field is confined to two spatial dimensions in the  $x - y$  plane for the sake of simplicity, and that a grid of  $n \times m$  vectors adequately resolves all features of the flow. Then, one can construct a vector composed of the  $x$ - and  $y$ -components of velocity at each point in space, which is represented in Figure 1.1 (b). This vector would then have  $2 \times n \times m$  components, where in principle each component is a degree of freedom. For flows realized in the laboratory, this dimensionality is often of order  $10^5$  or even much higher.

In fact, the dimensionality of a fluid flow grows with the *Reynolds number*,  $Re$ . The Reynolds number is the dimensionless ratio of inertial forces to viscous forces in a fluid flow [5]. When  $Re$  is small, the damping effects of viscosity dominate, and the flow is smooth and regular. As  $Re$  is increased, however, inertial effects take over and fluid flows become turbulent. Scaling arguments show that the dimensionality of a fluid flow grows quickly, as  $Re^{9/4}$  [6]. Due to this very high dimensionality, even at moderate  $Re$ , characterization of turbulence is a challenging task for scientists and

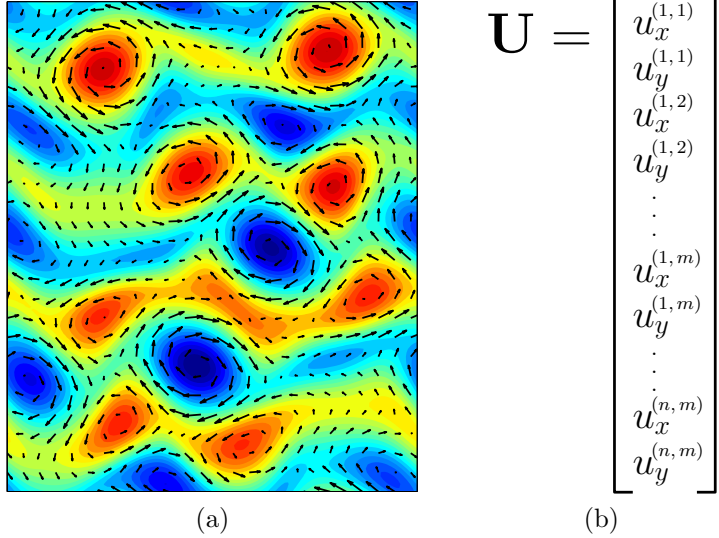


Figure 1.1: (a) An example 2D flow field resolved by  $n \times m$  vectors, and (b) a high-dimensional vector which can be used to specify the flow field shown in (a). The color contour in (a) corresponds to the vorticity, and is only included for visualization purposes.

engineers. When coupled with the fact that such flows are chaotic, the development of a framework for forecasting and controlling turbulence poses a tremendous challenge.

## 1.2 *Insight from Chaos Theory*

The development of chaos theory, beginning in the 1970s, has led to the understanding that complicated, aperiodic dynamics are not necessarily random, but often arise from nonlinearities in the governing equations of a system. The framework of chaos has helped explain the aperiodic dynamics observed in chemical reactions [7], lasers [8], oscillators [9–11], and cardiac cells [12], to name just a few examples from nature and technology. Nonlinear models exhibiting chaos have also offered unique insight into population dynamics [13, 14] and economic fluctuations [15]. Methods for predicting the evolution of a chaotic time series have been developed [16, 17], and even techniques for controlling chaos have been proposed [18] and experimentally demonstrated [19, 20]. All of these aforementioned studies, however, have focused on *low-dimensional* systems.

At the same time that chaos theory was finding great success with low-dimensional systems, there was a substantial scientific effort to use this newfound framework to explain fluid turbulence. In an influential article published in 1971 [21], Ruelle & Takens predicted that fluid turbulence could develop through the appearance of a chaotic “strange attractor” after a series of just three bifurcations (bifurcations are qualitative changes in a system’s behavior as some control parameter – usually  $Re$  for fluids – is varied). In general, the term “attractor” is used to describe the asymptotic dynamical behavior of a system; for example, the attractor for a swinging pendulum with friction is an equilibrium, while the attractor for a swinging pendulum without friction is a periodic state. The term “strange attractor” was introduced by Ruelle & Takens because the asymptotic dynamics are chaotic. A few years later, Gollub & Swinney experimentally confirmed this prediction in a study of Taylor-Couette flow (the flow between two independently-rotating cylinders) [22]. In the following years, more routes to chaos were discovered [23, 24] and several more examples of fluid flows at low  $Re$  have emerged which exhibit the chaotic behavior typical of low-dimensional nonlinear systems [25–27].

### ***1.3 A Low-Dimensional Description of Turbulence***

A growing body of evidence supports the notion that it may be possible to describe turbulence using much lower-dimensional models. This possibility was perhaps first recognized by Eberhard Hopf in a seminal paper published in 1948 [28], in which Hopf invokes the *state space* representation of turbulence. Before discussing Hopf’s radical insight on turbulence, this alternate description of turbulent dynamics is introduced.

In the state space picture of turbulence, each flow field corresponds to a unique point in a high-dimensional state space. This concept builds on the discussion surrounding Figure 1.1, i.e., the vector shown in Figure 1.1 (b) represents a specific flow field and can be thought of as the set of coordinates for a unique point in state space.

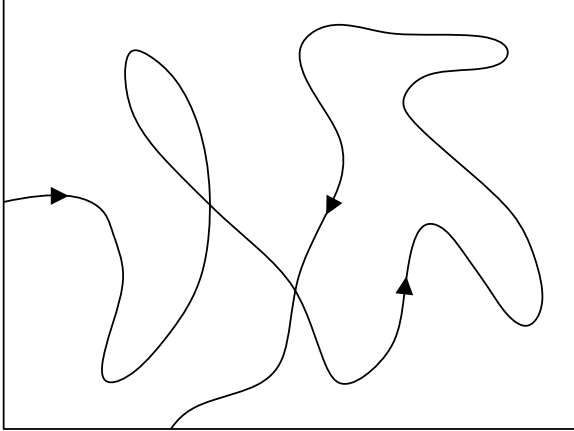


Figure 1.2: A cartoon showing a turbulent trajectory evolving in state space.

One can imagine that as a given flow field smoothly evolves in time, the corresponding components of the vector continuously change. By plotting the sequence of points from this continuously changing vector in state space, a smooth, winding trajectory is swept out. The winding trajectory, which is an equivalent representation of the evolution of the turbulent flow, is henceforth referred to as a *turbulent trajectory* in state space. A two-dimensional (2D) cartoon representing a turbulent trajectory is shown in Figure 1.2. This representation of turbulence is convenient for visualization purposes and will be used often throughout this dissertation.

Naïvely, one may expect that a turbulent trajectory aimlessly wanders throughout the entirety of state space. However, Hopf's conjecture was that not all regions of state space are visited, but rather a fluid's viscosity contracts the turbulent dynamics onto a finite-dimensional *inertial manifold*. A manifold is a topological space which is locally Euclidean, so this inertial manifold is a finite-dimensional, smooth object in state space which contains the global attractor of the system. In this picture, the simple laminar state which a fluid exhibits at low  $Re$  corresponds to a single point comprising the inertial manifold in state space. As  $Re$  is increased, the size of the inertial manifold grows and a strange attractor may appear leading to chaotic dynamics. The prospect of exploiting the low-dimensionality of an inertial manifold offers tremendous new

insight into turbulent dynamics and the possibility for constructing effective low-dimensional models. However, this framework requires that *dimensionality reduction* be performed. In general, dimensionality reduction refers to any methodology in which the full number of degrees of freedom is reduced to some smaller set which still retains key aspects of the dynamics of the full system. Such methods are discussed in the next section.

## 1.4 Dimensionality Reduction Methods for Characterizing Turbulence

By the start of the 1980s, scientists were investigating how the nature of a low-dimensional strange attractor underlying turbulence could be determined from observations of the actual fluid flow [29, 30]. The technological and computational resources available at the time typically limited experimental data acquisition to a time series of measurements performed at a single point in space. Examples from simulations of low-dimensional chaotic systems demonstrated that analogous single-point samples could be used to reconstruct properties of a strange attractor, such as its dimension [29]. These studies led to the development of the *time delay embedding* for characterizing the low-dimensional dynamics of turbulence.

### 1.4.1 Time Delay Embedding

A mathematical proof, now referred to as Takens' theorem, was published in 1981 [31] demonstrating that the properties of an attractor can be reconstructed from a single time series of some observable  $\phi(t)$ . This methodology utilizes a time delay embedding in which a vector  $\Phi(t) = (\phi(t), \phi(t + \tau), \phi(t + 2\tau), \dots, \phi(t + n\tau))$  is constructed from the time series of data. The time between sample points  $\tau$  is known as the *time delay* and the number of components in the vector (which is equal to  $n + 1$ ) is known as the *embedding dimension*. In general, one chooses a time delay based on some characteristic time scale in the problem, such as an autocorrelation time. Then, for

a sufficiently large embedding dimension, the plot of  $\Phi(t)$  (or a projection if  $\Phi(t)$  is too high-dimensional) may recover the attractor. Algorithms have been developed for using  $\Phi(t)$  to calculate, e.g., the dimension and entropy associated with a strange attractor [32]. For a thorough discussion of the dynamical properties that can be obtained from experimental observations, see the review articles by Eckmann & Ruelle [33] and Sauer, Yorke, & Casdagli [34].

Attractor reconstruction from experimental measurements was first demonstrated for a chaotic chemical reaction in 1980 [35]. In the years since, however, there have been relatively few studies involving turbulent fluid flows. Examples include investigations of Taylor-Couette flow [36, 37], convection [38, 39], and atmospheric boundary-layer turbulence [40]; also worth mentioning is a study of channel flow simulations [41]. The relatively few examples of successful implementation of time delay embeddings is likely due to the numerous difficulties associated with the method. For example, the optimal choice for the time delay is far from obvious, although efforts have been made to address this question [42]. Experimental noise also poses a problem for attractor reconstruction. Several methods have been developed for performing noise reduction [43, 44], but fundamentally, these methods rely on assumptions about the form of the noise, which may not hold. It is also potentially problematic that measurements are occurring at only a single point in space; the implicit assumption is that this point is representative of the dynamics of the full system, which may not be the case. Finally, this methodology is limited to cases where the reduced dimensionality is very low (about 5 or less), as a time delay embedding breaks down if the embedding dimension is too large [45].

#### 1.4.2 Proper Orthogonal Decomposition

Even before chaos theory had emerged, the concept of coherent structures had grown

to become an important research subject among the wider fluid mechanics community [46]. Coherent structures refer to the very general concept of large-scale ordered vortical patterns which are discernible and appear repeatedly in some turbulent flows. Because coherent structures are large-scale and organized, it is reasonable to expect that they play an important role in the turbulent dynamics and can perhaps be captured by low-dimensional models. Hence, by performing some kind of a modal decomposition which captures the coherent portion of the flow, it may be possible to construct low-order models which offer insight into the basic processes driving turbulence. Such a modal decomposition was first introduced in the context of turbulence by John L. Lumley in 1967 [47]. This method is often referred to as proper orthogonal decomposition (POD), although it is sometimes also called principal component analysis or the Karhunen-Loëve decomposition.

POD generates a set of orthogonal basis functions which contain the greatest kinetic energy of a particular ensemble of data (experimental or numerical); these highest-energy features often coincide with the coherent structures of a turbulent flow. Once the set of basis functions is obtained, the Navier-Stokes equation can be projected onto these modes. This projection typically uses a Galerkin method to yield a set of ordinary differential equations (ODEs). These ODEs then provide a low-dimensional deterministic model which is used to explore dynamical behavior. The book by Holmes, Lumley, and Berkooz [48] is an excellent resource explaining this methodology.

POD has formed the basis of several studies aimed at discovering the basic mechanisms which generate turbulence. This methodology has offered physical insight into the generation of turbulent phenomena in boundary layers [49–51], plane Poiseuille flow [52–54], flow past a circular cylinder [55, 56], convection [57], and plane Couette flow [58]. For example, the low-dimensional model studied by Aubry *et al.* [49] was used to demonstrate the mechanism by which “bursting” events (i.e., violent

ejections of low-speed fluid near the wall) occur in boundary layers. These results were directly used to explain observations from pipe flow experiments conducted two decades earlier [59].

POD is still widely used among scientists and engineers for modeling a wide variety of fluid flows throughout nature and technology. The low to moderate computational costs associated these reduced models make POD a very appealing approach. However, despite its prevalence, there are substantial limitations to this methodology. In these reduced models, basing the choice of modes on kinetic energy may not necessarily capture the dynamics that generate a particular ensemble of data, as low-energy features may play an important role. Furthermore, these modes do not relate to the underlying dynamics at a fundamental level. Most importantly, it should be noted that by performing such large truncations, these models only generate qualitative results and thus have a limited scope for use in prediction or control.

#### 1.4.3 Exact Coherent Structures

Further computational improvements leading into the 2000s have allowed for more widespread implementation of direct numerical simulations (DNS) of fluid flows at low to moderate  $Re$ , in which all relevant length and time scales are fully resolved. Such DNS studies, coupled with advances in chaos theory and numerical analysis, have led to the discovery of “exact coherent structures” (ECS), which are sometimes also called “invariant solutions.” ECS are exact, unstable solutions of the Navier-Stokes equation which have regular temporal dependence, meaning they correspond to equilibria, traveling waves, periodic orbits, etc. These solutions can exist in or near the inertial manifold so that when a turbulent trajectory passes close to an ECS, the turbulent flow field transiently appears similar to the flow field associated with the ECS. In a sense, ECS formalize the concept of coherent structures in that they explain why similar patterns seem to repeatedly appear in turbulent flows—the

turbulent trajectory is passing close to the same solutions repeatedly. It is for this reason that Fabian Waleffe [60, 61] introduced the term ECS.

In many ways, ECS form a more natural basis for studying the dynamics of fluid flows than POD modes. It is hypothesized that, in state space, a chaotic system spends a substantial amount of time near such solutions [62]. Furthermore, ECS are saddles in state space, meaning they will attract a turbulent trajectory from some directions and then repel it away along others. The hope is that knowledge of these directions can be exploited to forecast or even control turbulence. Hence, ECS form the basis of a substantial portion of the work presented in this dissertation. A detailed discussion of ECS is provided in Section 2.1, and results from the application of this methodology are presented in Chapter 5.

#### 1.4.4 Topological Data Analysis

A very appealing feature of time delay embeddings is that evidence for a low-dimensional attractor can be obtained *directly from experimental data*. Approaches utilizing POD or exact coherent structures involve numerical simulations and implicitly depend on proper modeling of the flow (e.g., an accurate forcing profile or realistic boundary conditions). The prospect of directly determining dynamical properties of a low-dimensional attractor from experimental observations bypasses the potential difficulties associated with simulations. This brings to mind the newly emerging framework of topological data analysis (TDA), which offers a powerful new tool that is in many ways in the same spirit as the time delay embedding.

TDA refers to a very general class of methodologies in which algebraic topology is used for information extraction. Algebraic topology is the mathematical study of properties of objects that are preserved through deformation, twisting, and stretching. The underlying premise in applying TDA to turbulence is that the dynamics depend on the system's topology, i.e., the interconnectedness of the structures in the flow of

the fluid. The primary tool for quantifying a system’s topology is persistent homology [1, 63], which is a powerful mathematical formalism in which well-defined topological characteristics are plotted as points in a so-called “persistence diagram” (PD). Points in a PD can be interpreted as corresponding to either dominant topological features or “noise” which can be neglected, hence providing dimensionality reduction. In particular, dynamics can be quantified by applying various metrics to PDs, and these associated distances can be used to construct a persistent homology state space. Persistent homology is described in detail in Section 2.2.2 and used as a tool for dimensionality reduction in Chapter 6.

## ***1.5 Thesis Organization***

This dissertation is organized as follows. In Chapter 2, an in-depth introduction to exact coherent structures and persistent homology is presented, as well as motivation and details of the fluid flow that has been analyzed in this work. In Chapter 3, the specific flow configuration, which is known as “Kolmogorov-like flow” is introduced, with an emphasis on reviewing the relevant literature, describing the experimental setup in detail, and explaining the numerical modeling. Chapter 4 provides a comparison of the experiment with the numerical model at low  $Re$  by comparing the primary and secondary bifurcations that are observed. In Chapter 5, a discussion of how ECS can be used for dimensionality reduction of weak turbulence is presented; this chapter also includes the first experimental demonstration of forecasting of weak turbulence using ECS. Chapter 6 covers the application of persistent homology to Kolmogorov-like flow simulations. Finally, Chapter 7 provides a discussion of the conclusions which may be drawn from this work.

## CHAPTER II

## BACKGROUND

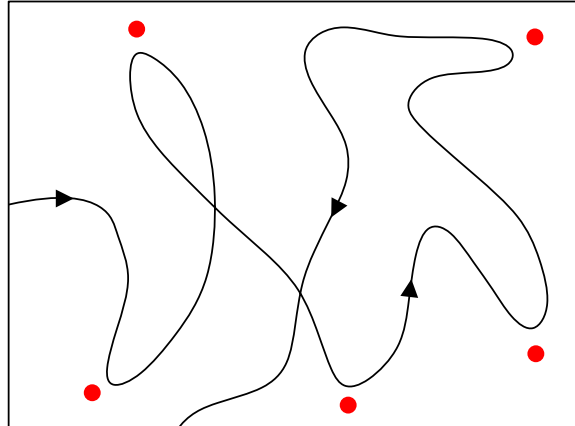
This chapter presents a discussion of the background associated with each of the two dimensionality reduction methods, starting with ECS and followed by persistent homology. In each of these associated sections, motivation for studying Kolmogorov-like flow is provided. Section 2.3 then offers an introduction to Kolmogorov-like flow experiments.

### 2.1 *Exact Coherent Structures*

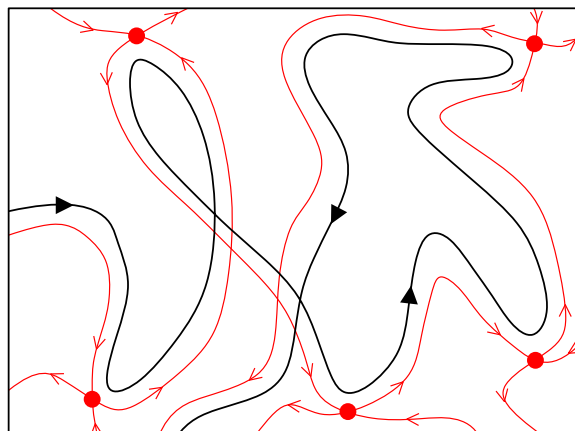
#### 2.1.1 Overview of ECS

To understand the important role ECS play in the dynamics of a turbulent fluid flow, it is convenient to again invoke the state space representation of the dynamics. Recall that Figure 1.2 illustrates a turbulent trajectory in state space, which provides an equivalent representation of the flow field evolving in time. In this example, the trajectory is evolving on the inertial manifold of the system which corresponds to a strange attractor (i.e., the dynamics are chaotic). As the system evolves, the turbulent trajectory transiently visits the neighborhoods of ECS which are embedded in or near the inertial manifold. This picture is illustrated in Figure 2.1 (a), where the red circles represent the simplest class of ECS, unstable equilibria.

The saddle structures of the ECS play a key role in guiding the turbulent trajectory. This saddle structure is illustrated in Figure 2.1 (b), where locally each ECS has stable and unstable manifolds (red lines), i.e., directions which respectively attract and repel a turbulent trajectory. The calculation of such manifolds should allow for forecasting of turbulence over short to moderate time scales. The intersection of the



(a)



(b)

Figure 2.1: (a) A cartoon showing a turbulent trajectory (black line) which visits the neighborhoods of ECS embedded in or near the inertial manifold. Here the red circles represent unstable equilibria, which are the simplest class of ECS. (b) A network of heteroclinic connections (red lines) between ECS, which guide the evolution of the chaotic trajectory.

unstable manifold of one ECS and the stable manifold of another ECS forms a *heteroclinic connection* (if the associated stable and unstable manifold belong to the same ECS, it is a *homoclinic connection*). The calculation of heteroclinic (and homoclinic) connections is expected to allow for forecasting over longer time scales.

The frequency for which each ECS is visited by a turbulent trajectory depends on the stability properties of that particular solution. ECS that are the *least* unstable are visited most often. These least unstable ECS will typically have unstable manifolds with the lowest dimensionality. Hence, the ECS that are the most dynamically-relevant for the evolution of the turbulent trajectory also offer the greatest dimensionality reduction in capturing the dynamics.

### 2.1.2 Previous Work in 3D Periodic Domains

The calculation of a network of ECS and their heteroclinic and homoclinic connections promises tremendous advancements in characterization, forecasting, and perhaps even control of turbulence. However, in practice, finding ECS requires numerical calculations that are so computationally expensive that they have only become possible in the last 15 years or so. Hence, the development of an ECS-based description of turbulence is still in its infancy. The vast majority of studies have been numerical and have focused on calculating ECS in three-dimensional (3D) fluid flows, such as plane Couette flow [64–67], plane Poiseuille flow [61, 68], and pipe flow [69–71]. In particular, these studies have largely focused on transitional and *weakly* turbulent flows at low  $Re$ . They also often use small experimentally-inaccessible flow domains with periodic boundary conditions; for a thorough overview of such calculations, see references [72, 73].

For plane Couette, plane Poiseuille, and pipe flows, periodic boundary conditions are not realizable in experiments. Hence, making direct quantitative comparisons between experiments and these simulations is difficult. For this reason, there have

been very few experimental studies in which ECS have been identified in the laboratory [74–76]. Theoretical studies of manifolds and/or heteroclinic connections are also scarce [77, 78], and there have been no prior experimental validations of their relevance.

The scarcity of experimental evidence for ECS is also due to the significant challenge posed by making temporally and spatially resolved velocity field measurements in 3D. Such measurements require state-of-the-art imaging equipment, careful alignment of multiple cameras, storage of very large amounts of data, and sophisticated algorithms with large computational overhead. Additionally, it is rarely if ever possible to measure the entire flow field simultaneously, and in the case of pipe flow, the ability to track turbulent structures is limited by the finite domain size and open (inflow-outflow) boundary conditions (i.e., the fluid eventually flows out of the end of the pipe).

### 2.1.3 Previous and Present Work in 2D Domains

To circumvent many of the challenges associated with studying 3D flows, the analyses described herein focus on a *quasi-two-dimensional* (Q2D) fluid flow which can be considered effectively 2D from numerical and experimental standpoints. Experimentally, Q2D flows at low  $Re$  offer an appealing test bed for studying ECS because they only require a single camera for performing velocity measurements; this significantly reduces the challenges of collecting, storing, and processing data. Furthermore, the flow fields may easily be observed for arbitrarily long times, which is an attractive feature for testing the forecasting capabilities of ECS. Finally, as will be demonstrated in this dissertation, the experimental Q2D flow can be quantitatively described by a strictly 2D model. This implies that simulations can be performed in 2D, which is another very appealing feature from the computational perspective.

The work presented in this dissertation, however, is not the first to study ECS in

2D. In recent numerical studies by Chandler & Kerswell [79] and Lucas & Kerswell [80, 81], dozens of ECS have been identified in weakly turbulent 2D flows. Specifically, Chandler & Kerswell’s work [79] was called “the most exhaustive study of this programme undertaken so far in fluid dynamics” [82]. Unfortunately, the particular parameters and boundary conditions of these simulations are nonphysical, preventing any possibility of direct comparison with experiments. The details of why these particular parameters and boundary conditions are inaccessible to experiments are highlighted throughout Chapters 3 and 4.

The goal then for the ECS-related work presented in this dissertation is to: (i) introduce a Q2D experiment whose evolution can be described satisfactorily using a strictly 2D equation, (ii) compare results from the experiment with those computed numerically using the 2D model in the preturbulent regimes (low  $Re$ ) as a benchmarking exercise, (iii) provide evidence for the existence and dynamical relevance of ECS in the weakly turbulent regime, and (iv) forecast weak turbulence using the dimensionality reduction offered by ECS.

## ***2.2 Persistent Homology***

### **2.2.1 Computational Homology**

Homology is a branch of algebraic topology which characterizes global geometric properties of patterns in some topological space. The homology of a pattern is described by a set of non-negative integers, known as “Betti numbers,” which describe the connectivity of that pattern. For an  $N$ -dimensional pattern there are  $N$  Betti numbers, denoted  $\beta_k$ , where  $k = 0, 1, 2, \dots, N - 1$ .

Each  $\beta_k$  is associated with a unique topological property of the pattern. The zeroth Betti number,  $\beta_0$ , corresponds to the distinct, connected components. For example, Figure 2.2 (a-b) show two simple, one-dimensional (1D) patterns, for which  $\beta_0 = 2$  and  $\beta_0 = 9$ , respectively. For a 2D pattern, such as those shown in Figure 2.2

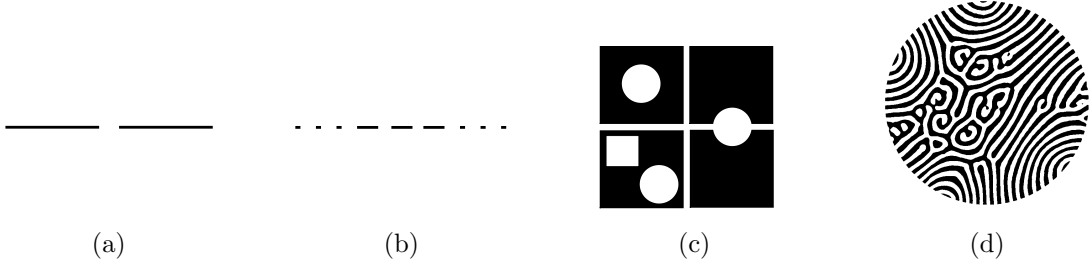


Figure 2.2: Example 1D and 2D patterns with Betti numbers (a)  $\beta_0 = 2$ , (b)  $\beta_0 = 9$ , (c)  $\beta_0 = 4$ ,  $\beta_1 = 3$ , and (d)  $\beta_0 = 42$ ,  $\beta_1 = 8$ .

(c-d), the additional Betti number  $\beta_1$  corresponds to holes (or alternatively loops).

For example, Figure 2.2 (c) has Betti numbers  $\beta_0 = 4$  and  $\beta_1 = 3$ , while for the complicated image in Figure 2.2 (d),  $\beta_0 = 42$  and  $\beta_1 = 8$ . For 3D patterns, the additional Betti number  $\beta_2$  corresponds to cavities. Three hollow 3D objects are shown in Figure 2.3. For the open cylinder,  $\beta_0 = 1$ ,  $\beta_1 = 1$ , and  $\beta_2 = 0$ , while the case of the hollow sphere corresponds to  $\beta_0 = 1$ ,  $\beta_1 = 0$ , and  $\beta_2 = 1$ ; the hollow torus has Betti numbers  $\beta_0 = 1$ ,  $\beta_1 = 2$ , and  $\beta_2 = 1$ . Note that the two holes/loops arise from the separate enclosures along the toroidal and poloidal directions.

As demonstrated, homology characterizes the connectivity of  $N$ -dimensional patterns. Several numerical packages, such as CHomP [83], are freely available and have been developed for performing *computational homology*. Inherently, this analysis technique quantifies connectivity in *binary* discretized patterns, such as those shown in Figures 2.2 and 2.3. However, quantities that are measured or simulated in many systems are continuous functions (e.g., velocity or temperature fields), and hence thresholding is required to generate such binary patterns. The concept of computational homology can be extended to utilize the topological information contained in the functional dependence of such quantities—one such formalism is that of persistent homology.

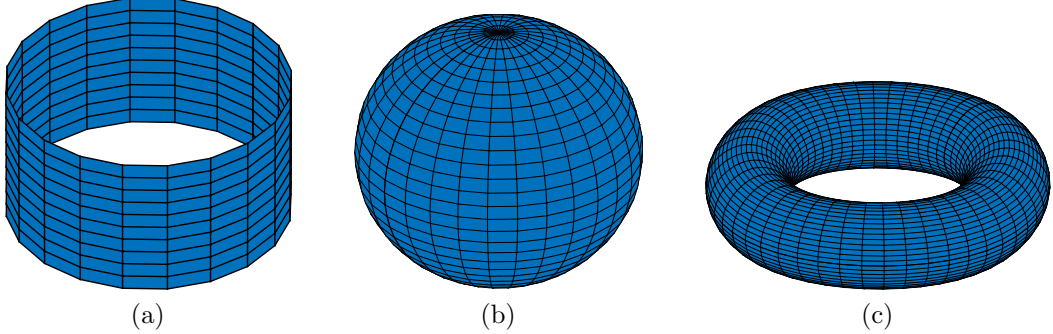


Figure 2.3: Example 3D shapes that when analyzed using homology yield the following Betti numbers: (a)  $\beta_0 = 1$ ,  $\beta_1 = 1$ , and  $\beta_2 = 0$  for an open ended cylinder, (b)  $\beta_0 = 1$ ,  $\beta_1 = 0$ ,  $\beta_2 = 1$  for a hollow sphere, and (c)  $\beta_0 = 1$ ,  $\beta_1 = 2$ ,  $\beta_2 = 1$  for a hollow torus.

### 2.2.2 Overview of Persistent Homology

The principal aspect of the persistent homology analysis is the construction of persistence diagrams (PDs), which each contain a set of points  $p$  corresponding to well-defined topological features of the pattern being analyzed. For an  $N$ -dimensional pattern,  $N$  PDs are generated, each associated with the aforementioned forms of connectivity (components, holes, etc.). In this brief overview, persistent homology is explained for the 1D case using a continuous, real function  $f: \mathbb{R} \rightarrow \mathbb{R}$ . Recall that a smooth real function  $f(x)$  is said to have a *critical point* at  $x$  if  $f'(x) = 0$ . Each (non-degenerate) critical point corresponds to either a local minimum or a local maximum of  $f(x)$ . To construct a PD, a threshold  $\theta \in \mathbb{R}$  is varied from  $-\infty$  to  $\infty$  and the connectivity of the *sublevel set*:

$$C(f, \theta) = \{x \in \mathbb{R} \mid f(x) \leq \theta\} \quad (2.1)$$

is considered. This connectivity only changes when a local minimum (at critical point  $x_{min}$ ) or local maximum (at critical point  $x_{max}$ ) is encountered. At a local minimum, a new component appears, which is called a *birth*; at a local maximum, two components merge to form just one, which is called a *death*. When a death is encountered, it is paired with the highest, adjacent birth and a point  $(f(x_{min}), f(x_{max}))$  is plotted in

the persistence diagram.

To illustrate this methodology, consider the 1D pattern shown in Figure 2.4 to the left. The critical points have been labeled  $x_i$  for  $i = 1, \dots, 6$ , where  $\{x_2, x_4, x_6\}$  correspond to local minima and  $\{x_1, x_3, x_5\}$  correspond to local maxima. As a threshold  $\theta$  is swept along the vertical axis from  $-\infty$  to  $\infty$ , the first local minimum or “birth” is encountered at  $(x_4, f(x_4))$ . Continuing, another birth is encountered at  $(x_2, f(x_2))$ . Next, a local maximum or “death” is encountered at  $(x_3, f(x_3))$ ; this death is then paired with the point  $(x_2, f(x_2))$  because it is the *highest*, adjacent birth, and a point  $(f(x_2), f(x_3))$  is plotted in the PD to the right. As  $\theta$  is increased further, another birth is encountered at  $(x_6, f(x_6))$ , then a death at  $(x_1, f(x_1))$ . This death cannot be paired with  $(x_6, f(x_6))$  because it is not *adjacent*, nor can it be paired with  $(x_2, f(x_2))$  because that point has already been paired. Hence, the death at  $(x_1, f(x_1))$  is paired with  $(x_4, f(x_4))$ , and a point is plotted in the PD at  $(f(x_4), f(x_1))$ . Finally, a death is encountered at  $(x_5, f(x_5))$  which is paired with  $(x_6, f(x_6))$  and a point is plotted in the PD at  $(f(x_6), f(x_5))$ . This 1D example illustrates the general methodology for generating a PD. For the case of the 2D patterns analyzed in Chapter 6, a 2D example is provided.

There are a few important properties of PDs that should be noted. Firstly, as a consequence of considering the sublevel sets (i.e., sweeping the threshold up), all points in a PD will be above the diagonal. Secondly, the vertical distance between the diagonal and any given point in the PD is called the *life span*. Points far from the diagonal correspond to features in the pattern which persist the longest, and hence are considered the most dominant features. Points close to the diagonal are viewed as small scale features or “noise,” which one may choose to ignore. Figure 2.5 illustrates this concept. In (a), a smooth function is shown in black, while a similar but noisy function is shown in red. The points in each corresponding PD, shown in (b), are very similar with the exception that the red function has several more (potentially

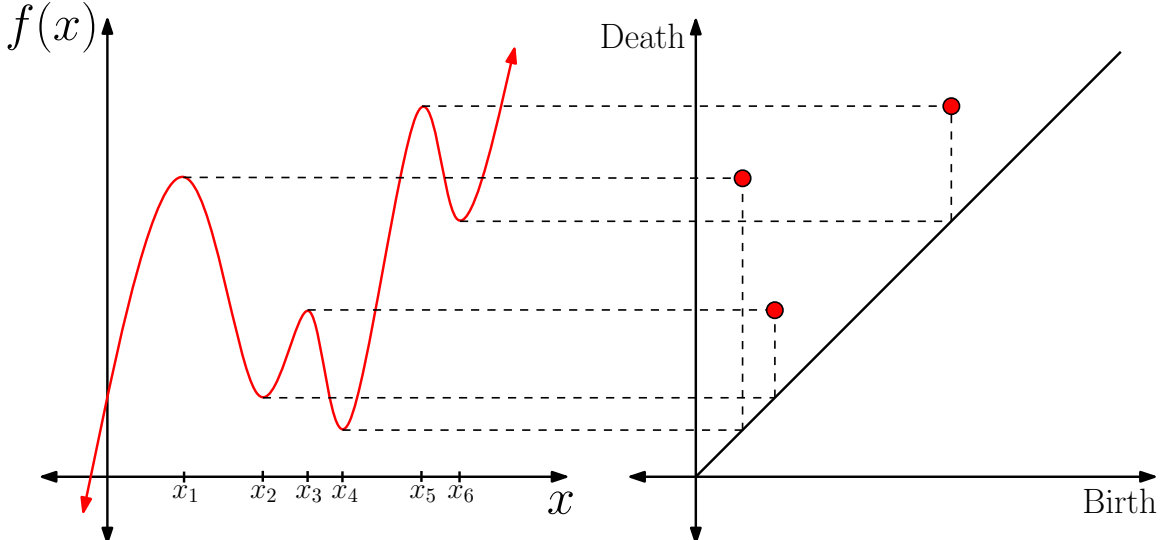


Figure 2.4: A 1D function (left) with three local minima and three local maxima. The critical points are paired as indicated to form three points in the persistence diagram (right). This figure is adapted from reference [1].

negligible) points near the diagonal which are generated by the noisy features. This treatment of noise is an appealing feature in the context of analyzing experimental data, which is often noisy. By constructing a PD, a substantial dimensionality reduction has been performed. For the example shown in Figure 2.5, a function which has continuous spatial dependence undergoes a substantial reduction to 3 dominant points in the PD. Finally, it is emphasized that persistent homology is *symmetry-independent*. For example, observe that if the black function in Figure 2.5 (a) were reflected or translated along the  $x$ -axis, the resulting PD would remain unchanged. Now since in certain cases symmetries of a system allow for such transformations, it is clear that persistent homology automatically removes the redundancies which may arise due to symmetry operations.

An important feature of persistent homology is that it also provides a framework for making *quantitative* comparisons between patterns. This is done by applying a metric to measure the distance between two PDs denoted  $\text{PD}$  and  $\text{PD}'$ . There are a variety of metrics that can be imposed on persistence diagrams [84–87]. One commonly used metric is the *bottleneck distance*, which is defined between  $\text{PD}$  and

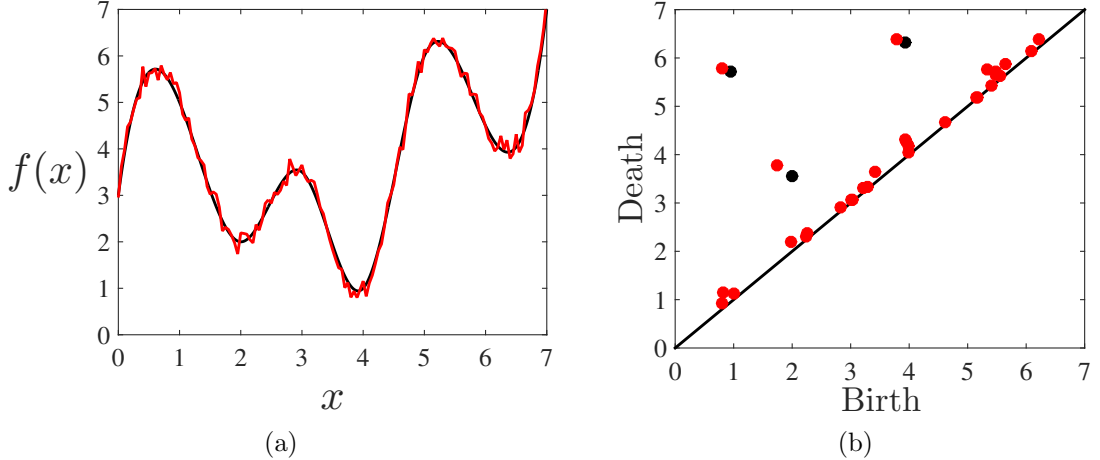


Figure 2.5: An example illustrating how persistent homology handles noisy data. (a) Smooth and noisy 1D functions shown in black and red, respectively. (b) The PDs superimposed on top of each other with the same color convention as the functions. Notice that the dominant far-from-diagonal points do not change much, but the red function generates several additional points near the diagonal which correspond to the noisy features.

$\text{PD}'$  as:

$$d_B(\text{PD}, \text{PD}') = \inf_{\gamma: \text{PD} \rightarrow \text{PD}'} \sup_{p \in \text{PD}} \|p - \gamma(p)\|_\infty, \quad (2.2)$$

where  $\|(a_0, b_0) - (a_1, b_1)\|_\infty := \max \{|a_0 - a_1|, |b_0 - b_1|\}$  and  $\gamma$  ranges over all bijections between persistence points. Similarly, the *degree- $q$  Wasserstein distance* is defined as:

$$d_{W^q}(\text{PD}, \text{PD}') = \left[ \inf_{\gamma: \text{PD} \rightarrow \text{PD}'} \sum_{p \in \text{PD}} \|p - \gamma(p)\|_\infty^q \right]^{1/q}. \quad (2.3)$$

Each calculation involves matching the points  $p \in \text{PD}$  in a one-to-one correspondence (bijection) with the points in  $\text{PD}'$ . According to the definition, every persistence diagram contains an infinite number of points along the diagonal. Hence, there are many different bijections  $\gamma$  between  $\text{PD}$  and  $\text{PD}'$ . Roughly speaking, the distance between  $\text{PD}$  and  $\text{PD}'$  is defined using the bijections that “minimize the shift” in the mapping of the points  $p$  from  $\text{PD}$  to  $\gamma(p)$  in  $\text{PD}'$ . This is illustrated in Figure 2.6, where (a) shows two superimposed PDs; the black lines between the points indicate the most efficient way of moving the blue squares to form the configuration of the red circles. In (b), all possible bijections  $\gamma(p)$  are illustrated with gray lines; the black

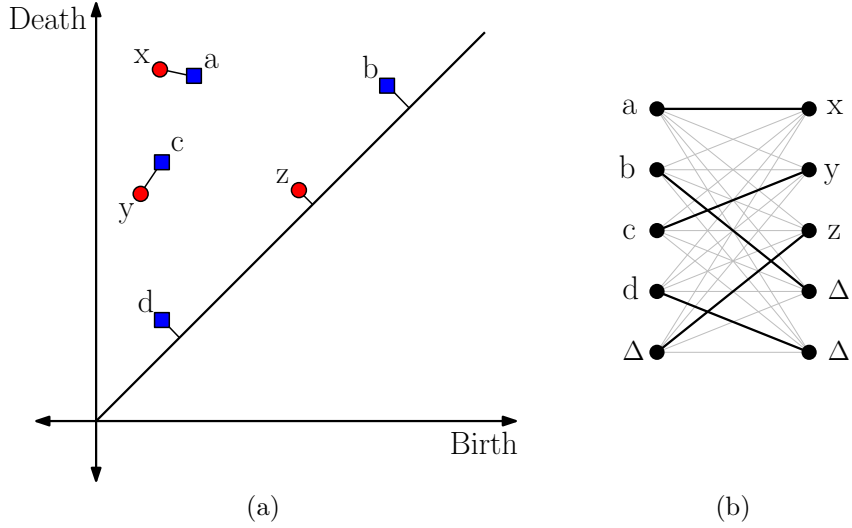


Figure 2.6: An illustration of how distances are computed between PDs. (a) Two PDs represented by red circles and blue squares, with black lines indicating the least cost bijection. (b) A graphical representation of all possible bijections (gray lines) and the most efficient bijections (black lines). Any point on a PD can be matched to the diagonal, denoted  $\Delta$ . This figure is adapted from reference [2].

lines correspond to the bijection with the minimized distance.

It is convenient to imagine the metrics as quantifying distance in a *persistent homology state space*. In this picture, the persistent homology state space can be thought of as the set of all possible PDs, henceforth referred to as  $\text{Per}$ . Then, the PD for a given pattern corresponds to a single point in  $\text{Per}$ . By generating the PDs for several patterns, one then obtains a so-called *point cloud*, which is nothing more than a collection of points in some space (in this case, the space is  $\text{Per}$ ). A point cloud could be generated from many different types of data; for example, the points may correspond to discrete samples from a system evolving in time. By applying persistent homology a *second* time to characterize the connectivity of this point cloud in  $\text{Per}$ , useful information about the dynamics can be obtained; for example, periodicity in a time series could be identified. Persistent homology offers a framework for dimensionality reduction and dynamical insight which is quite different from that of the ECS-based approach.

### 2.2.3 Previous and Present Work

Neither computational nor persistent homology have been used very widely in the fluids community. The limited number of studies which have employed computational homology have used the method for characterizing convection [88–90], bubble swarms [91], and turbulent plasmas [92, 93]. There are even fewer applications of persistent homology, which includes a paper in which Rayleigh-Taylor instabilities are characterized [94], a study of structures in ventricular blood flow [95], and an analysis of Rayleigh-Bénard convection and Kolmogorov flow [96].

A feature of persistent homology which makes it an appealing method for characterizing fluids is its inherent removal of redundancies which may arise due to the symmetries of a system. Such symmetries are a result of coordinate transformations which leave the governing equations of a system equivariant. For fluid flows, symmetries arise in several different geometries and their physical manifestation is usually quite intuitive. For example, pipe flow exhibits a rotational symmetry about the streamwise centerline of the pipe; hence, two flow fields that are identical but rotated relative to each other by an arbitrary angle about this centerline may appear to be different flow fields at first glance, but are in fact dynamically equivalent. Accounting for this redundancy is often referred to as *symmetry reduction* or *quotienting* of symmetries. Procedures have been developed to perform symmetry reduction, such as the “method of slices” [97]. However, the use of a method such as persistent homology automatically quotients any symmetries.

In the analysis presented in Chapter 6, persistent homology is applied to a 2D doubly-periodic simulation of a canonical problem known as Kolmogorov flow (defined in the next section). This system is particularly interesting to study because of the multiple symmetries this system possesses. The lower computational cost of studying a 2D flow field, as opposed to 3D, is again an appealing feature for exploring this new methodology. The simulation which is analyzed using persistent homology is based

on an equation derived from first principles by modeling a Q2D flow in the laboratory. The following section provides an introduction to experiments in Q2D flows.

### 2.3 *Experiments in Quasi-Two-Dimensional Flows*

Flows in 2D have been studied both experimentally and numerically for decades. This is in part because geophysical flows, such as those of the atmosphere and oceans, can be described to a good approximation using 2D models [98]. Additionally, as mentioned above, 2D flows are much more analytically and numerically tractable than their fully 3D counterparts, offering a convenient platform for developing new approaches to understanding turbulence. This was recognized as early as the 1950s, when Andrey Kolmogorov proposed a 2D problem for studying hydrodynamic stability [99]. This canonical fluid flow problem, now known as “Kolmogorov flow,” provides the basis for the analyses performed herein; Kolmogorov flow is detailed in Section 2.3.1 below.

Despite the appealing aspects of studying 2D flows numerically and experimentally, there is the complication that experimental realizations can only achieve *quasi-two-dimensionality*. Real flows are never strictly 2D in the sense that the velocity field describing the flow depends on all three spatial coordinates and has non-zero components along all three spatial directions. As a consequence, much research has been carried out over the last 40 years or so to characterize various Q2D experimental setups and determine how well their dynamics can be captured by a 2D model. In this dissertation, a flow is defined as quasi-two-dimensional if it satisfies the following two conditions: (i) the components of velocity parallel to a plane (horizontal) are much stronger than the component perpendicular to it (vertical) [100] and (ii) the *direction* of the horizontal velocity does not depend on vertical coordinate.

Q2D experiments have been performed in numerous settings, including shallow electrolytic layers [101], superfluid helium [102], liquid metals [103, 104], soap films

[105], and electron plasmas [106]. Electrolyte layers have been chosen for this study because the setup is relatively easy, the materials are not hazardous, and there is an extensive literature characterizing such flows. A discussion of the associated Q2D setup variations is presented in Section 2.3.2, followed by a discussion of the actual two-dimensionality of these setups in Section 2.3.3.

### 2.3.1 Kolmogorov flow

Kolmogorov flow was introduced by Andrey Kolmogorov in 1959 as a mathematical problem for studying the transition to turbulence [99]. In its original formulation, Kolmogorov flow refers to the motion of a viscous fluid in two dimensions (henceforth referred to as  $x$  and  $y$ ) driven by a forcing that points along the  $x$ -direction and varies sinusoidally along the  $y$ -direction. The fluid flow is considered incompressible,  $\nabla \cdot \mathbf{u} = 0$ , and is governed by the 2D Navier-Stokes equation,

$$\partial_t \mathbf{u} + \mathbf{u} \cdot \nabla \mathbf{u} = -\frac{1}{\rho} \nabla p + \nu \nabla^2 \mathbf{u} + \mathbf{f}. \quad (2.4)$$

Here,  $\mathbf{u} = (u_x, u_y)$  is the velocity field,  $p$  is the 2D pressure field, and  $\mathbf{f} = A \sin(\kappa y) \hat{\mathbf{x}}$  represents the driving force per unit mass with amplitude  $A$  and wavenumber  $\kappa$ . The parameters  $\rho$  and  $\nu$  are the density and the kinematic viscosity of the fluid being driven, respectively. Kolmogorov flow has served as a convenient model for understanding a wide variety of hydrodynamic phenomena in 2D, such as fluid instabilities [107–110], 2D turbulence [111], and coherent structures [79, 112, 113], to name a few.

Since flows in the laboratory are never strictly 2D, experimental approximations of Kolmogorov flow have often been carried out in either shallow layers of electrolytes [101] or in soap films [114], wherein geometric confinement suppresses the component of velocity along one of the spatial directions ( $z$ ), making the flow closer to being 2D. The evolution of such Q2D flows has often been described by adding a linear friction term to the 2D Navier-Stokes equation (2.4):

$$\partial_t \mathbf{u} + \mathbf{u} \cdot \nabla \mathbf{u} = -\frac{1}{\rho} \nabla p + \nu \nabla^2 \mathbf{u} - \alpha \mathbf{u} + \mathbf{f}, \quad (2.5)$$

where  $\alpha$  is a constant. The addition of this term was first suggested by Bondarenko *et al.* [101] in the context of a Q2D flow realized in an electromagnetically driven shallow layer of electrolyte. In such a flow, the bottom of the fluid layer is constrained to be at rest because it is in contact with the solid surface of the container holding the fluid. This no-slip constraint at the bottom of the fluid layer causes a gradient in the magnitude of the horizontal velocity  $\mathbf{u}$  along the vertical direction  $z$ . Bondarenko *et al.* [101] rationalized that the dissipation due to this shear, for sufficiently shallow fluid layers, is captured by the linear friction term. In the context of Q2D flows in electrolyte layers, this term has come to be known as “Rayleigh friction.” Experimental realizations of Kolmogorov flow, which are Q2D and use *roughly* sinusoidal driving, as well as 2D models that employ equation (2.5) with a near-sinusoidal forcing profile are now commonly referred to as “Kolmogorov-like flow.”

### 2.3.2 Setup Variations in Thin Electrolyte Layers

When realized in thin electrolyte layers, Kolmogorov-like flow experiments utilize electromagnetic forcing to generate an approximately sinusoidal forcing profile. Specifically, this flow is generated by passing a constant current  $\mathbf{J}$  through a thin electrolyte layer in the presence of a spatially alternating magnetic field  $\mathbf{B}$ ; the resulting Lorentz forces  $\mathbf{F}$  set the fluid in motion (a schematic diagram is provided in Figure 3.1 in the next chapter). Fluid flows in shallow electrolytic layers have been studied extensively beyond the context of Kolmogorov-like flow. Such experiments (with fluid layer thickness usually between 0.2 and 1 cm) have been realized in both homogeneous, single layer setups as well as stratified, two layer setups. The first experimental realization of Kolmogorov-like flow by Bondarenko *et al.* [101] used a homogeneous, single electrolyte layer. Several subsequent studies have also used the single layer setup to investigate variations to the Kolmogorov-like flow geometry [115–120] and the statistics of freely decaying turbulence [121, 122], among several other studies

[123–127]. However, all such flows necessarily exhibit a gradient in the  $z$ -component of vorticity along the vertical direction. This vorticity gradient provides a mechanism for circulation along the  $z$ -direction, which is known as “Ekman pumping” [128, 129]; this effect is detrimental to experiments aiming to generate flows that are as 2D as possible. Consequently, new fluid layer configurations have been introduced which make use of stratification to inhibit this effect.

In the mid 1990s, in the context of characterizing the statistics of decaying turbulent flow, Marteau *et al.* [130] introduced the two-miscible-layer configuration. In this setup, a thin layer of fresh water is suspended above a thin layer of salt water; the relative densities of the salt water and fresh water maintain the configuration. This setup has been used extensively to study mixing phenomena [131–136], as well as to test statistical theories of 2D turbulence, such as the inverse energy cascade [137], Richardson pair dispersion [138], and the direct enstrophy cascade [139]. A decade later, a third configuration (the “two-immiscible-layer configuration”) was introduced by Rivera and Ecke [140], in which an electrolyte is suspended on top of an immiscible, denser dielectric fluid. The dielectric, although not electromagnetically driven, is viscously coupled to the driven top layer, essentially serving as a lubricant between the top layer and the solid surface at the bottom of the container. The two-immiscible-layer setup, having been introduced the most recently of the three setups, has been implemented the least of the three setups, with a single work focused on mixing [141] and a couple statistical studies [142, 143] following Rivera and Ecke’s article which introduced this setup [140].

Each of the three configurations for generating Q2D flows in thin electrolyte layers has its own advantages and disadvantages. The single layer configuration is, of course, the simplest of the three; however, without any stratification, it is perhaps the most prone to 3D effects. The two-miscible-layer configuration is moderately more challenging to set up. Often, the fresh water is added to the container then the salt water

is gently injected below; this prevents the mixing of the two layers that would occur if both were poured into the container. For visualization, it is also advantageous to seed the interface of the two layers in this setup so that there are no surface tension effects on the seeding particles [129]. A disadvantage of the two-miscible-layer setup, however, is that it may only be run for a limited amount of time before diffusion homogenizes the fluid layers. Of the three setups, the two-immiscible-layer configuration likely offers the best two-dimensionality, as it is the most strongly stratified, but it also requires the most effort to set up. Since the two layers are immiscible, diffusion is not an issue and hence experiments using this configuration may be run arbitrarily long. One potential drawback, however, is that the electromagnetic forcing in this configuration is somewhat less efficient in the sense that the driven electrolyte layer is now further away from the permanent magnets located below both fluid layers; this decrease in the magnetic field essentially requires larger driving currents to achieve the same Reynolds numbers, which gives rise to more Joule heating, which in turn may affect the fluid's viscosity. The question remains, however, to what degree each of these fluid configurations can closely approximate a 2D flow; this is discussed in the following section.

### 2.3.3 How Two-Dimensional Are Flows in Thin Electrolyte Layers?

Efforts to characterize the degree of two-dimensionality of flows in electromagnetically driven thin fluid layers have largely focused on the two-miscible-layer configuration. This is likely because it is generally accepted that stratification enhances two-dimensionality, making this setup more favorable than the single, homogeneous layer setup. The fact that the two-immiscible-layer configuration is a decade newer than the two-miscible-layer configuration may explain why far fewer studies have directly characterized its two-dimensionality. Historically, there has been some controversy as to whether the the two-miscible-layer configuration can be considered Q2D. The

works of Jüttner *et al.* [144] and Satijn *et al.* [145] generally supported the notion that such flows could be considered Q2D. However, the work of Akkermans *et al.* [124, 146, 147] indicated that, at high Reynolds numbers ( $Re \approx 2000$ ), the vertical velocity component was comparable to the horizontal components and hence the flow could no longer be considered Q2D. To explain this discrepancy, Kelley and Ouellette [129] performed experiments over a wide range of Reynolds numbers ( $30 < Re < 250$ ) and showed that there is a critical Reynolds number ( $Re_c \approx 200$ ) below which the flow can be considered Q2D.

These studies, aimed at understanding the three-dimensionality of flows in shallow electrolytic layers, suggest that there are three mechanisms that lead to three-dimensionality in thin electrolyte layer flows. Ekman pumping [124, 128, 129], which results from the variation of vorticity with depth, and interfacial deformations, which drive gravity waves [147], are small effects that are in play at all Reynolds numbers. A shear instability, on the other hand, is a large effect which sets in above a critical Reynolds number [129]. This instability was observed at  $Re \approx 200$  for the two-miscible-layer configuration, so it is reasonable to expect that the two-immiscible-layer configuration, which is used in the experiments discussed in this dissertation, may be considered Q2D even beyond  $Re = 200$ . Experimental measurements, which are briefly discussed in Section 3.1.5, verify that the setup employed here is indeed Q2D for the range of  $Re$  considered.

## CHAPTER III

# EXPERIMENTAL REALIZATION AND MODELING OF KOLMOGOROV-LIKE FLOW

In this chapter, Kolmogorov-like flow is discussed from the perspectives of experimental realization, theoretical modeling, and numerical simulation. The goal of this chapter is to provide a detailed description of the experimental setup and a discussion of the derivation of a model which allows for quantitative agreement between experiment and simulation. In Section 3.1, all aspects of the experimental realization are discussed. Section 3.2 presents a discussion of how the experimental flow is modeled. Finally, Section 3.3 provides details of the numerical modeling employed in this dissertation.

### ***3.1 Experimental Realization***

In this section, a thorough discussion of the experimental setup is presented, including construction of the experimental apparatus, the setup procedure, details of the control circuit, information concerning data acquisition and processing, and a brief discussion of the verification of quasi-two-dimensionality which has been obtained.

#### **3.1.1 Constructing the Experimental Apparatus**

As discussed in the previous section, the Q2D Kolmogorov-like flow is generated by passing a direct current density  $\mathbf{J}$  through a thin layer of electrolyte in the presence of a spatially alternating magnetic field  $\mathbf{B}$ , resulting in spatially varying Lorentz forces  $\mathbf{J} \times \mathbf{B}$ . This magnetic field is generated by a permanent magnet array which is immediately below the container which holds the fluids. In this section, the construction of this apparatus is described in detail.

The magnet array consists of 14 Nd<sub>2</sub>Fe<sub>14</sub>B magnets of grade N42, manufactured by K&J Magnetics, Inc. Each magnet is 15.24 cm long and 1.27 cm wide, with a thickness of  $0.32 \pm 0.01$  cm. The magnetization is through the thickness, with a surface field strength of about 0.2 T. The magnets are positioned side-by-side along their width to form a  $15.24\text{ cm} \times (14 \times 1.27\text{ cm}) \times 0.32\text{ cm}$  array such that the adjacent magnets have fields pointing in opposite directions (along  $\pm\hat{\mathbf{z}}$ ), normal to the plane of the array. The magnets are stable in this configuration, with each individual magnet attracting its immediate neighbors. However, care should be exercised when constructing the array, as the magnets are brittle and their attracting forces can cause them to break upon initial contact.

This magnet array is placed on the surface of a flat aluminum plate of dimensions  $30.5\text{ cm} \times 30.5\text{ cm} \times 1.0\text{ cm}$  and laterally centered. Four thin, rectangular pieces of aluminum with the same thickness as the magnets ( $0.32 \pm 0.02$  cm) are placed beside the magnet array to create a level surface. These aluminum pieces are machined such that when placed beside the magnet array, the magnets and aluminum pieces form a larger, laterally centered, level array of dimensions  $25.4\text{ cm} \times 25.4\text{ cm} \times 0.32 \pm 0.02$  cm. Manufacturing imperfections in the individual magnets and the aluminum pieces result in a surface which is not absolutely smooth. Hence, a thin glass plate measuring  $25.4\text{ cm} \times 25.4\text{ cm}$  in area with a thickness of  $0.079 \pm 0.005$  cm is placed atop the magnet and aluminum array to provide a uniform bottom surface for the fluid container<sup>1</sup>. Since the electromagnetic forcing is proportional to the strength of the magnetic field, and the magnetic field drops off approximately exponentially with  $z$ , it is most efficient to use a thin glass plate. The material used here is “Gorilla Glass” brand, manufactured by Corning; this material is very thin while also maintaining the strength, durability, and rigidity necessary for precise dimensions and prevention

---

<sup>1</sup>It is noted that the results of Chapter 5 correspond to an older version of the apparatus which does not have the glass plate in place. Results from Chapter 4, however, correspond to the apparatus described here.

of breaking. A layer of silicone adhesive is then applied along the lateral boundaries of the glass plate and the magnet and aluminum array, such that both are secured to the aluminum plate.

A thin layer of black, adhesive contact paper (with approximate thickness 0.005 cm) is placed on top of the glass plate to serve as a dark background for imaging. The surface of the contact paper serves as the bottom boundary for the fluids. The origin of the coordinate system used throughout this dissertation is placed at this height and the lateral center of the magnet array, oriented with the  $x$ -coordinate aligned with the magnet length, the  $y$ -coordinate pointing in the direction of the magnet periodicity, and the  $z$ -coordinate pointing opposite gravitational acceleration. See Figure 3.1 for a schematic diagram.

A calibration target of dimensions 17.7 cm  $\times$  22.8 cm  $\times$  0.6 cm, discussed in more detail below, is fabricated from acrylic using a laser cutter. This calibration target is placed atop the contact paper, at the lateral center. Rectangular bars of clear acrylic are placed adjacent to the calibration target, to create the lateral boundaries of the fluid container that run parallel to the  $y$ -direction. These solid boundaries for the fluid are hence positioned at a distance of 17.8 cm apart, centered about the origin, and will henceforth be referred to as the “end walls.” Similarly, running parallel to the  $x$ -direction, two electrodes are mounted on rectangular bars of acrylic which are placed adjacent to the calibration target. These fluid boundaries are then positioned at a distance of 22.9 cm, centered about the origin, and will henceforth referred to as the “side walls.” The electrodes forming the side walls are used to drive a uniform current density through the electrolyte, and hence they extend slightly beyond the length of the acrylic bars such that they may be easily connected to a constant current circuit (described below) using alligator clips. The end walls and side walls are affixed directly onto the contact paper using a clear silicone adhesive (Dap “All-Purpose Adhesive Sealant”). A small but adequate amount of silicone is

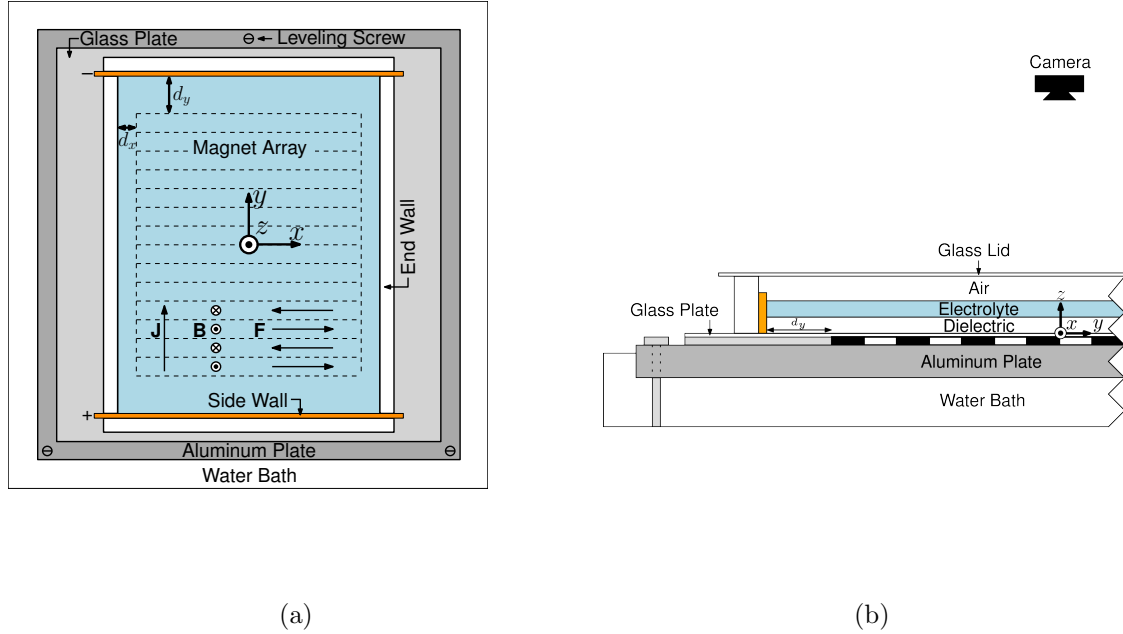


Figure 3.1: A schematic diagram of the two-immiscible-layer Kolmogorov-like flow experimental setup viewed (a) from above and (b) from the transverse cross section. The fluid flow is driven by Lorentz forces arising from the interaction of a direct current density  $\mathbf{J}$ , which is passed through the electrolyte in the  $y$ -direction, with a spatially varying magnetic field  $\mathbf{B}$  pointed in the  $\pm z$ -direction, generated by an array of permanent magnets located below the fluid layers (dashed lines in (a); black and white rectangles in (b)). The resulting forcing  $\mathbf{F}$  is in the  $\pm x$ -direction. The flow is bounded by two end walls, two side walls (electrodes), and a solid, bottom surface, while the top surface of the fluid is a free electrolyte-air interface. This container is mounted on an aluminum plate which is leveled and submerged in a water bath that is regulated such that the electrolyte is maintained at  $23^\circ\text{C} \pm 0.2^\circ\text{C}$ .

used such that the walls are securely fastened but excess silicone does not adhere the calibration target. Applying a thin layer of tape to the perimeter of the calibration target can help ensure it does not end up glued down. After the silicone has dried, the calibration target is removed. The placement of the end walls and side walls then form a  $17.8 \pm 0.1$  cm  $\times$   $22.9 \pm 0.1$  cm container which will hold the two immiscible fluid layers. Note that the location of the end walls and side walls leaves a buffer region of  $d_x = 1.3$  cm and  $d_y = 2.5$  cm, respectively, between the edge of the magnet array and these solid boundaries. See Figure 3.1 (a) for a schematic diagram depicting the locations of the walls. The aluminum plate upon which the magnets are mounted then has three holes drilled and tapped so that the entire apparatus is supported by three screws, which can be adjusted to level the system. As a final step, a thin layer of clear flowable silicone (Dow Corning “734 Flowable Sealant”) is applied to the exterior of each lateral boundary to ensure that the container is completely sealed.

### 3.1.2 Setting Up the Experiment

To ensure that the viscosity remains constant throughout the duration of experiments, it is necessary to temperature-regulate the apparatus. This is necessary because the viscosity of the electrolyte changes by about  $3.5\%/\text{ }^\circ\text{C}$  and the temperature of the room in which experiments are performed fluctuates by about  $2\text{ }^\circ\text{C}$  on a daily basis. Furthermore, passing a current through a resistive conductor (the electrolyte) results in Joule heating, which can raise the temperature at least another  $1\text{ }^\circ\text{C}$ . Hence, when setting up the experiment, it is placed in a temperature-controlled water bath. The water level is carefully maintained such that the aluminum plate is wetted, but the water does not rise above the top surface and short the electrodes. A small aquarium pump is used to circulate the water in the bath to improve the temperature regulation.

Every time the experiment is set up, it is carefully leveled and optically aligned. In order to avoid disrupting the leveling and alignment of the apparatus later, one

should first secure the electrical connections to the electrodes and also position the arrays of light emitting diodes (discussed below) which illuminate the seeding particles in the fluids. For leveling, a precision bubble level with a sensitivity of 1 minute / division is placed atop the bottom surface which holds the fluids and is leveled to within  $0.03^\circ$ . A camera (discussed in section 3.1.4) is permanently mounted directly above the experimental apparatus using a rigid four-leg frame constructed from 80/20. This camera is connected via USB to a Windows computer, and MATLAB is used for image acquisition. The calibration grid is carefully placed inside the flow domain (the fluids have not been added yet) and the water tub containing the apparatus is slightly nudged until the grid is properly positioned. The lateral positioning should be such that the entire flow domain is visible, but it need not be precisely centered, as the calibration grid will be used to perform a coordinate transformation from pixels to cm and to place the origin at the lateral center of the flow domain. The rotational alignment, however, must be precise. This can be checked and adjusted in real time by streaming live video from the camera to the computer. The leveling and optical alignment can be adjusted iteratively until the apparatus positioning is adequate. Once the alignment is finalized, an image of the calibration grid is recorded for use later; an example image of the carefully aligned calibration grid is shown in Figure 3.2. At this point, the calibration grid should be removed very carefully to minimize any shift to the apparatus's position.

The interior of the container can now be filled with the two immiscible fluids. The desired final volumes are 122 mL of each of the electrolyte and dielectric, such that each fluid layer is 0.30 cm thick. However, in practice, pouring the electrolyte onto the dielectric when the layers are so thin always results in the electrolyte passing through the dielectric and wetting the bottom surface. To ensure that the fluid layers are uniformly stratified in their final configuration, an excess of each fluid is initially added to the container and then removed using a syringe. To begin, approximately

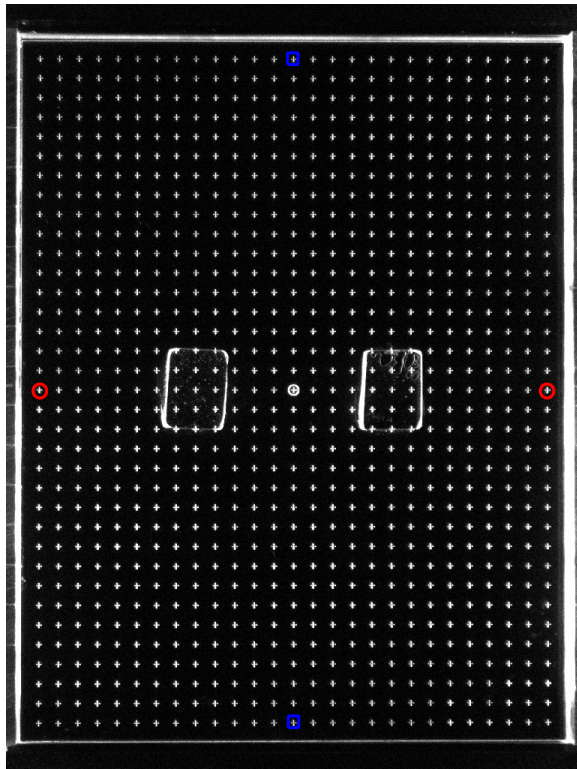


Figure 3.2: An image of the calibration grid placed inside the flow domain allows for careful optical alignment and a coordinate transformation from pixels to cm. The red circles and blue squares indicate the pairs of cross hairs which are used for determining the pixel-to-cm scaling constant.

220 mL of the dielectric fluid is added to the container. Then, approximately 160 mL of electrolyte is carefully added above the dielectric, and two drops of viscosity-matched surfactant (a solution of dish soap, water, and glycerol) is added to lower the surface tension. At this point, each fluid layer should be of uniform thickness and in contact with the entirety of the lateral boundaries, with the possible exception of a few drops of electrolyte wetting the bottom surface. The excess of the two fluids as well as the small amount of electrolyte wetting the bottom surface can then be removed using a syringe. When removing the excess fluids, it is important to be wary that as the electrolyte becomes thinner, it also becomes less stable in its uniform, planar configuration. Spilling just a few drops of the dielectric onto the electrolyte free surface can “break open” the electrolyte layer, exposing the dielectric layer below. More fluids would then have to be added to and removed from the container to obtain the uniform stratification again.

The volumes added to the container and then removed from the container are carefully measured such that the final volumes are  $122 \pm 4$  mL of dielectric and  $122 \pm 2$  mL of electrolyte. The two immiscible layers are then  $h_d = 0.30 \pm 0.01$  cm and  $h_e = 0.30 \pm 0.005$  cm thick, respectively. The dielectric fluid used is perfluorooctane, which has a viscosity of  $\mu_d = 1.30$  mPa·s and a density of  $\rho_d = 1769$  kg/m<sup>3</sup> at 23.0°C. The electrolyte fluid is a solution consisting of 60% 1 M copper sulfate solution and 40% glycerol by weight. The electrolyte’s viscosity is  $\mu_e = 5.85$  mPa·s and the density is  $\rho_e = 1192$  kg/m<sup>3</sup> at 23.0°C. Note that the viscosity ratio  $\mu_e/\mu_d = 4.5$  has been increased to enhance the two-dimensionality of the electrolyte, which is explained below in section 3.2.3. The larger uncertainty in the volume of the dielectric is a result of how quickly perfluorooctane evaporates when exposed to open air. Because of this evaporation, the dielectric should be promptly covered by the electrolyte during the setup process. A calibrated thermistor is placed in the corner of the flow domain so that temperature measurements can be taken while minimally

disrupting the flow. Finally, a glass lid is placed on top of the container to limit evaporation. While the experiment is running, temperature measurements are taken inside the flow domain via the calibrated thermistor. The water bath surrounding the apparatus is then iteratively adjusted such that the electrolyte and dielectric are maintained to  $23.0 \pm 0.2^\circ\text{C}$ . By maintaining the temperature of the fluids, their associated change in viscosity is kept to a minimum.

### 3.1.3 Constant Current Control Circuit

The direct current which is passed through the electrolyte serves as the control parameter. By slowly sweeping the current from about 5 to 25 mA (which corresponds to a current density of about 10 to 50 A/m<sup>2</sup>), the flow exhibits a series of bifurcations, transitioning through at least three stable states before becoming weakly turbulent at higher values. In order to study this sequence of bifurcations, it is convenient to construct a constant current control circuit which can be programmed using MATLAB. This circuit is discussed in this subsection.

A schematic diagram for the constant current control circuit is shown in Figure 3.3 (a). There are two core components to this circuit: the LM317 3-terminal adjustable voltage regulator and the AD8400 digital potentiometer (“digipot”). The LM317 device operates in such a way that the OUT terminal will provide the current source necessary such that the OUT terminal is  $V_{ref} = 1.25$  V greater than the ADJ terminal. Since  $V_{ref}$  is constant, the resistance value of the digipot determines the amount of current that flows through the digipot and the experimental apparatus to ground. This constant current  $\mathcal{I}$  is then given by:

$$\mathcal{I} = V_{ref}/R, \quad (3.1)$$

where  $R$  is the resistance of the 1 kΩ digipot. Note that the constant current value is independent of the load, meaning the conductivity of the electrolyte does not play a role in determining  $\mathcal{I}$ . By adjusting  $R$ , the constant current source can be varied.

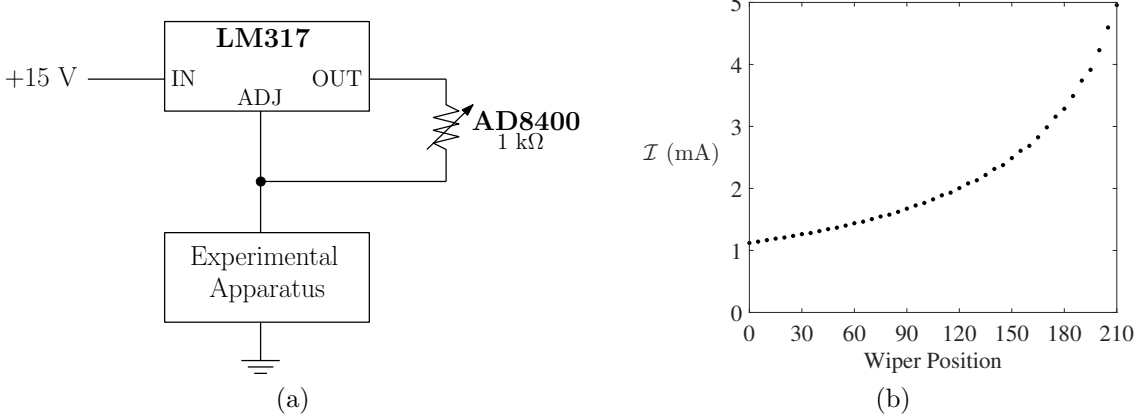


Figure 3.3: (a) A schematic diagram of the elementary component of the constant current control circuit. By adjusting the resistance  $R$  of the  $1\text{ k}\Omega$  digipot (AD8400) using MATLAB, the voltage regulator (LM317) produces a constant output current of  $\mathcal{I} = 1.25\text{ V}/R$ . (b) A plot showing the current through the experimental apparatus as a function of the wiper position for an elementary component of the circuit.

The AD8400 digipot has 256 wiper positions, which allows the resistance to be varied in steps of  $\Delta R \approx 4\text{ }\Omega$ . However, this device is only rated for a continuous current of up to 5 mA. Hence, to attain a higher range of current, 5 identical circuits are constructed and connected to the experimental apparatus in parallel. The wiper positions of the digipots are adjusted by interfacing them with a Measurement Computing USB-1208FS device which is controlled using MATLAB. By varying the wiper positions across all 5 digital potentiometers, the constant current passing through the electrolyte can be increased or decreased throughout the desired range of current values.

In practice, precise control of the current requires a calibration for each individual digipot to determine the precise range of output current as a function of the digipot wiper position. Such a calibration is shown in Figure 3.3 (b) for a single digipot. It is important to set bounds on the allowable wiper positions, as too small of a resistance can result in a current greater than 5 mA which will damage the device. In this case, the maximum allowable wiper position is 210.

Note that the circuit used to drive the light emitting diodes (LEDs) is the same

as that of Figure 3.3 (a), except that a  $200\ \Omega$  mechanical potentiometer is used in place of the AD8400. If the light brightness needs to be adjusted, the wiper position of the potentiometer is adjusted mechanically using a screwdriver. A constant direct current is necessary for driving the LEDs so that the brightness is uniform across all flow images, which are collected at 15 Hz (at this frame rate, an alternating current power supply would result in “flickering” in the images).

### 3.1.4 Measuring the Experimental Velocity Fields

A technique known as *particle image velocimetry* (PIV) is used for measuring the velocity fields in the experiment. To perform PIV, a fluid flow is seeded with tracer particles for visualization and then rapidly imaged with a camera. By cross-correlating several pairs of images, a time series of spatially-resolved displacement fields can be obtained. The displacement fields (which are in units of pixels) can then be dimensioned by using a calibration grid and the time between the pairs of images. This process is explained in detail below.

To begin, hollow glass microspheres are added to the fluid for visualization and are illuminated with two arrays of white light emitting diodes (LEDs). Each array of LEDs is positioned running along the length of the end walls and points inward towards the flow. Two separate methods are used to seed the flow with particles, either at the free surface of the electrolyte or at the dielectric-electrolyte interface. The simplest is free surface seeding, in which hollow glass microspheres are sprinkled onto the electrolyte; these particles are Glass Bubbles (K15) manufactured by 3M and sieved to obtain particles with mean radius  $24.5 \pm 2\ \mu\text{m}$  and mean density  $150\ \text{kg/m}^3$ . Seeding at the electrolyte-dielectric interface is more challenging, but is particularly useful when the experiment will be running continuously for longer than an hour, as it is observed that particles seeded at the interface remain evenly distributed much longer than those at the free surface (potentially several hours, depending on the flow

regime). For interfacial seeding, hollow glass microspheres coated in titanium oxide (mean radius  $9 \pm 6 \mu\text{m}$  and mean density  $800 \text{ kg/m}^3$ ), are mixed with perfluorooctane then injected into the perfluorooctane layer. Although the titanium oxide coated microspheres are less dense than both fluids, they remain trapped at the dielectric-electrolyte interface due to interfacial tension. This process works best if performed after the full excess volumes of fluids have been added to the container. It is of course important that the volume of perfluorooctane that is used for injecting particles (usually about 10 mL) also be included in the calculation of the final volume left in the container. Furthermore, it is useful when removing the excess perfluorooctane to position the syringe needle over any regions where particles have stuck to the bottom surface. Removing these static particles from the black bottom surface will improve the quality of the PIV measurements.

The seeded flow is imaged using a DMK 31BU03 camera manufactured by The Imaging Source. This camera has a CCD sensor with a resolution of  $1024 \times 768$  pixels, which results in an adequate spatial resolution of about 53 pixels per magnet width. The images are collected in a continuous uncompressed AVI movie recorded at 15 Hz, which are later extracted from the video file. PIV is performed for pairs of images that are  $dt$  seconds apart. Note that a general overview of PIV is available in references [148, 149]. All experimental velocities presented in this dissertation come from PIV measurements made using Prana [150, 151]. Prana interfaces with MATLAB, can be run in parallel, and has many advanced features which allow for high quality velocity measurements. The specific parameters and features of each package are discussed in detail in Appendix A.

The PIV software outputs two coordinate arrays  $X$  and  $Y$  and a time series of displacement fields  $d_x(x, y, t)$  and  $d_y(x, y, t)$ , all of which are in units of pixels. To transform these variables into physically-meaningful units, first the scale factor  $M$  which is the ratio relating pixels to cm is calculated by inspecting the calibration

grid image which was collected when setting up the experiment. This is done by determining the number of pixels between the cross hairs circled in red in Figure 3.2 to the nearest pixel. This number is divided by the 16.49 cm it corresponds to in real space. Then, the number of pixels between the cross hairs indicated by blue squares is determined to the nearest pixel. This number is divided by the 21.54 cm it corresponds to in real space. These two ratios are averaged to obtain  $M$ , which has an uncertainty which is less than 0.3%. Secondly, the pixel coordinates for the center of the domain ( $X_c, Y_c$ ) are determined. Then, the coordinate arrays ( $x, y$ ) in units of cm, with the origin at the center of the flow domain, can be determined from:

$$(x, y) = ((X - X_c)M, (Y - Y_c)M). \quad (3.2)$$

To transform the displacement fields  $d_x(x, y, t)$  and  $d_y(x, y, t)$ , it is necessary to also use the effective frame rate  $1/dt$ . Note that a thorough discussion of how to choose the effective frame rate is provided in Appendix A. The displacement fields are then transformed into units of cm/s using:

$$(u_x, u_y) = (d_x M/dt, d_y M/dt). \quad (3.3)$$

This completes the process for determining the experimental coordinates and velocities which are presented throughout this dissertation.

### 3.1.5 Verification of Quasi-Two-Dimensionality

The quasi-two-dimensionality of the flow has been directly verified by measuring the normalized in-plane divergence of the horizontal velocity field at the electrolyte free surface up to  $Re \approx 50$ . This quantity is defined as:

$$\Lambda = \frac{h_e \iint |\nabla \cdot \mathbf{u}| dx dy}{w \iint |\omega| dx dy}, \quad (3.4)$$

where  $w = 1.27$  cm is the characteristic length scale (magnet width). This quantity is used by Akkermans *et al.* [147] and characterizes the ratio of the horizontal velocity

to the vertical velocity. Measurements obtained show that  $\Lambda$  varies from about 0.01 to 0.02, with no clear systematic trend. Since small errors in PIV can contribute significantly to the value of the divergence computed, it is safe to say that  $\Lambda = 0.02$  provides an upper bound for the relative strength of the vertical flow. This indicates that for the experiment, even in the weakly turbulent regime, the deviation from quasi-two-dimensionality is small.

### **3.2 Theoretical Modeling**

In most previous studies, quantitative comparison between Q2D experiments and theoretical predictions has been hampered by the lack of a reliable and consistent procedure to relate experimental parameters with the coefficients  $\alpha$ ,  $\nu$ , and  $\rho$  in equation (2.5). For instance, bifurcation studies of Q2D Kolmogorov-like flows have often treated  $\alpha$  as a fitting parameter [100, 101] to compare theoretical predictions with experiments, with an *ad hoc* assumption that the viscous term ( $\nu \nabla^2 \mathbf{u}$ ) was negligible. Furthermore, studies employing Q2D experimental flows realized in stratified layers of fluids have not accounted for the variation in the viscosity and density across the fluid layers [144, 152, 153].

To address these deficiencies, the derivation of a new 2D equation [154] is discussed in this section. In particular, this equation is derived from first principles by starting from the full 3D Navier-Stokes equation and depth-averaging along the  $z$ -direction. In addition to the new equation which is discussed, analytical expressions for the coefficients in the model ( $\alpha$ ,  $\nu$ , etc.) are also obtained and can be evaluated by directly substituting experimental parameters. This model, which can be applied to homogeneous or stratified fluid configurations, is discussed next.

#### **3.2.1 Discussion of the Model Derivation**

Consider a shallow layer of fluid, with thickness  $h$ , in a laterally extended container with a flat bottom. As introduced earlier, assume that the  $x$ - $y$  plane is parallel to

the bottom of the container and the  $z$ -axis is in the vertical direction, with  $z = 0$  chosen at the bottom of the fluid layer and  $z = h$  corresponding to the fluid-air interface. The velocity field for such a flow is inherently three-dimensional, in the sense that it generally depends on all three coordinates,  $\mathbf{v} = \mathbf{v}(x, y, z, t)$ . This inherent three-dimensionality is due to the fact that the bottom of the fluid layer ( $z = 0$ ) is constrained to be at rest due to the no-slip boundary condition associated with the solid bottom surface. The velocity field in such a system is governed by the 3D Navier-Stokes equation for an incompressible fluid ( $\nabla \cdot \mathbf{v} = 0$ ) which was given by equation (1.1), and is stated again for convenience:

$$\rho(\partial_t \mathbf{v} + \mathbf{v} \cdot \nabla \mathbf{v}) = -\nabla p + \mu \nabla^2 \mathbf{v} + \mathbf{F} + \rho \mathbf{g}. \quad (3.5)$$

Note that  $\mu = \rho\nu$  is the dynamic viscosity and in the context of the experimental Kolmogorov-like flow,  $\mathbf{F}$  corresponds to the Lorentz force per unit volume which is primarily in the plane of the fluid (the  $x$ - $y$  plane).

Equation (3.5), combined with the incompressibility condition, describes the evolution of the full 3D velocity field. However, for flows in shallow fluid layers, driven by *weak, in-plane* forcing, the vertical velocity component is much smaller compared to the horizontal one [145]. In such flows the characteristic times describing equilibration of momentum in the vertical direction ( $\rho h^2/\mu$ ) are much smaller than those associated with the horizontal directions ( $\rho L^2/\mu$ ). This tends to align an unforced flow at a particular horizontal position ( $x, y$ ) and different  $z$  along the same direction. Furthermore, if the *direction* of the forcing  $\mathbf{F}$  is independent of  $z$ , this forcing will not destroy the alignment and we can assume the *direction* of the velocity to be independent of the height  $z$  allowing the velocity field to be factored as [126, 155]:

$$\mathbf{v}(x, y, z, t) = P(z)\mathbf{u}(x, y, t) \equiv P(z)[u_x(x, y, t)\hat{\mathbf{x}} + u_y(x, y, t)\hat{\mathbf{y}}], \quad (3.6)$$

where  $P(z)$  describes the dependence of the horizontal velocity on  $z$ , and the unit vectors  $\hat{\mathbf{x}}$  and  $\hat{\mathbf{y}}$  lie in the horizontal plane. A thorough discussion on the validity

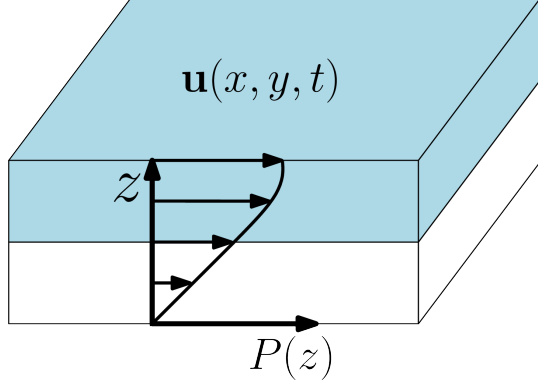


Figure 3.4: An illustration of the velocity profile in the two-immiscible-layer configuration. Under the Q2D approximation, the full 3D velocity  $\mathbf{v}(x, y, z, t)$  can be decomposed as the 2D in-plane velocity at the free surface  $\mathbf{u}(x, y, t)$  times a 1D profile  $P(z)$ .

of this Q2D approximation can be found in [145]. The presence of the solid boundary at the bottom ( $z = 0$ ) and of a free surface at the top ( $z = h$ ) are accounted for by choosing  $P(0) = 0$  and  $P'(h) = 0$ , where  $P' = dP/dz$ . Furthermore, the following normalization condition is imposed:

$$P(h) = 1 \quad (3.7)$$

to make the factorization unique, so  $\mathbf{u}(x, y, t)$  can be interpreted as the in-plane velocity at the free surface ( $z = h$ ). An illustration of  $\mathbf{u}(x, y, t)$  and the profile  $P(z)$  for the two-immiscible-layer configuration is provided in Figure 3.4.

Substitution of (3.6) into (3.5) gives:

$$\begin{aligned} \rho P \partial_t \mathbf{u} + \rho P^2 \mathbf{u} \cdot \nabla_{\parallel} \mathbf{u} &= -\nabla_{\parallel} p + \mu P \nabla_{\parallel}^2 \mathbf{u} + \mu \mathbf{u} \nabla_{\perp}^2 P + \mathbf{F}, \\ \nabla_{\perp} p &= \rho \mathbf{g}, \end{aligned} \quad (3.8)$$

along with  $\nabla_{\parallel} \cdot \mathbf{u} = 0$ , where the subscripts  $\parallel$  and  $\perp$  represent the horizontal and vertical components, respectively. In general, the profile  $P(z)$  depends on the exact form of forcing  $\mathbf{F}$  and the horizontal flow profile  $\mathbf{u}$ . However, it turns out that assuming the profile  $P(z)$  to be independent of  $\mathbf{u}$ , although not intuitive, proves to be valid at moderate  $Re$ . This is demonstrated in Appendix B.

Integrating equation (3.8) over the fluid layer depth along the  $z$ -direction, i.e., from the bottom of the fluid layer ( $z = 0$ ) to the free surface ( $z = h$ ), an equation for the in-plane velocity  $\mathbf{u}$  is obtained:

$$\partial_t \mathbf{u} + \beta \mathbf{u} \cdot \nabla \mathbf{u} = -\frac{1}{\bar{\rho}} \nabla p + \bar{\nu} \nabla^2 \mathbf{u} - \alpha \mathbf{u} + \frac{1}{\bar{\rho}} \mathbf{f}, \quad (3.9)$$

where the subscript  $\parallel$  has been dropped for notational convenience. The parameters  $\beta$ ,  $\bar{\rho}$ ,  $\bar{\nu}$ , and  $\alpha$  are defined as follows:

$$\beta = \frac{\int_0^h \rho P^2 dz}{\int_0^h \rho P dz}, \quad \bar{\rho} = \frac{\int_0^h \rho P dz}{h}, \quad \bar{\nu} = \frac{\int_0^h \mu P dz}{\int_0^h \rho P dz}, \quad \alpha = \frac{(\mu P')_{z=0}}{\int_0^h \rho P dz}, \quad (3.10)$$

The source term  $\mathbf{f}$  on the right-hand side of equation (3.9) corresponds to the depth-averaged force density:

$$\mathbf{f} = \frac{1}{h} \int_0^h \mathbf{F} dz. \quad (3.11)$$

To evaluate this expression,  $\mathbf{F}$  is obtained by modeling the Lorentz forces which drive the electrolyte in the experiment. It is worth noting that in general, the forcing  $\mathbf{F}$  depends on  $z$ , most commonly due to a decay in the magnetic field strength. The 2D source term  $\mathbf{f}$  takes into account the effect of such decay in the 3D forcing profile  $\mathbf{F}$ . The Lorentz force modeling used to obtain  $\mathbf{F}$  is discussed below in Section 3.3.1.

It is emphasized that the parameter  $\beta$  is a prefactor to the advection term which has been unaccounted for (i.e., assumed to be unity) in all previous studies. This new prefactor  $\beta < 1$  accounts for the decrease of the mean inertia of the fluid layer resulting from the velocity gradient along the layer thickness. It can be easily seen that equations (2.4) and (2.5) can be treated as special cases of equation (3.9) by suitable choices of the parameters  $\alpha$  and  $\beta$ . The parameters  $\bar{\nu}$  and  $\bar{\rho}$  are the depth-averaged kinematic viscosity and the depth-averaged density, respectively. For a single homogeneous layer of fluid, the depth-averaged kinematic viscosity is simply equal to the kinematic viscosity of the fluid. However, for stratified layers, the fluid properties  $\mu$  and  $\rho$  depend on  $z$ . In such a case, the integrals in equations (3.10) are computed

taking into account the variation in  $\mu$  and  $\rho$ . The linear friction term  $-\alpha\mathbf{u}$ , which accounts for the presence of the solid boundary at the bottom of the fluid layer, is a direct consequence of *ansatz* (3.6) and depth-averaging. This is distinctly different from how previous studies have included this term in equation (2.5) [100, 101]. It is important to point out that equation (3.9) is a 2D equation that *quantitatively* describes 3D flows in regimes where *ansatz* (3.6) is valid. In particular,  $\mathbf{u}$  describes the velocity at the top, free surface of the electrolyte, facilitating direct comparisons between experimental PIV measurements and numerical simulations.

### 3.2.2 Nondimensionalization

Before proceeding to a discussion of the calculation of  $P(z)$ , a nondimensional form of equation (3.9) is briefly introduced in this section. It is noted that the governing equation (3.9) introduced in the previous section was presented in dimensional form to highlight that parameters  $\beta$ ,  $\bar{\rho}$ ,  $\bar{\nu}$ , and  $\alpha$  can be computed directly from fluid layer properties. However, in the study of differential equations, nondimensionalization is usually preferable, as it often simplifies the problem at hand, may provide physical insight, and is a common convention.

To begin, a characteristic length scale and a characteristic velocity scale are chosen. A natural choice for the length scale is the width of a magnet,  $w = 1.27$  cm. For the velocity scale  $U$ , the spatial root-mean-square (rms) velocity computed over the region  $(|x|, |y|) \leq (4w, 4w)$  (cf. Section 3.1.1) is used; this choice is to facilitate a direct comparison between the experiment and a doubly-periodic simulation with a smaller domain size, as will be discussed in Section 3.3.2. These two quantities can be combined to form a characteristic time scale  $T = w/U$ .

The nondimensional form of equation (3.9) can then be written as:

$$\frac{\partial \mathbf{u}}{\partial t} + \beta \mathbf{u} \cdot \nabla \mathbf{u} = -\nabla p + \frac{1}{Re} (\nabla^2 \mathbf{u} - \gamma \mathbf{u}) + \mathbf{f}_0, \quad (3.12)$$

where the Reynolds number  $Re = Uw/\bar{\nu}$  defines the complexity of the flow, and

$\gamma = \alpha w^2 / \bar{\nu}$  captures the relative strength of the Rayleigh friction and viscous terms in equation (3.9). Lastly,  $\mathbf{f}_0 = wf/U^2$  in the above equation represents the nondimensional rescaled forcing profile. Note that from this point on, the characteristic length scale  $w$ , velocity scale  $U$ , and time scale  $w/U$  will be used for nondimensionalization in this dissertation.

### 3.2.3 Velocity Profile in Two Immiscible Layers

In this section, a derivation for the vertical profile  $P(z)$  of the horizontal velocity (cf. equation (3.6)) is briefly discussed for the case of Kolmogorov-like flow. To begin, it is necessary to assume that the magnet array has an infinite extent and that the magnetic field is perfectly sinusoidal. Magnetic field measurements taken above the center of the magnet array, at a height corresponding to the center of the electrolyte layer are provided in Figure 3.5 and show that the magnetic field is indeed close to sinusoidal. It is also necessary to assume that the magnetic field drops off with some functional dependence. It is found that across the depth of the electrolyte layer, a linear decay of the form  $B_z = B_1 z + B_0$  fits well, where  $B_1 = -0.389 \pm 0.006$  T and  $B_0 = 0.276 \pm 0.01$  T. This approximation allows the 3D Lorentz force  $\mathbf{F}$  to be written analytically.

The form of the horizontal velocity at the free surface  $\mathbf{u}(x, y, t)$ , for low values of driving, is then also sinusoidal, i.e.,  $\mathbf{u}(x, y, t) = u_0 \sin(\kappa y) \hat{\mathbf{x}}$ . Substituting this form of the velocity into equations (3.8) yields a hydrostatic pressure distribution and a boundary value problem for the vertical profile  $P(z)$ . By applying the appropriate boundary conditions, along with a normalization condition  $P(h_e + h_d) = 1$ , a system of five equations with five unknowns is then solved to obtain  $P(z)$ . These lengthy expressions are not provided here for the sake of brevity.

Based on this analysis, a new measure that characterizes the inherent deviation

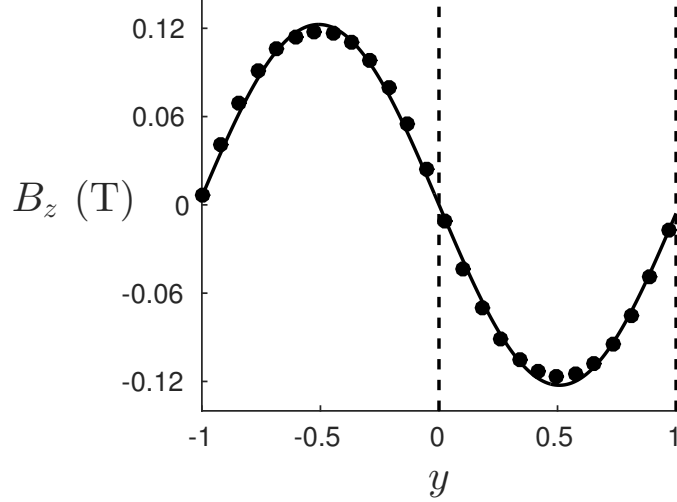


Figure 3.5: Magnetic field measurements (black circles) taken above the center of the magnet array at height  $z = 0.394$ , which corresponds to roughly the middle of the electrolyte layer. A sinusoidal fit to the data, shown by the black curve, suggests that the magnetic field is indeed close to sinusoidal here. Uncertainties are the size of the symbols or smaller.

from two-dimensionality is introduced for the two-immiscible-layer configuration:

$$S = \frac{P(h_d + h_e)}{P(h_d)}. \quad (3.13)$$

The motivation behind using the two-immiscible-layer configuration is that the top layer is lubricated by the dielectric layer below it, which is subject to the no-slip boundary condition at the solid bottom surface. For a perfectly two-dimensional flow, one would expect the velocity field in the top layer to be independent of the  $z$ -coordinate. Hence, for a monotonically varying profile, the value of  $S$  describes how strongly the magnitude of the horizontal velocity field varies with  $z$  in the electrolyte, with  $S = 1$  corresponding to a  $z$ -independent velocity profile.

From this analysis, it should be possible to determine what experimental parameters can be varied to enhance the two-dimensionality of flow, as characterized by equation (3.13). Unfortunately, the functional form of expression (3.13) is quite complicated and does not allow one to easily deduce the dependence on experimental parameters. Hence, a special case referred to as “unidirectional flow” is considered. Unidirectional flow can be interpreted as the limiting case of very wide magnets where

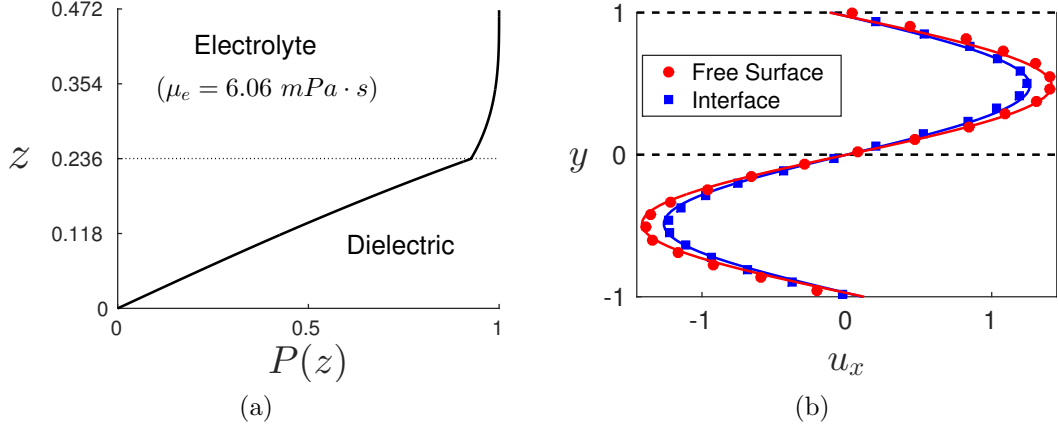


Figure 3.6: (a) Analytical results for the vertical profile of the horizontal flow field in both layers. The ratio of the velocities, as defined by equation (3.13), is  $S = 1.08$ . (b) Experimental measurements of the horizontal flow profile taken separately at the electrolyte free surface (red circles) and at the electrolyte-dielectric interface (blue squares). PIV measurements are plotted for the time-independent laminar flow near the center of the magnet array. A sine wave with fixed periodicity is fit to each data set. In both (a) and (b),  $h_d = h_e = 0.236$  and the electrolyte layer has viscosity  $\mu_e = 6.06 \text{ mPa}\cdot\text{s}$ . Uncertainties in (b) are the size of the symbols or smaller.

the  $y$ -dependence of the magnetic field  $B_z$  is ignored (i.e.,  $\kappa \rightarrow 0$ ).

The analysis of unidirectional flow, as well as a justification for its consideration, are not presented here for the sake of brevity, but instead included in Appendix B. The results of the analysis suggest that the most straightforward way to enhance the two-dimensionality of the flow in the electrolyte is by increasing the ratio of viscosities,  $\mu_e/\mu_d$ . For this reason, throughout the work presented in this dissertation, an electrolyte that is approximately 4.5 times more viscous than the dielectric is used. The analytical solution for  $P(z)$  corresponding to an electrolyte with  $\mu_e = 6.06 \text{ mPa}\cdot\text{s}$  is shown in Figure 3.6 (a). By conducting two separate experiments in which the flow is seeded at the free surface or at the electrolyte-dielectric interface, as shown in Figure 3.6 (b), the corresponding value of  $S = 1.08$  is verified to within 1%. Furthermore, it is confirmed that the flow in the electrolyte is much closer to being uniform along the vertical direction.

### 3.2.4 Evaluation of Parameters from Experimental Quantities

The parameters  $\beta$ ,  $\bar{\rho}$ ,  $\bar{\nu}$ , and  $\alpha$  in equation (3.9), as well as  $S$ , are evaluated using the analytical expressions provided in equation (3.10), with the form of the vertical profile  $P(z)$  as described in the previous section. By directly substituting the experimental quantities presented in Section 3.1.2 while evaluating the integrals in a piecewise manner in order to account for the inhomogeneity of the two distinct layers, the following parameters are obtained:  $\beta = 0.830$ ,  $\bar{\rho} = 976.4 \text{ kg/m}^3$ ,  $\bar{\nu} = 3.26 \times 10^{-6} \text{ m}^2/\text{s}$ ,  $\alpha = 0.0636 \text{ s}^{-1}$ , and  $S = 1.08$ .

## 3.3 Numerical Modeling

In this section, details of the numerical modeling based on equation (3.9) are presented. In Section 3.2.1, a perfectly sinusoidal forcing profile with a linear decay was assumed for the sake of analytical convenience in performing depth-averaging. However, in an effort to capture the form of the experimental forcing more accurately, a numerical model of the magnetic field is introduced in Section 3.3.1. Then, in Section 3.3.2, the boundary conditions which form the basis for three different numerical simulations are introduced. Details of the spatial and temporal discretizations, as well as the integration schemes employed in all three numerical simulations have been included in Appendix C.

### 3.3.1 Magnetic Field Modeling

As mentioned,  $\mathbf{f}$  is obtained by depth-averaging  $\mathbf{F}$ , which is a model of the Lorentz forces which drive the electrolyte in the experiment. These Lorentz forces arise from the interaction of the magnetic field  $\mathbf{B}$  with a current density  $\mathbf{J}$ . The current density is easily calculated from geometrical considerations, but the magnetic field generated by the array of permanent magnets is quite complicated. For  $\mathbf{J} = J\hat{\mathbf{y}}$ , as indicated in Figure 3.1, the Lorentz force density at any location  $(x, y, z)$  within the electrolyte

layer is given by  $\mathbf{F} = \mathbf{J} \times \mathbf{B} = JB_z\hat{\mathbf{x}} - JB_x\hat{\mathbf{z}}$ . Here,  $B_x$  and  $B_z$  are the  $x$ - and  $z$ -components of the magnetic field, respectively, which vary along all three coordinates  $x$ ,  $y$ , and  $z$ . Experimental measurements show that the typical value of  $B_x$  is less than 3% of the value of  $B_z$  at any given location within the electrolyte. Hence, the Lorentz force density for all practical purposes can be approximated as  $\mathbf{F} \approx JB_z\hat{\mathbf{x}}$ . Then, for the case of the two-immiscible-layer configuration, equation (3.11) can be rewritten as:

$$\mathbf{f} = \frac{1}{\bar{\rho}} \int_{h_d}^{h_d+h_e} \frac{JB_z(x, y, z) dz}{h_d + h_e} \hat{\mathbf{x}} \quad (3.14)$$

where  $B_z(x, y, z)$  is yet to be determined.

To characterize the magnetic field  $B_z(x, y, z)$  in the experiment, 3D measurements have been taken using a F. W. Bell Model 4048 handheld Gaussmeter and are plotted as the black symbols in Figure 3.7. Figure 3.7 (a) shows the experimental measurements of  $B_z$  along the line  $x = 0$ , passing above the center of the magnet array at two different heights. Clearly, this profile deviates significantly from that of a pure sinusoid, especially due near the edges of the array where the fringe fields are non-negligible. To obtain a magnetic field profile that closely resembles the one in the experiment, one could measure the  $z$ -component of the magnetic field ( $B_z$ ) across the entire flow domain at various heights above the magnet array. Using the measured field, the depth-averaged forcing profile could then be computed using equation (3.14). However, measuring  $B_z$  on a 3D grid is an extremely tedious process; hence, the following numerical model of the magnet array is used.

Recall that the magnets in the array are arranged such that adjacent ones have magnetization pointing in opposite directions, along  $\pm\hat{\mathbf{z}}$ . To obtain a magnetic field that closely resembles the one due to this array, each magnet is modeled as a 3D cubic lattice of identical dipoles, each with a moment  $m\hat{\mathbf{z}}$ . Changing the sign of  $m$  across adjacent magnets accounts for the alternating direction of magnetization. The

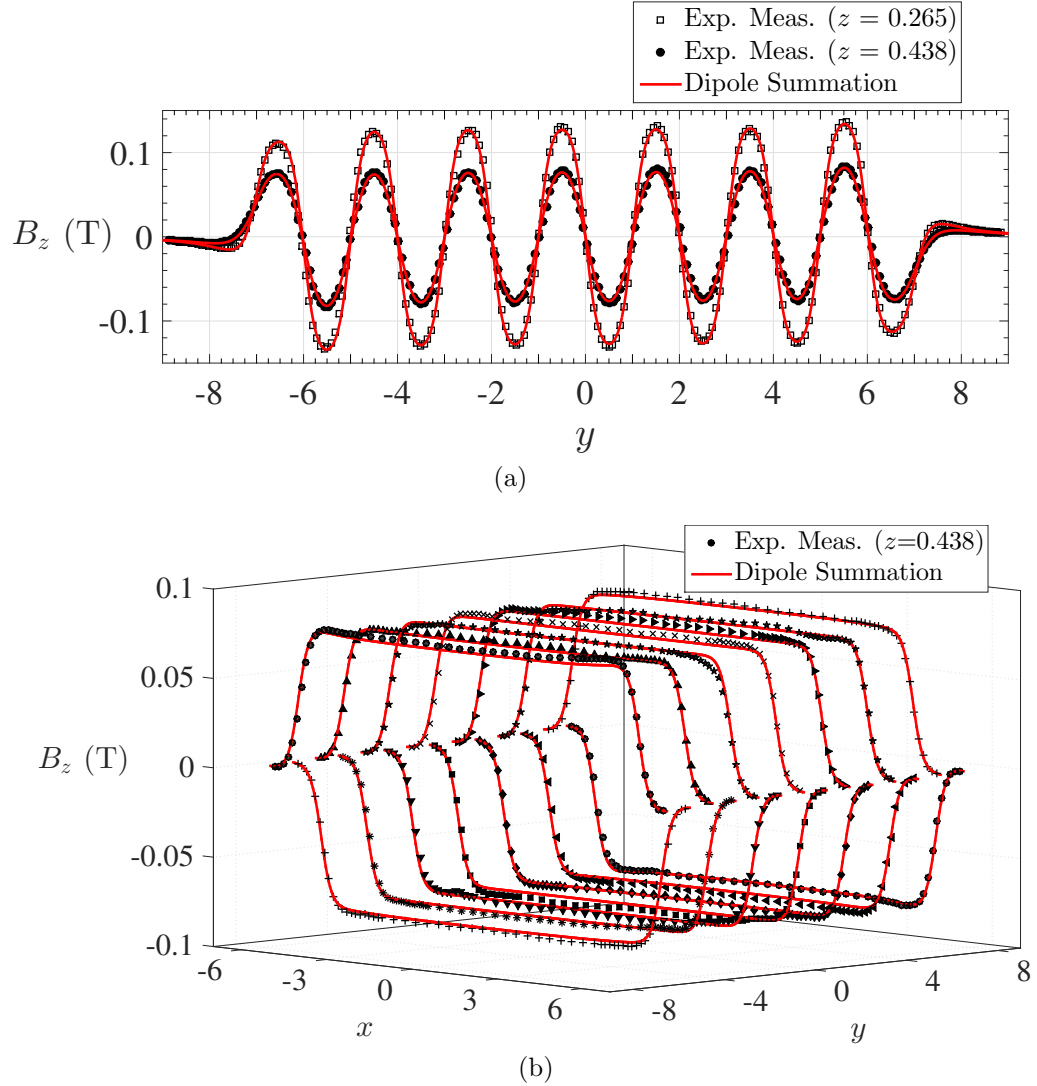


Figure 3.7: (a) Experimental measurements of the  $z$ -component of the magnetic field,  $B_z$ , as a function of  $y$  at the longitudinal center of the domain ( $x = 0$ ), and (b) experimental measurements of  $B_z$  along the magnet centerlines at  $y = \pm\{0.5, 1.5, 2.5, 3.5, 4.5, 5.5, 6.5\}$ . Measurements in (a) are taken at a height just above the dielectric-electrolyte interface at  $z = 0.236$  and just below the electrolyte free surface at  $z = 0.472$ . A least-squares fit has been performed using the data in (a) to determine the scaling factor for the dipole summation; the scaled dipole summation magnetic field is shown in red. The experimental uncertainties are the size of the symbols or smaller.

magnetic field at any location  $(x, y, z)$  above the array is then approximated using the linear superposition of the field contribution from all of the dipoles modeling the array. Hence, this model is referred to as the “dipole summation.” Since the strength of the dipole  $m$  cannot be measured experimentally, a single scaling parameter is calculated from a least-squares fit with the experimental measurements, taken at two heights. The rescaled dipole summation magnetic field is shown in Figure 3.7 (a) (red lines), along with the experimental measurements of  $B_z$  (black symbols), corresponding to the line  $x = 0$  at heights  $z = 0.265$  and  $z = 0.438$ . Figure 3.7 (b) shows the magnetic field comparison at  $z = 0.438$  along the magnet centerlines. Note that the electrolyte layer in the experiment is bounded by the planes  $z = 0.236$  and  $z = 0.472$ . Hence, the magnetic field  $B_z(x, y, z)$  is computed using the dipole summation at various heights, in steps of 0.0197, in the region  $0.236 < z < 0.472$  and depth-averaged using a discrete version of expression (3.14).

### 3.3.2 Boundary Conditions for Direct Numerical Simulations

In the experimental Kolmogorov-like flow, vertical solid walls serve as the lateral boundaries, resulting in a no-slip boundary condition. However, for reasons of analytical and computational feasibility, Kolmogorov flow has been studied almost exclusively using unbounded or periodic domains. Neither an infinite lateral extent nor periodicity offer a realistic representation of the effect of boundary conditions in the experiment, as far as the flow’s structure and its stability are concerned. To explore the role of boundaries, Chapter 4 focuses on comparisons between the experiment and numerical simulations which use three different computational domains with increasing degrees of confinement. These three different computational domains are described below.

- Doubly-Periodic Domain: This computational domain is chosen to coincide with the central  $8w \times 8w$  region of the experimental domain, with its boundaries

coinciding with  $x = \pm 4$  and  $y = \pm 4$ . The simulated flow is constrained to be periodic in both the longitudinal and transverse directions, i.e.  $\mathbf{u}(x = -4, y) = \mathbf{u}(x = 4, y)$  and  $\mathbf{u}(x, y = -4) = \mathbf{u}(x, y = 4)$ . Along the transverse direction it spans a width equaling that of 8 magnets. The 2D forcing profile  $\mathbf{f}$  over this doubly-periodic domain is constructed from the depth-averaged magnetic field presented in Section 3.3.1 by retaining only the two dominant Fourier modes,  $\sin(\kappa y)$  and  $\sin(3\kappa y)$ , along the  $y$ -direction; along the  $x$ -direction the profile is uniform. This gives  $\mathbf{f}(x, y) = 0.95 \sin(\kappa y) \hat{\mathbf{x}} + 0.05 \sin(3\kappa y) \hat{\mathbf{x}}$ .

- **Singly-Periodic Domain:** This computational domain coincides with the region  $-7 \leq x \leq 7$  and  $-4 \leq y \leq 4$ . The longitudinal dimension is the same as that of the experiment, while the transverse one spans a width equaling that of 8 magnets, like in the doubly-periodic domain. No-slip boundary conditions are imposed at the end walls, i.e.  $\mathbf{u}(x = \pm 7, y) = 0$ , while periodic boundary conditions are imposed along the transverse direction, i.e.  $\mathbf{u}(x, y = 4) = \mathbf{u}(x, y = -4)$ . The 2D forcing profile  $\mathbf{f}$  over this singly-periodic domain is constructed as a product of two one-dimensional profiles. Along the  $y$ -direction the profile is once again constructed by retaining only two dominant Fourier modes,  $\sin(\kappa y)$  and  $\sin(3\kappa y)$ , of the depth-averaged magnetic field. Along the  $x$ -direction the profile is chosen to be the depth-averaged magnetic field profile along the magnet centerline  $y = 0.5$ . It is noted that the effect of transverse confinement has been studied by Thess [156], and therefore is not investigated here separately.
- **Non-Periodic Domain:** This computational domain is identical to the experimental one in both lateral dimensions, i.e.  $-7 \leq x \leq 7$  and  $-9 \leq y \leq 9$ , with no-slip boundary conditions imposed at both the end walls and side walls, i.e.  $\mathbf{u}(x = \pm 7, y) = 0$  and  $\mathbf{u}(x, y = \pm 9) = 0$ . As mentioned earlier in Section

3.3.1, the forcing over this domain is computed from depth-averaging the dipole summation.

To compare experimental observations with those predicted by equation (3.9) with the three types of boundary conditions described above, direct numerical simulations have been performed. The flow over the doubly-periodic domain is simulated using a pseudo-spectral method in the vorticity-stream function formulation, as described in [157]. This simulation is henceforth referred to as the “doubly-periodic simulation,” abbreviated DPS. For the singly-periodic and the non-periodic domains, numerical simulations have been performed using a finite-difference scheme, described in [158]. These simulations are hereafter referred to as the “singly-periodic simulation” (SPS) and the “non-periodic simulation” (NPS).

## CHAPTER IV

### PRIMARY AND SECONDARY INSTABILITIES OF KOLMOGOROV-LIKE FLOW

This chapter presents a comparison between experimental PIV measurements and direct numerical simulations for low Reynolds numbers. The simulations are based on equation (3.9) using the three domains described in Section 3.3.2. There are two primary goals in presenting the comparisons made in this chapter. The first is to show that equation (3.9), in comparison to equation (2.5), provides a more accurate description of a Q2D flow. Secondly, and more importantly, this chapter serves to demonstrate that quantitative agreement can be obtained between experiment and carefully modeled numerical simulations in the study of a Kolmogorov-like flow. This bifurcation study sets a solid foundation for the search for ECS which is presented in Chapter 5.

This chapter is organized as follows. First, the straight uniform flow which is found at low Reynolds numbers is presented, with a special emphasis on the effect of boundaries. Then, linear stability analysis is performed to demonstrate that equation (3.9) predicts the primary instability more accurately than equation (2.5), but still substantially undershoots the experimentally observed critical Reynolds number. Next, the primary instability in the experiment and simulations is characterized, along with the secondary steady flow state which is observed. Finally, the secondary instability which gives rise to a time-periodic flow is presented.

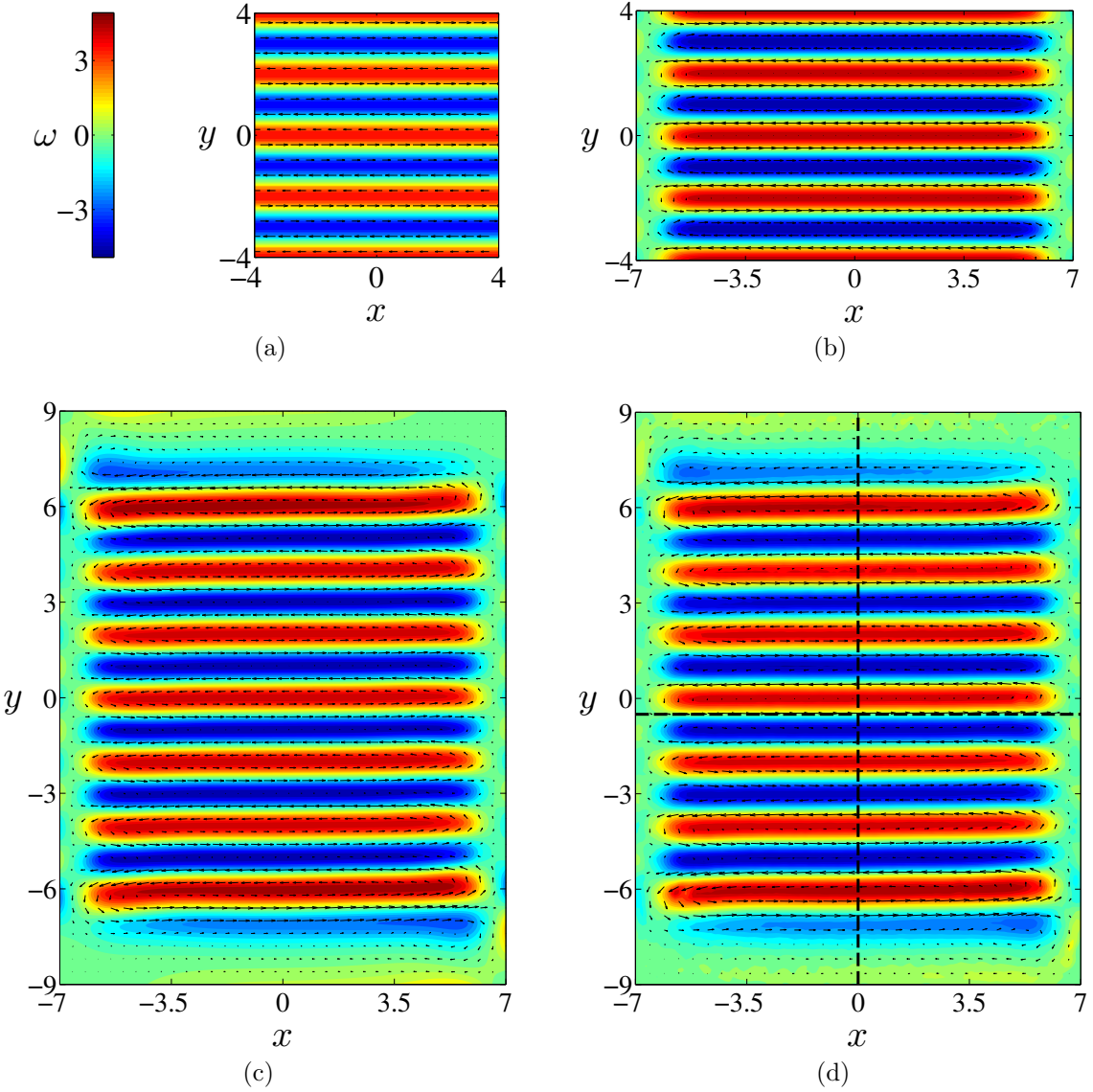


Figure 4.1: Straight flow fields at  $Re = 8.1$  for the (a) DPS, (b) SPS, (c) NPS, and (d) experiment. The dashed lines in (d) indicate the locations of velocity profiles that are compared to the simulations in Figure 4.2. The vorticity color scale plotted for (a) also applies to (b-d). The velocity vectors are downsampled in each direction by a factor of 8 for the simulations and a factor of 4 for the experiment.

## 4.1 Straight Flow

For low driving the flow mimics the forcing closely, resulting in spatially alternating bands of fluid flow along the  $\pm x$ -directions, as can be seen in Figure 4.1. In this figure, black vectors correspond to the velocity field  $\mathbf{u}$  and the color indicates the vorticity  $\omega = (\nabla \times \mathbf{u}) \cdot \hat{\mathbf{z}}$ . For the experiment (Figure 4.1 (d)), the  $y$ -component of the velocity measured near the center of the domain is close to zero. However, there are regions of strong recirculation near the end walls, characterized by a nonzero  $y$ -component of velocity. Additionally, a careful observation of the flow shows a slight tilt in the alignment of the flow bands. This tilt is due to the global circulation, resulting from confinement and the fluid flowing in opposite directions over the end magnets at  $y = \pm 6.5$ . Figures 4.1 (a) and (b) show the straight flows found in the DPS and SPS at  $Re = 8.1$ . It can be seen that flow fields in the DPS and SPS reproduce the experimental flow qualitatively away from the lateral walls. Furthermore, the SPS captures the turnaround flow near the end walls. However, neither the SPS nor the DPS displays the tilt of the flow bands observed in the experiment since the periodic flows are devoid of global circulation. In contrast, the NPS generates a flow field that looks indistinguishable from the experimental one (cf. Figure 4.1 (c)).

For a quantitative description of the straight flow profile, the longitudinal component  $u_x^{exp}$  of the velocity along the line  $x = 0$  in the experiment is plotted in Figure 4.2 (a). The location of this cross section is indicated by the vertical dashed line in Figure 4.1 (d). The difference in  $u_x$  between the experiment and the numerical simulations along this line is shown in Figure 4.2 (b). As can be seen, the DPS and SPS, which are only defined for  $|y| < 4$ , show systematic deviation from the experiment as high as 18% since they do not capture the tilt in the shear bands which results from global circulation. In comparison, the NPS agrees to within about 5% over the same region, with no clear systematic deviation. The disagreement between the experiment and NPS in this region, we believe, is a result of the dipole summation not accounting

for the variation in the strength of each individual magnet. Closer to the boundaries, at  $y \approx 7$  and  $y \approx -6$ , the largest difference between the NPS and the experiment is around 12%.

The experimental longitudinal velocity component  $u_x^{exp}$  at  $y = -0.5$  (along a central magnet centerline) is shown in Figure 4.2 (c). The very slight asymmetry in the longitudinal velocity is a result of the global circulation. In contrast, the flow in the DPS is perfectly uniform and thus does not capture this asymmetry, as can be seen from the plot of its difference with the experimental profile in Figure 4.2 (d). The SPS, which is defined all the way to the end walls, also does not capture this asymmetry, as the flow in the SPS is also devoid of global circulation. The NPS produces the closest agreement: the corresponding flow displays the asymmetry observed in the experiment, with no significant systematic deviation. In summary, the NPS succeeds in capturing the effects of confinement in the experiment with good accuracy, while the DPS and SPS show significant systematic deviations.

## 4.2 Linear Stability Analysis

As the strength of the forcing increases, the flow in the experiment undergoes a qualitative change at  $Re_c = 11.07 \pm 0.05$ , with uniform flow bands developing spatial modulation that eventually gives rise to distinct stationary vortices (cf. Figure 4.2 (d)). Hence, this flow is referred to as the “modulated flow.” Several previous experimental studies have reported this transition and have characterized it using the critical Reynolds number ( $Re_c^{exp}$ ) and wavenumber ( $k_c^{exp}$ ) of the longitudinal modulation [101, 116, 159]. In the experiments reported here, the wavenumber just above this transition was measured to be  $k_c^{exp} = 0.50\kappa$ . In virtually all previous studies, theoretical estimates for these critical parameters have been obtained by using equation (2.5) and modeling the straight flow in the experiment as a strict sinusoid

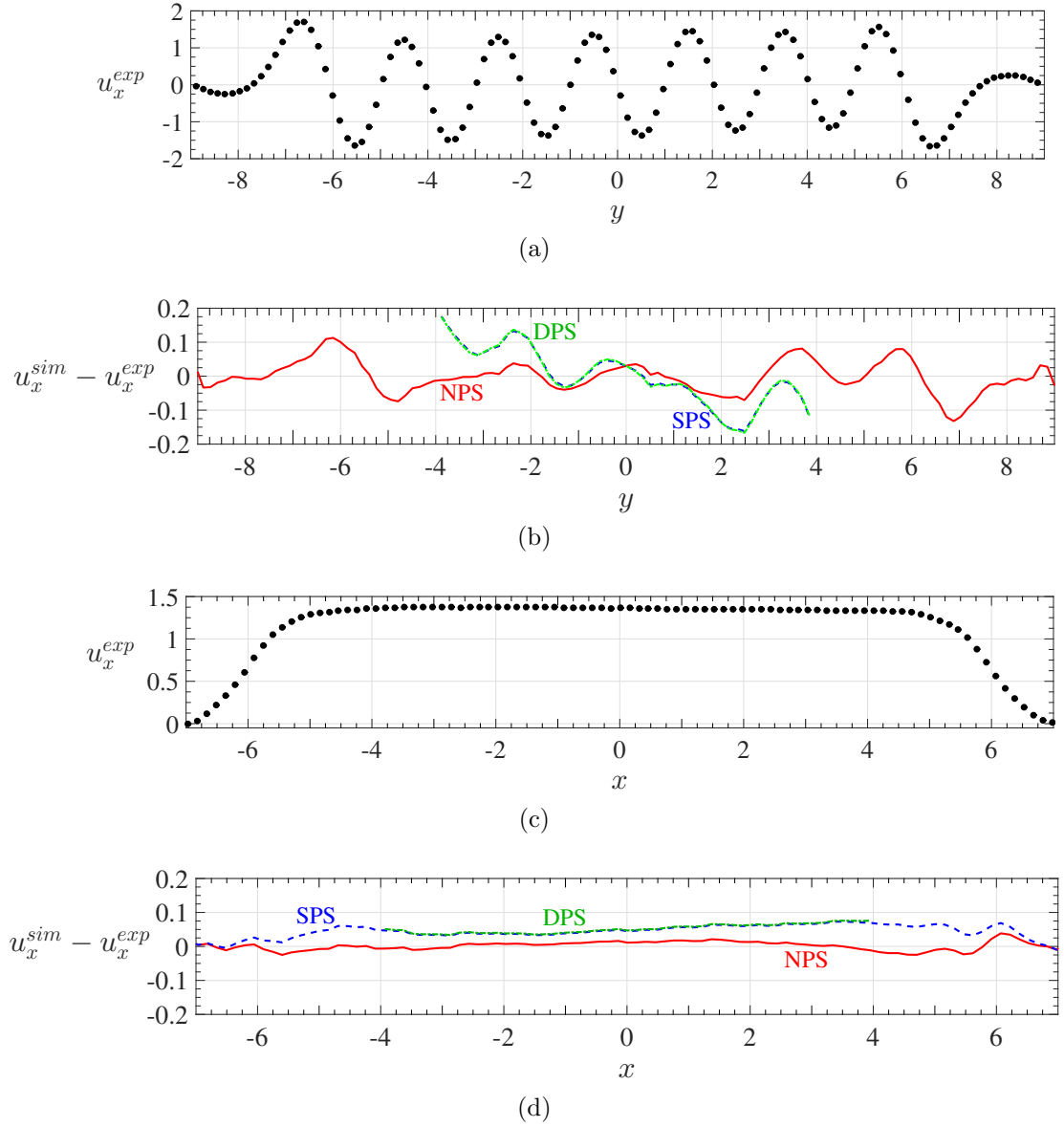


Figure 4.2: Profiles of the longitudinal velocity and longitudinal velocity differences at  $Re = 8.1$ . (a)  $u_x^{exp}$  as a function of  $y$  at the longitudinal center ( $x = 0$ ), (b) the difference between the longitudinal velocity in the simulations and the experiment,  $u_x^{sim} - u_x^{exp}$ , as a function of  $y$  at the longitudinal center ( $x = 0$ ); note that the curves corresponding to the DPS and SPS are virtually indistinguishable, (c)  $u_x^{exp}$  as a function of  $x$  at the centerline of a middle magnet ( $y = -0.5$ ), and (d) the difference between the longitudinal velocity of the simulations and the experiment,  $u_x^{sim} - u_x^{exp}$ , as a function of  $x$  at the centerline of a middle magnet ( $y = -0.5$ ); note that the curves corresponding to the DPS and SPS are virtually indistinguishable in the region  $|x| < 4$ , where the DPS is defined. Experimental uncertainties are the size of the symbols or smaller.

$\mathbf{u}_{\text{str}} \propto \sin(\kappa y)$ ; the flow stability is then analyzed with respect to longitudinal perturbations  $\delta \mathbf{u}(y) e^{ikx}$ . In this section, this analytical approach is revisited for equation (3.9) to provide estimates for the critical parameters. Many previous studies have used a different nondimensionalization, which corresponds to  $\kappa = 1$ . To make comparison easier, a scaled wavenumber  $q = k/\kappa$  is used which corresponds to the convention followed in those studies.

The strictly sinusoidal straight flow governed by equation (3.9) on an unbounded domain becomes unstable with respect to perturbations of longitudinal wavelength  $q$  above the Reynolds number  $Re = Re_n(q)$ , which to a very good accuracy is given by:

$$Re_n(q) = \frac{\pi}{\beta} \frac{1}{q} \sqrt{\frac{(1+q^2)}{(1-q^2)} \left( q^2 + \frac{\alpha}{\nu \kappa^2} \right) \left( 1+q^2 + \frac{\alpha}{\nu \kappa^2} \right)}. \quad (4.1)$$

This expression was computed by linearizing equation (3.9) around  $\mathbf{u}_{\text{str}}$  and calculating its stability with respect to perturbations  $\delta \mathbf{u}(y) e^{ikx} = \sum_{n=-1,0,1} \epsilon_n e^{i\kappa(ny+qx)}$  including three dominant modes [160]. The critical Reynolds number  $Re_c = \min_q Re_n(q)$  and the corresponding critical wavenumber  $k_c = \kappa q_c$  computed using the above expression can then be compared with experimental observations.

The neutral stability curve (blue dot-dashed line) which corresponds to the experimental values of parameters  $\alpha$ ,  $\beta$ , and  $\bar{\nu}$  is shown in figure 4.3. The minimum of this neutral stability curve yields a critical Reynolds number  $Re_c = 9.16$  and an associated critical wavenumber  $q_c = 0.465$ . The black dot on the plot indicates the critical values  $Re_c^{\text{exp}} = 11.07$  and  $q_c^{\text{exp}} = 0.50$ , corresponding to the instability observed in the experiment. The relative difference  $(Re_c^{\text{exp}} - Re_c)/Re_c^{\text{exp}}$  between the theoretical estimate for the critical Reynolds number and that measured in experiment is about 17%. The critical wavenumber, however, is in better agreement with the experimentally measured one, with a 7% relative error.

While the critical Reynolds number obtained from the linear stability analysis disagrees substantially with the experimentally observed one, it is still a significant improvement over analytical estimates for a flow modeled using equation (2.5), which

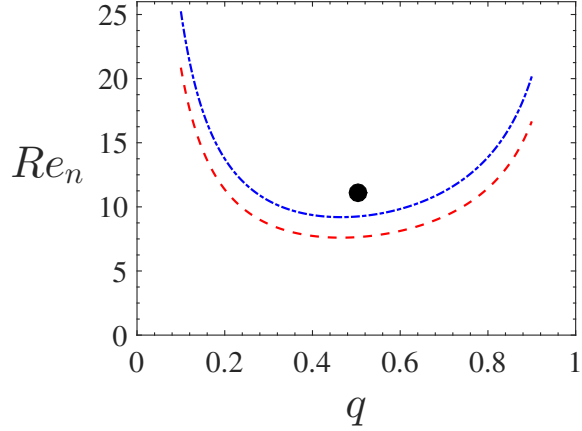


Figure 4.3: Neutral stability curves (4.1) showing the Reynolds number  $Re_n$  at which the straight flow in an unbounded domain goes unstable when subjected to a perturbation of longitudinal wavenumber  $q$ . The red dashed line corresponds to  $\alpha = 0.064 \text{ s}^{-1}$  and  $\beta = 1.00$ , while the blue dot-dashed line corresponds to  $\alpha = 0.064 \text{ s}^{-1}$  and  $\beta = 0.83$ . The black circle shows the corresponding measurement from the experiment. In all cases,  $\bar{\nu} = 3.26 \times 10^{-6} \text{ m}^2/\text{s}$  is held constant.

corresponds to setting  $\beta = 1$  in equation (3.9). The corresponding neutral stability curve is indicated by the red dashed line in figure 4.3. From equation (4.1) it can be seen that the entire neutral stability curve scales as  $1/\beta$ . This implies that the critical wavenumber ( $q_c = 0.465$ ) is independent of  $\beta$ , while the predicted critical Reynolds number for  $\beta = 1$  is  $Re_c = 7.60$ . This is a 31% discrepancy with the experimental value, which is comparable to the 30% discrepancy reported by Bondarenko *et al.* [101] in a study based on equation (2.5).

It is noted that the increase in the stability of the straight flow for  $\beta < 1$  is due to the vertical gradient in the magnitude of horizontal velocity, which results in a reduction of the effective inertia and nonlinearity of the flow. Equation (2.5), in contrast, does not account for this reduction. As is shown in the next section, the remaining discrepancy can be substantially improved by imposing lateral boundaries.

### 4.3 Primary Instability and Modulated Flow

Figure 4.4 (a-d) shows the modulated flow fields corresponding to the DPS, SPS, NPS, and experiment, respectively, at  $Re = 14$ . At this Reynolds number the modulated

flow is well developed and is visually quite distinct from the straight flow. The counterclockwise global circulation in the experiment strongly affects the alignment of the vortices (see Figure 4.4 (d)) as can be seen by comparing the modulated flows in the DPS and SPS with the relevant regions of the experimental flow. It should be noted that the size of the DPS domain along  $x$  was chosen *a posteriori* to be commensurate with the critical longitudinal wavenumber  $q_c^{exp} = 0.50$ . However, once again, the flow field in the NPS captures the features observed in the experiment remarkably well. This unambiguously demonstrates the importance of properly modeling the confinement effects in both the longitudinal and the transverse direction to reproduce the features of the flow in the experiment.

This transition to the modulated flow is characterized by the appearance of the transverse component of velocity throughout the flow domain,  $u_y \neq 0$ . As the driving is increased, the magnitude of  $u_y$  also increases. A bifurcation diagram characterizing the transition from the straight to the modulated flow is shown in Figure 4.5 (a). The order parameter is the spatial mean square transverse velocity,  $\langle u_y^2 \rangle$ , which is plotted as a function of  $Re$ . The spatial average is computed over the central region  $|x| < 4$  and  $|y| < 4$  for all simulations and the experiment. In comparison to the experimental value of  $Re_c^{exp} = 11.07$ , the primary bifurcation in the DPS and SPS occurs at much lower Reynolds numbers  $Re_c = 9.39$  and  $Re_c = 9.64$ , respectively. This result shows that imposing realistic boundary conditions in the longitudinal direction alone cannot capture the instability of the straight flow. In contrast, by imposing the correct (no-slip) boundary conditions in both the longitudinal and transverse directions, in addition to using a realistic model of the magnetic field, the primary instability can be predicted quite accurately: the transition in the NPS occurs at  $Re_c = 10.73$ , which is within 3% of  $Re_c^{exp}$ . Note that setting  $\beta = 1$  results in a much poorer prediction  $Re_c = 8.91$  even in the NPS, which corresponds to a 20% error.

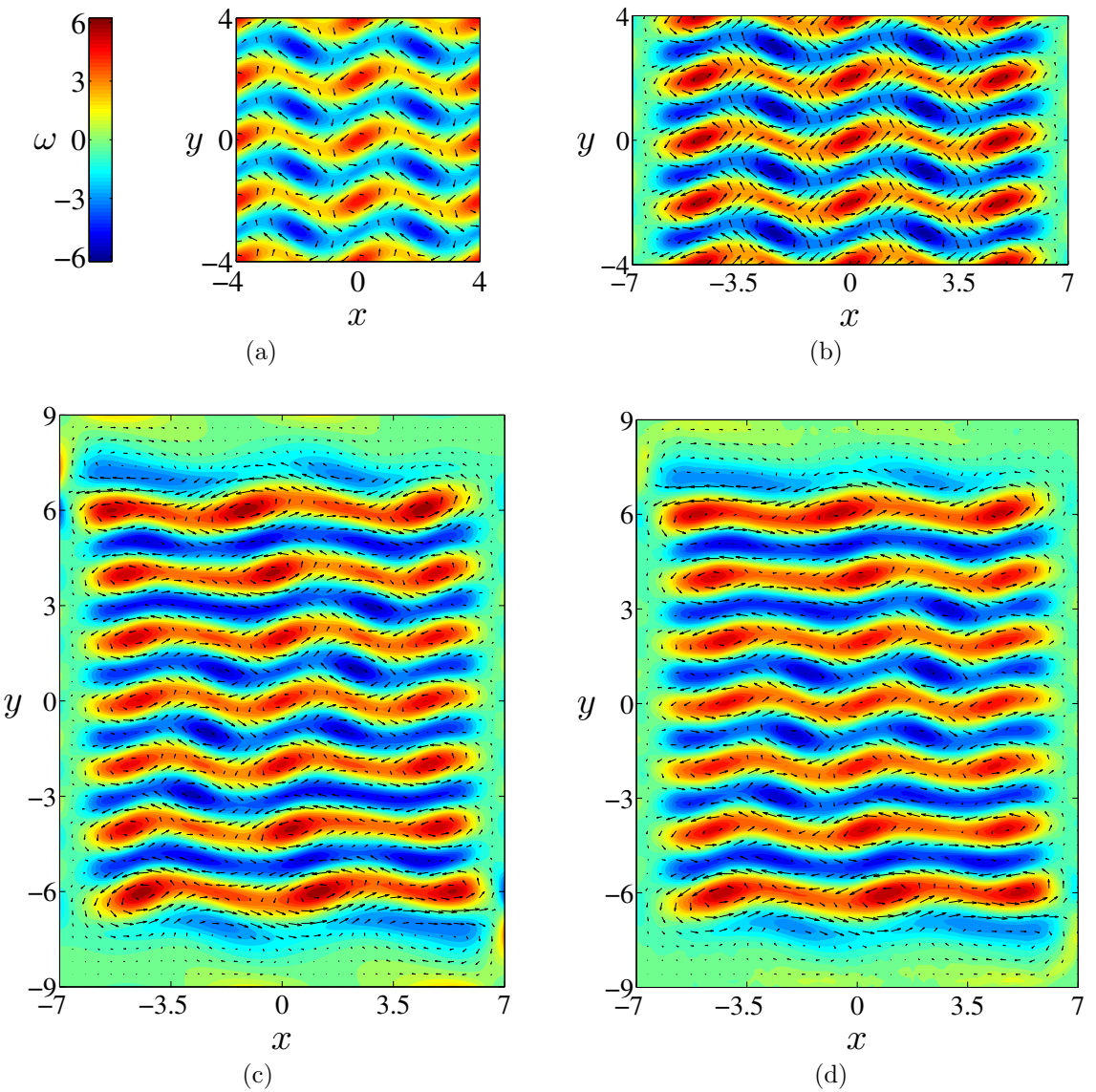


Figure 4.4: Modulated flow fields at  $Re = 14$  for the (a) DPS, (b) SPS, (c) NPS, and (d) experiment. The vorticity color scale plotted for (a) also applies to (b-d). The velocity vectors are downsampled in each direction by a factor of 8 for the simulations and a factor of 4 for the experiment.

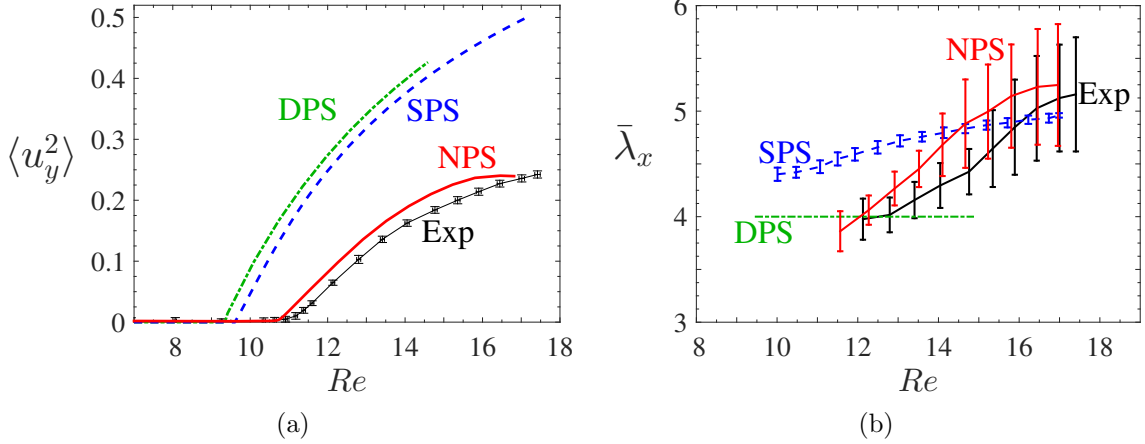


Figure 4.5: (a) A bifurcation diagram showing the primary instability for the experiment and simulations, and (b) the spatial average of the longitudinal wavelength,  $\bar{\lambda}_x$ , as a function of  $Re$  for the modulated flow regime. At each  $Re$ , wavelength measurements are made for  $|y| < 4$  then averaged; the uncertainty bars indicate one standard deviation in the spatial measurements.

Another measure that facilitates a quantitative comparison between the experiment and the simulations is the average longitudinal wavelength  $\bar{\lambda}_x$  associated with the vortex pattern of the modulated flow. This wavelength is defined as a spatial average computed by measuring the separation between adjacent vortex centers in the central region of the domain  $|y| < 4$ . Just above the initial instability, the vortices in the experiment form a lattice with a fairly uniform separation,  $\bar{\lambda}_x^{exp} = 4.0$ . As the forcing is increased, the mean separation between the vortices increases, as can be seen from the plot of  $\bar{\lambda}_x$  versus  $Re$  shown in Figure 4.5 (b). Additionally, at higher forcing, the vortex lattice becomes spatially irregular, as can be seen in Figure 4.4 (d). This spatial variation is quantified in the plot in Figure 4.5 (b) wherein the uncertainty bars indicate one standard deviation in the spatial variation of the separation between adjacent vortices. For comparison, Figure 4.5 (b) also shows the wavelength measured in the DPS and SPS. The DPS does not capture the spatial variation of the wavelength or its variation with  $Re$ . The SPS, however, shows a qualitatively similar trend for the mean wavelength dependence on the Reynolds number. The periodicity in the transverse direction results in a uniform vortex pattern with smaller spatial

variation in the separation between vortices compared to the experiment. In contrast, the NPS captures both the spatial variation of the wavelength and the distortion of the lattice with increasing forcing quite well. The wavelength shortly above the initial instability agrees with that of the experiment to within about 0.1 (2.5%), but for a given Reynolds number, the NPS overestimates the wavelength compared to what is observed in the experiment. The largest discrepancy, which is almost 11%, occurs around  $Re = 15$ . Note that at onset of the modulated flow, the average wavelength in the experiment is used to define the critical wavenumber  $k_c^{exp} = 2\pi/\bar{\lambda}_x = 1.58 \pm 0.081$  (which corresponds to  $q_c^{exp} = 0.50 \pm 0.026$ ).

Careful analysis shows that while in the DPS and SPS the transition from straight to modulated flow corresponds to a supercritical pitchfork bifurcation, the transition in the experiment and NPS is described by an imperfect pitchfork bifurcation. In the experiment and NPS, no instability happens due to a weak symmetry breaking effect of the boundary conditions. A detailed discussion of the exact nature of the bifurcation in each of the three simulations is provided in [161].

#### **4.4 Secondary Instability and Time-Periodic Flow**

As the forcing is increased further, the modulated flow in the experiment becomes unstable at  $Re_s = 17.6 \pm 0.1$  giving way to a time-periodic flow with a period of  $42.8 \pm 0.4$  at onset (dimensionally,  $120 \pm 1$  s). The NPS similarly predicts a transition to a time-periodic flow with a period of 42.8, occurring at  $Re_s = 17.0$ . In contrast, the modulated flows from neither the DPS nor the SPS transition directly into a time-periodic flow; hence quantitative comparison of the secondary instability for the DPS and SPS is not provided here. To quantify this transition in the experiment and NPS, a bifurcation diagram is shown in Figure 4.6 (a) which plots the peak intensity  $I$  of the temporal power spectrum spatially averaged over the region  $|x| < 4$  and  $|y| < 4$  as a function of  $Re$ . The associated power spectra are shown in Figure 4.6 (b). Note that

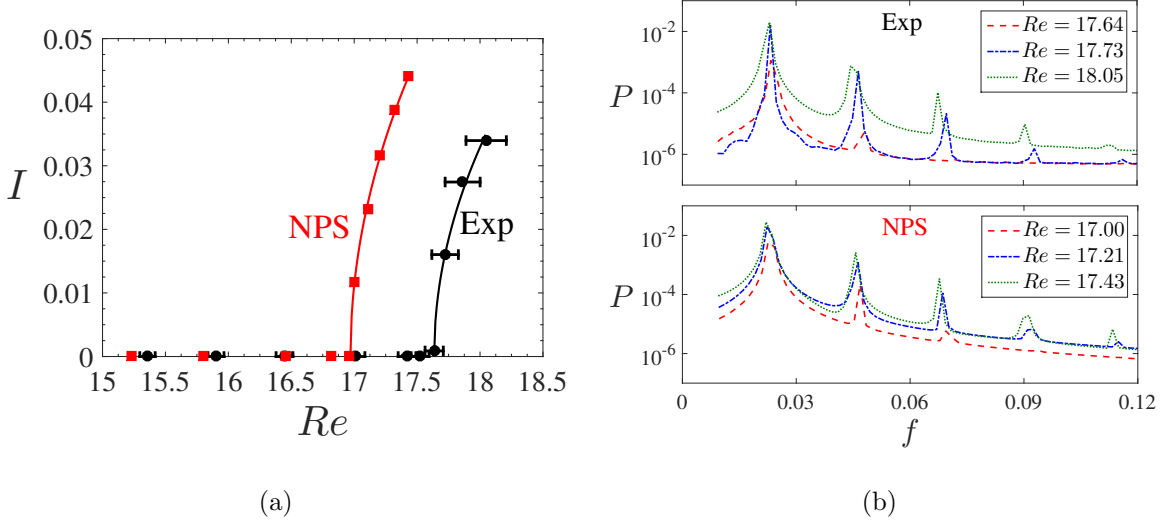


Figure 4.6: (a) A bifurcation diagram showing the power spectrum peak intensity  $I$  as a function of  $Re$ , and (b) the temporal power spectrum  $P$  as a function of the frequency  $f$  for the experiment (top) and NPS (bottom) as  $Re$  is increased. The temporal power spectrum is averaged over the region  $|x| < 4$  and  $|y| < 4$  before calculating the intensity  $I$ . This transition, which occurs at  $Re_s = 17.6$  in the experiment and  $Re_s = 17.0$  in the NPS, corresponds to the flow transitioning from the modulated flow to a time-periodic flow.

the critical Reynolds number characterizing this bifurcation in the NPS agrees with the experimental observations to within 4%, and the same nondimensional oscillation period (to one decimal place) is observed.

As the driving is increased further, the amplitude of the oscillations grows while the period remains approximately constant. Figure 4.7 shows two snapshots of the time-periodic flow fields from the experiment (left) and the NPS (right). The most apparent oscillatory feature is the motion of the central diagonal band of red vortices; as the oscillations repeat, the vortices forming this band collectively move towards the line  $x = 0$ , then away from the line  $x = 0$ , repeatedly. The flow fields shown in this figure correspond to  $Re = 17.9$  for the experiment and  $Re = 17.2$  for the NPS, which is approximately the same distance in  $Re$  above the bifurcation in each case.

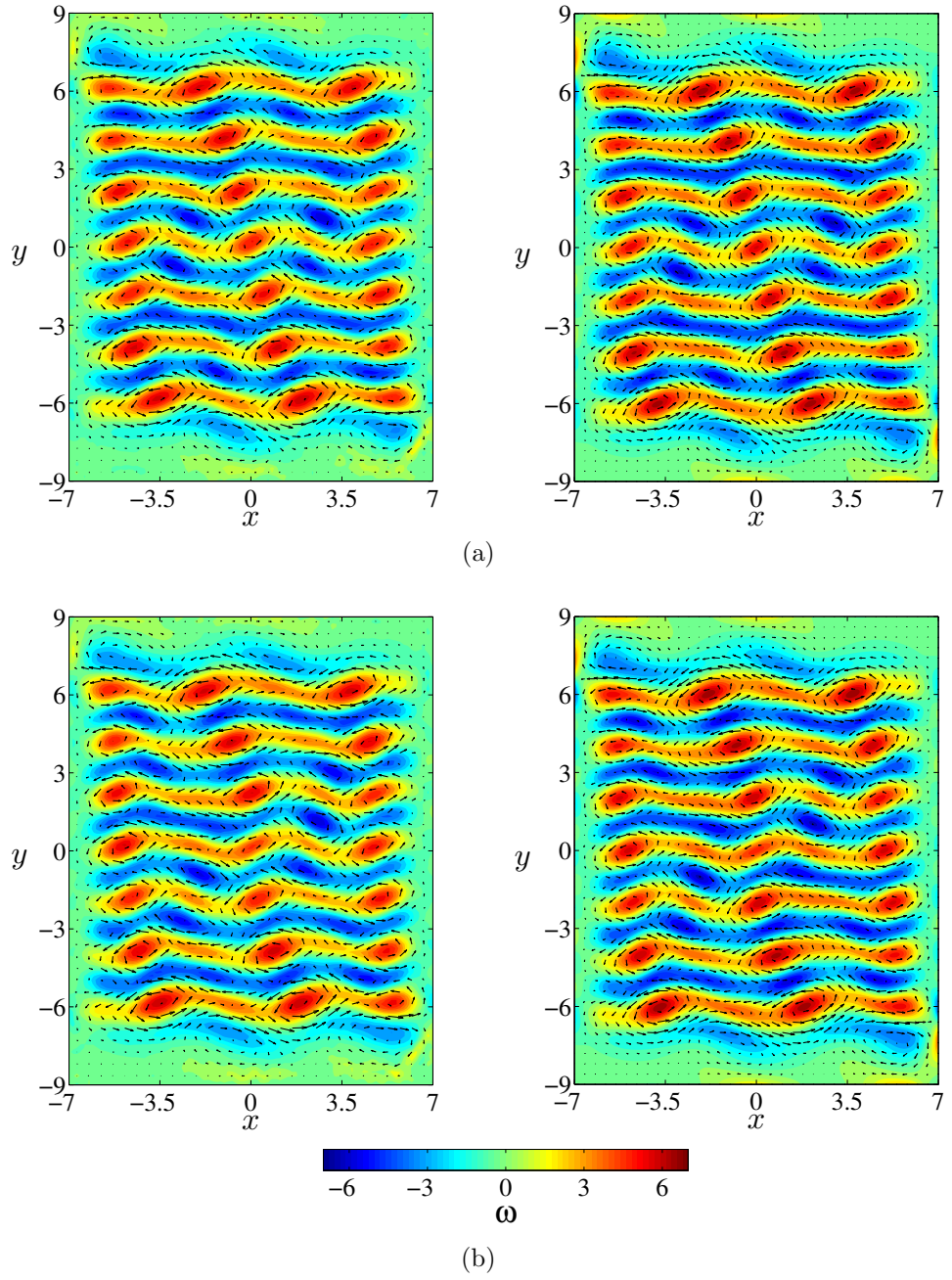


Figure 4.7: Two snapshots of the experimental (left) and NPS (right) flow fields in the time-periodic regime. The vorticity color scale plotted for (b) also applies to (a). The velocity vectors are downsampled in each direction by a factor of 8 for the simulations and a factor of 3 for the experiment.

## 4.5 Discussion

This chapter has presented an analysis of the first three flow regimes observed in a Kolmogorov-like flow as  $Re$  is increased. This analysis has been made by directly comparing experimental PIV measurements with numerical simulations. In particular, comparisons have been made with three different numerical simulations (the DPS, SPS, and NPS) to test the importance of confinement and lateral boundary conditions in modeling the flow. The results indicate that it is necessary to incorporate realistic, no-slip boundary conditions at both of the lateral boundaries and a realistic forcing profile (as is the case for the NPS) to obtain close, quantitative agreement with the experiment. Specifically, the NPS predicts the Reynolds number  $Re_c$  for the primary instability to within 3%; the critical Reynolds number  $Re_s$ , as well as the period at the onset of the time-periodic state, are predicted to within 2%.

It is emphasized that this is the first study to incorporate equation (3.9), along with the analytical expressions (3.10) which use experimentally measured fluid layer properties, for modeling the flow. It is worth noting that even with the proper boundary conditions and a realistic model of the forcing profile, the use of equation (2.5) would result in a discrepancy of about 20% between experiment and simulation for both  $Re_c$  and  $Re_s$ . This is because equation (2.5) does not account for the suppression of the effective nonlinearity (i.e.,  $\beta = 1$ ). The analysis presented in this chapter also provides the first quantitative description of the secondary instability of a Kolmogorov-like flow.

Most importantly, these results demonstrate that the NPS, based on equation (3.9), can be used to quantitatively capture the dynamics of this Q2D Kolmogorov-like flow which is realized in the laboratory. This close agreement in the preturbulent regime suggests that the NPS can be used to gain insight into the dynamics of weak turbulence found at higher Reynolds numbers. In particular, using this model, one can test for evidence of the existence and dynamical relevance of exact coherent

structures guiding the chaotic dynamics. This is the topic of the next chapter.

# CHAPTER V

## EXACT COHERENT STRUCTURES IN WEAKLY TURBULENT KOLMOGOROV-LIKE FLOW

In the previous chapter, it was demonstrated that PIV measurements from the Kolmogorov-like flow experiment agree quantitatively with the predictions of the NPS. This comparison was made for the first three flow regimes that are found as  $Re$  is increased, up to about  $Re = 17.5$ . Shortly above this Reynolds number, the system becomes weakly turbulent. This regime is the focus of the present chapter, with emphasis on identifying signatures of ECS, calculating ECS, and using ECS to forecast weak turbulence. The analysis herein is conducted at  $Re = 22.5$ .

### 5.1 *Weakly Turbulent Dynamics*

The weakly turbulent dynamics are characterized by the irregular merging and splitting of vortices throughout the flow domain as the system evolves in time. Figure 5.1 shows four sequential weakly turbulent flow fields from the experiment which are representative samples of the dynamical behavior in this regime. In this figure, between (a) and (b), the blue vortices in the top right-center merge and a blue vortex at the bottom center splits. From frame (b) to (c), the stretched blue vortices in top left further separate, and some red vortices near the very center of the domain begin to merge. Finally, from (c) to (d), the two rows of red vortices in the bottom right merge, as well as the two rows of blue vortices in top right. Experimental runs as long as 4800 characteristic time units (dimensionally, 3 hours) show that the system does not reach an asymptotic steady state. The temporal power spectrum for a time series that is 1600 characteristic time units long is shown in Figure 5.2. This broadband

spectrum suggests that the time series is indeed chaotic [33].

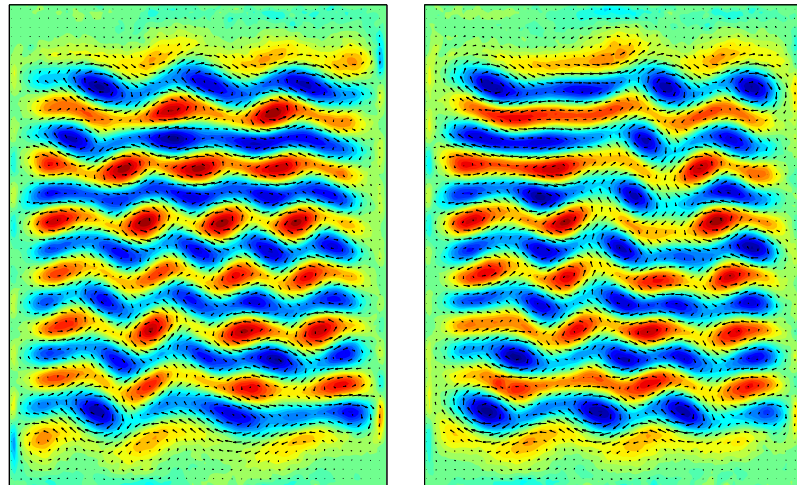
The rate of evolution of the experimental flow fields can be characterized by calculating the normalized autocorrelation time:

$$C(\Delta t) = \frac{\langle \Delta \mathbf{u}(t) \cdot \Delta \mathbf{u}(t + \Delta t) \rangle_t}{\langle \Delta \mathbf{u}(t) \cdot \Delta \mathbf{u}(t) \rangle_t}, \quad (5.1)$$

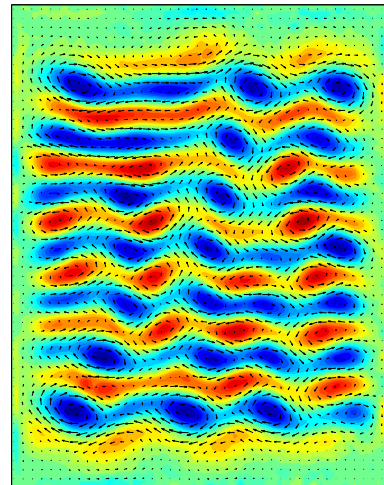
where  $\langle \cdot \rangle_t$  denotes temporal averaging and  $\Delta \mathbf{u}(t) = \mathbf{u}(t) - \langle \mathbf{u}(t) \rangle_t$ . The normalized autocorrelation is plotted with black circles in Figure 5.3. The autocorrelation time  $\tau$  is then defined such that  $C(\Delta t) = 1/e$  (dashed line in Figure 5.3), which yields  $\tau = 12$ . This longer time scale is in many ways a better choice than the nondimensionalization time scale  $w/U$  because it characterizes the average time required for the flow field to change. This time scale  $\tau$  will be used explicitly throughout this chapter to quantify the dynamics.

Having described a typical example of the weakly turbulent dynamics and having introduced a useful characteristic time scale, focus is now shifted to the goal of this chapter: to demonstrate how ECS can be used to characterize and even forecast weak turbulence. It is useful to imagine the evolution of this system as corresponding to a turbulent trajectory evolving in a high-dimensional state space. The reader is reminded that an introduction to this concept is available in Sections 1.3 and 2.1. Although this state space is in principle infinite-dimensional, the turbulent trajectory is expected to evolve (possibly, after some transient) on a finite-dimensional “inertial manifold” [28, 162], which allows for a drastically reduced description of the dynamics. The evolution of the turbulent trajectory on this inertial manifold is not arbitrary, but rather guided by the stable and unstable manifolds of the temporally-regular but unstable ECS (also introduced in Section 2.1). However, neither the structure of the inertial manifold nor the ECS are known *a priori*, but rather must be numerically calculated.

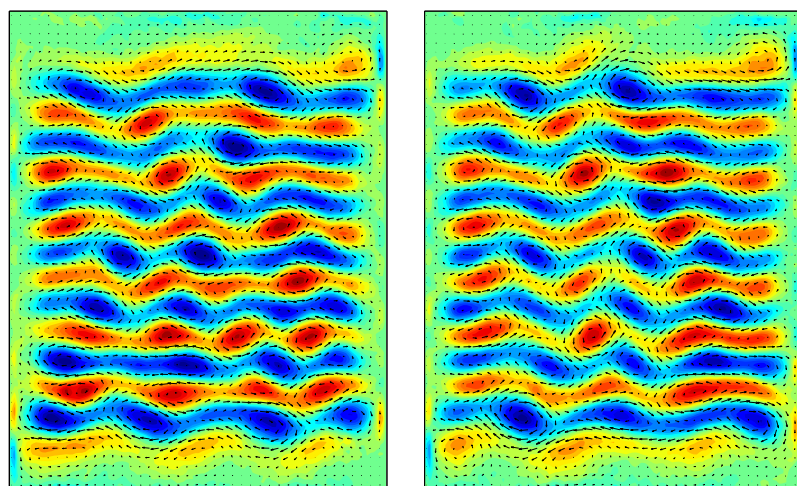
A first step towards building this fundamentally deterministic description of turbulence is to calculate such ECS. As mentioned previously, ECS have regular temporal



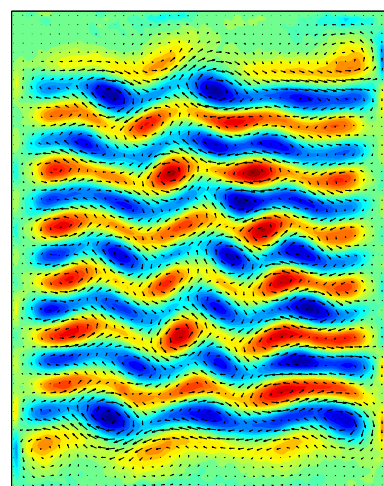
(a)



(b)



(c)



(d)

Figure 5.1: Four sequential weakly turbulent flow fields from the experiment, separated by  $\Delta t = 8.0$ .

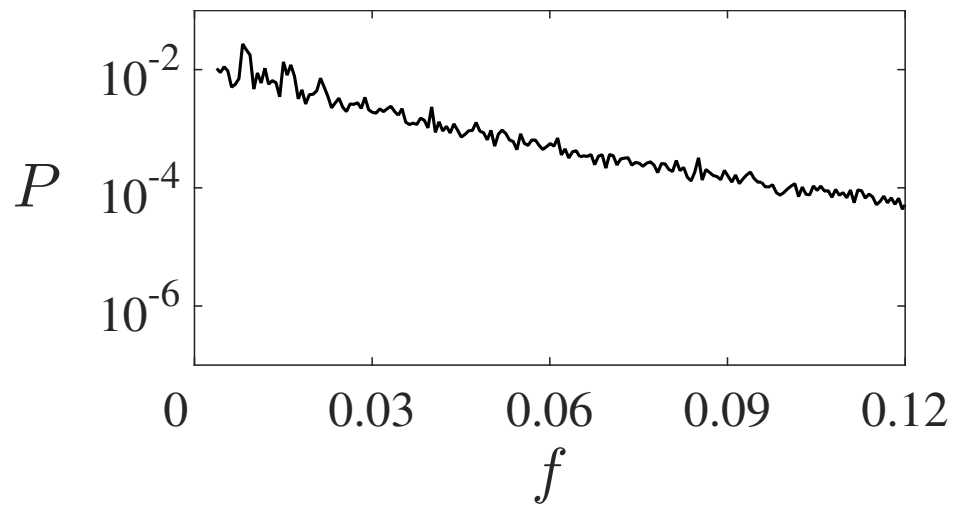


Figure 5.2: The spatially-averaged power spectrum for a long (1 hour) experimental time series.

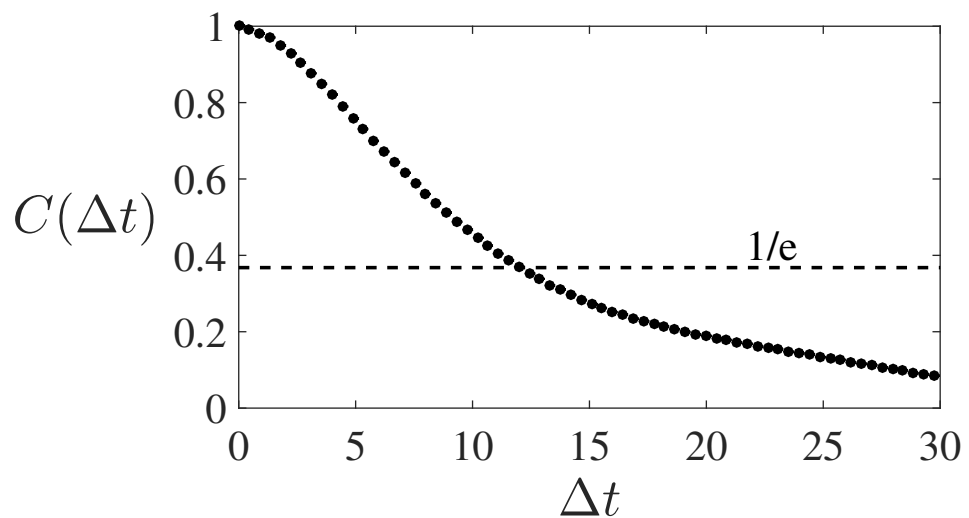


Figure 5.3: The experimental velocity field autocorrelation function  $C(\Delta t)$ .

dependence, meaning they correspond to unstable equilibria, periodic orbits, tori, etc. If one can identify an instant when a turbulent trajectory is traveling through the neighborhood of one of these solutions in state space, such an instant can be used as an initial condition for a specialized Newton solver, allowing the solution to be calculated (if the solver successfully converges). The analysis presented in this chapter is restricted to the simplest class of ECS, unstable equilibria. Before presenting the unstable equilibria which have been calculated, the criteria for determining when the turbulent trajectory is in the neighborhood of such a solution is first presented.

## 5.2 Calculating Unstable Equilibria

In general, an unstable equilibrium refers to a state in which a system does not change in time, but a minute perturbation can cause the system to evolve far away from that state. A simple example of an unstable equilibrium is the inverted position for a simple pendulum. For a turbulent trajectory evolving through state space, a sufficiently close pass to an unstable equilibrium requires that the rate of evolution decrease substantially. Analogously, a pendulum swinging with a large amplitude also slows down as it passes near its unstable equilibrium. The rate at which the turbulent trajectory evolves can be quantified using:

$$s(t) = \left\| \frac{\partial \mathbf{u}}{\partial t} \right\| \approx \frac{1}{\Delta t} \left\{ \iint [\mathbf{u}(t + \Delta t) - \mathbf{u}(t)]^2 dx dy \right\}^{1/2}, \quad (5.2)$$

where the integral is taken over the entire spatial domain and  $\Delta t$  defines the temporal frequency at which velocity fields are sampled in experiments. Hence, a criterion which can be used for determining when the turbulent trajectory *may* be close to an unstable equilibrium is to look for substantial decreases in  $s(t)$  [163].

The black curve in Figure 5.4 shows a short experimental time series of  $s(t)$  as a function of time (rescaled by the autocorrelation time  $\tau$ ). The red circles indicate the deepest minima which are at least one correlation time  $\tau$  apart; these instants are expected to be the most likely points in time for finding the turbulent trajectory

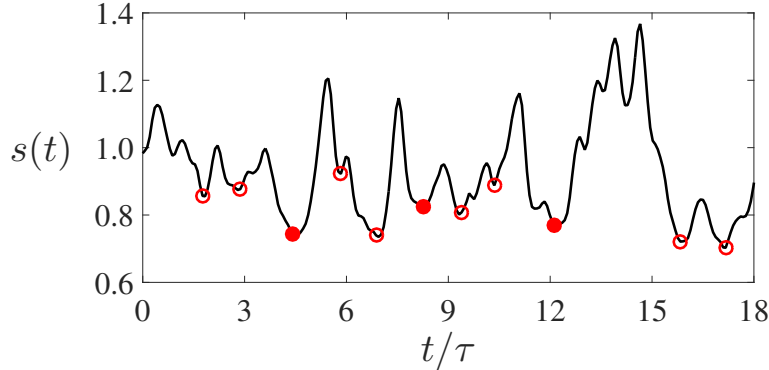


Figure 5.4: The rate of flow evolution,  $s(t) = \|\partial\mathbf{u}/\partial t\|$ , as a function of normalized time, in the experiment.

close to an unstable equilibrium. Moreover, if the turbulent trajectory is close to an unstable equilibrium, the spatial structure of that unstable equilibrium should be similar to the flow field from that instant on the trajectory when  $s(t)$  is minimal. Using experimental flow fields  $\mathbf{u}(t)$  from such instants as initial conditions, these corresponding unstable equilibria of equation (3.9) can be calculated using a matrix-free iterative Newton solver [164].

It is found that many of these initial conditions do indeed successfully converge to unstable equilibria. Successful convergences are indicated by the filled circles in Figure 5.4, while open circles correspond to initial conditions for which the solver failed to converge to an equilibrium. Overall, around 7% of the experimental initial conditions successfully converge to an unstable equilibrium. Note that the portion of the time series shown in Figure 5.4 has a particularly high number of convergences. Overall, a total of 13 distinct solutions have been found from experimental initial conditions.

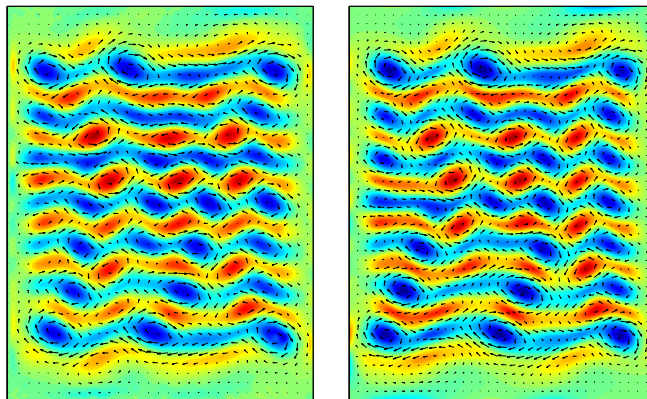
As an illustration, Figure 5.5 shows three examples of experimental flow fields used as initial conditions (left column) and the corresponding unstable equilibria computed (right column). The degree of similarity is striking, suggesting that turbulent trajectories pass quite close to these ECS. Using an identical methodology, 10 more distinct

unstable equilibrium solutions have been computed using initial guesses from a numerically generated turbulent trajectory. Of these, 4 were found to coincide with the ones computed from experimental initial conditions. The frequency with which the neighborhoods of the unstable equilibria are visited by the turbulent flow suggests that these ECS play an important dynamical role.

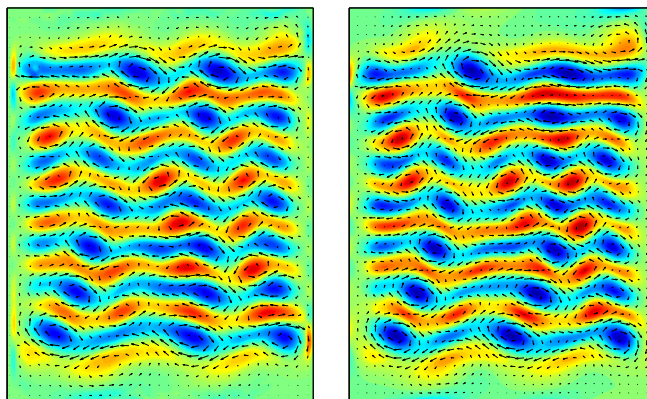
Before proceeding to the next section, there are two brief comments worth mentioning. Firstly, it is noted that minimal preprocessing is performed on the experimental flow fields before they are used as initial conditions for the solver. These experimental flow fields, which were obtained using PIV and are shown in Figure 5.5, are subject to small measurement inaccuracies (for example, a region in the flow may have a particle density which is too sparse for accurately calculating the cross-correlation). As a result of even very few incorrect velocity vectors, the experimental velocity field does not satisfy incompressibility. Additionally, the resolution of this velocity field is about 4 times less than that of the simulation (along each direction  $x$  and  $y$ ). Hence, experimental initial conditions are first interpolated onto the finer grid corresponding to the numerical simulations, and then projected onto a divergence-free subspace. This projection results in a change to the flow field of about 2% (calculated as the relative  $L_2$  norm). Secondly, it is important to realize that an instance of the solver failing to converge does *not* necessarily mean that the initial condition from the turbulent trajectory was not close to an unstable equilibrium. In some cases, it has been observed that for an initial condition which failed to converge, a convergence can be obtained by instead using a flow field from slightly earlier or slightly later in time as the initial condition.

### 5.3 Forecasting Weak Turbulence

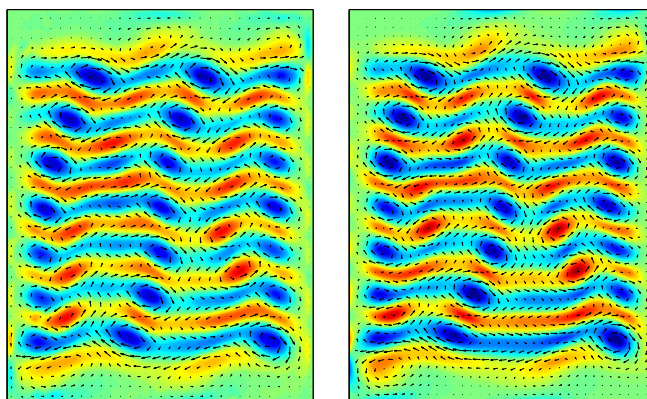
With several unstable equilibria in hand, it will now be demonstrated how such ECS can be used to forecast weak turbulence. As briefly mentioned in Section 2.1, the



(a)



(b)



(c)

Figure 5.5: Three experimental snapshots (left column) which correspond to local minima of  $s(t)$ ; when used as initial conditions for a Newton solver, each flow field converges to an unstable equilibrium (right column).

turbulent trajectory is expected to approach an unstable equilibrium following its stable manifold and recede following its unstable manifold. Hence, starting from an instant when the turbulent trajectory is known to be near an unstable equilibrium, the evolution can then be forecasted using the unstable manifold of that ECS. This section provides an example demonstrating that this is precisely what happens in the experiment.

Consider, for example, the unstable equilibrium shown in Figure 5.5 (c). This equilibrium has a 7-dimensional unstable manifold, with the associated eigenvalue spectrum consisting of one real and three complex conjugate pairs. These eigenvalues are:  $0.1492$ ,  $0.0147 \pm 0.1680i$ ,  $0.0045 \pm 0.1104i$ , and  $0.0009 \pm 0.4500i$ . As can be seen, the leading (real) eigenvalue is at least ten times greater than the real parts of the remaining six unstable eigenvalues. Furthermore, in this case the corresponding eigenfunctions in the physical space are spatially localized, as the respective vorticity fields shown in Figure 5.6 illustrate. Hence, as the turbulent trajectory recedes from this ECS, it is expected that it will be guided primarily by a one-dimensional (1D) invariant submanifold which is associated with the eigenfunction shown in Figure 5.6 (a). To compute this submanifold, a small perturbation is added to the unstable equilibrium in the direction of the leading eigenvector  $\mathbf{e}_1$  and then integrated forward in time.

For visualization purposes, the state space trajectories are projected onto a subspace spanned by the dominant eigenvector  $\mathbf{e}_1$  and vectors  $\mathbf{e}_2$  and  $\mathbf{e}_3$  constructed from the eigenvectors associated with a complex conjugate pair<sup>2</sup> such that  $\mathbf{e}_1$ ,  $\mathbf{e}_2$ , and  $\mathbf{e}_3$  form an orthogonal basis. The projection is shown in Figure 5.7 where the red sphere and the red curve denote the unstable equilibrium and its dominant unstable submanifold, respectively. Note that the trajectory which defines the submanifold is straight only close to the ECS and becomes curved further away due to the nonlinearity of the evolution equation (3.9). The blue and green curves correspond to experimental and

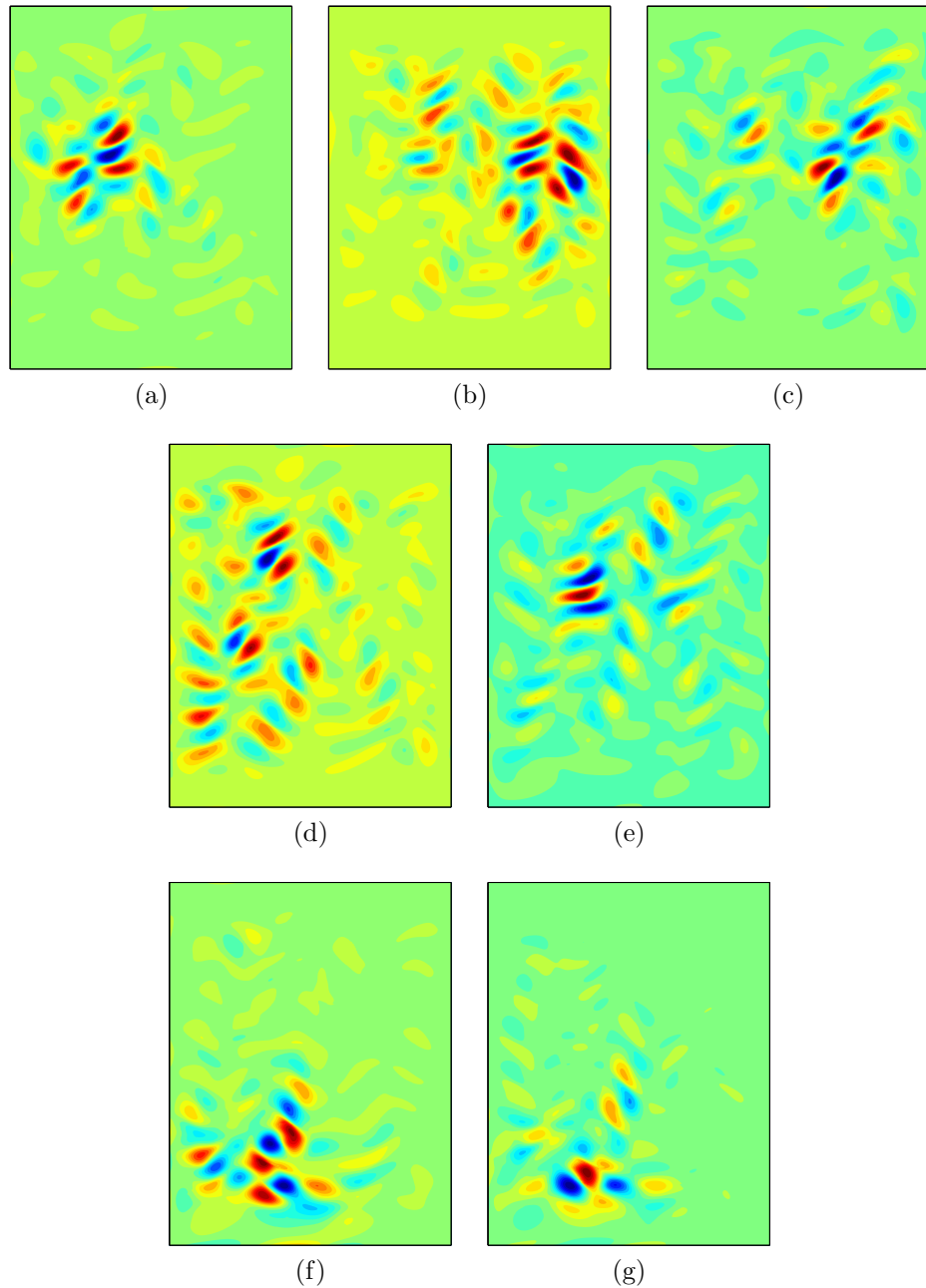


Figure 5.6: The vorticity field associated with the seven eigenfunctions of the unstable equilibrium used for forecasting. (a) The leading real eigenfunction, (b-c) the real and imaginary part of the first complex conjugate pair, (d-e) the real and imaginary part of the second complex conjugate pair, (f-g) the real and imaginary part of the third complex conjugate pair.

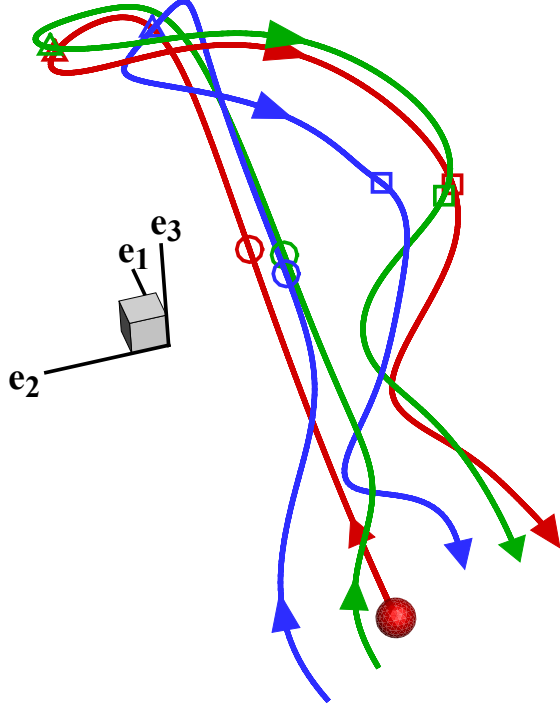


Figure 5.7: A projection showing an unstable equilibrium (red sphere) with its dominant unstable submanifold (red curve). Both the experimental (blue curve) and numerical (green curve) turbulent trajectories follow this submanifold as they depart from the neighborhood of this unstable equilibrium.

numerical turbulent trajectories receding from the ECS, respectively. They follow the submanifold remarkably well even far away from the ECS, with the length of the experimental curve corresponding to a total of  $3.4\tau$ .

To illustrate the degree of similarity between the turbulent trajectories and the dominant submanifold in the physical space, snapshots of the flow fields along these

---

<sup>2</sup>The projection shown in Figure 5.7 corresponds to a subspace spanned by the leading eigenfunction (Figure 5.6 (a)) and the eigenfunctions associated with the complex conjugate pair in Figure 5.6 (f) and 5.6 (g) which have eigenvalues of  $0.0009 \pm 0.4500i$ . The choice of this specific complex conjugate pair is motivated by the shape of the submanifold in the full state space. As Figure 5.7 illustrates, the leading submanifold exhibits significant curvature due to the nonlinearity of the evolution equations. As a result, disturbances initially have no components in the direction of any of the three complex conjugate pairs, but eventually acquire nonvanishing components along each of these six directions. The components along the third complex conjugate pair happen to be the largest by far. As a result, the eigenfunctions associated with that pair, along with the leading eigenfunction, capture the evolution of the flow with reasonably good accuracy during the entire time interval represented in Figure 5.7. Note that for the projection, these three directions have been orthogonalized using the Gram-Schmidt process.

trajectories are provided in Figure 5.8. The corresponding sequential time instants for each trajectory are indicated in Figure 5.7 by an open circle, triangle, and square. Note that these three instants are separated by about  $0.7\tau$ . The flow fields corresponding to all three trajectories are very similar, which validates the conjecture that dominant manifolds guide neighboring turbulent trajectories. The first set of flow fields (Figure 5.8 (a)) are characterized by the appearance of new vortices near the left-center. The localization of this emerging feature corresponds to evolution dominantly along the leading eigenvector (whose eigenfunction is shown in Figure 5.6 (a)). As the flows evolve, a new column of vortices emerge, first in the top half of the domain, as shown in Figure 5.8 (b). This new column of vortices then propagates downward, throughout the rest of the domain, as shown in Figure 5.8 (c).

## 5.4 Discussion

The results presented in this chapter provide the first direct and unambiguous evidence in support of the dynamical role played by exact coherent structures in a weakly turbulent flow. The particular ECS studied here (unstable equilibria) have been calculated by directly plugging experimental initial conditions into a Newton solver; these initial conditions were chosen based on the dynamical criterion that  $s(t)$  be a local minimum. Furthermore, as shown in Figure 5.5, these experimental initial conditions closely resemble the unstable equilibria. By constructing the 1D dominant unstable submanifold of one such solution, the flow observed in the laboratory can be forecasted for over  $3\tau$ , as depicted in Figures 5.7 and 5.8. This is a demonstration of forecasting in that whenever the experimental turbulent trajectory is in the vicinity of this solution, the evolution for the next few  $\tau$  is known, provided it passes close enough. This result is the first laboratory demonstration of deterministic forecasting of weak turbulence using ECS. Further calculations are needed to construct the network of dynamical connections (see, for example, the cartoon provided in Figure 2.1

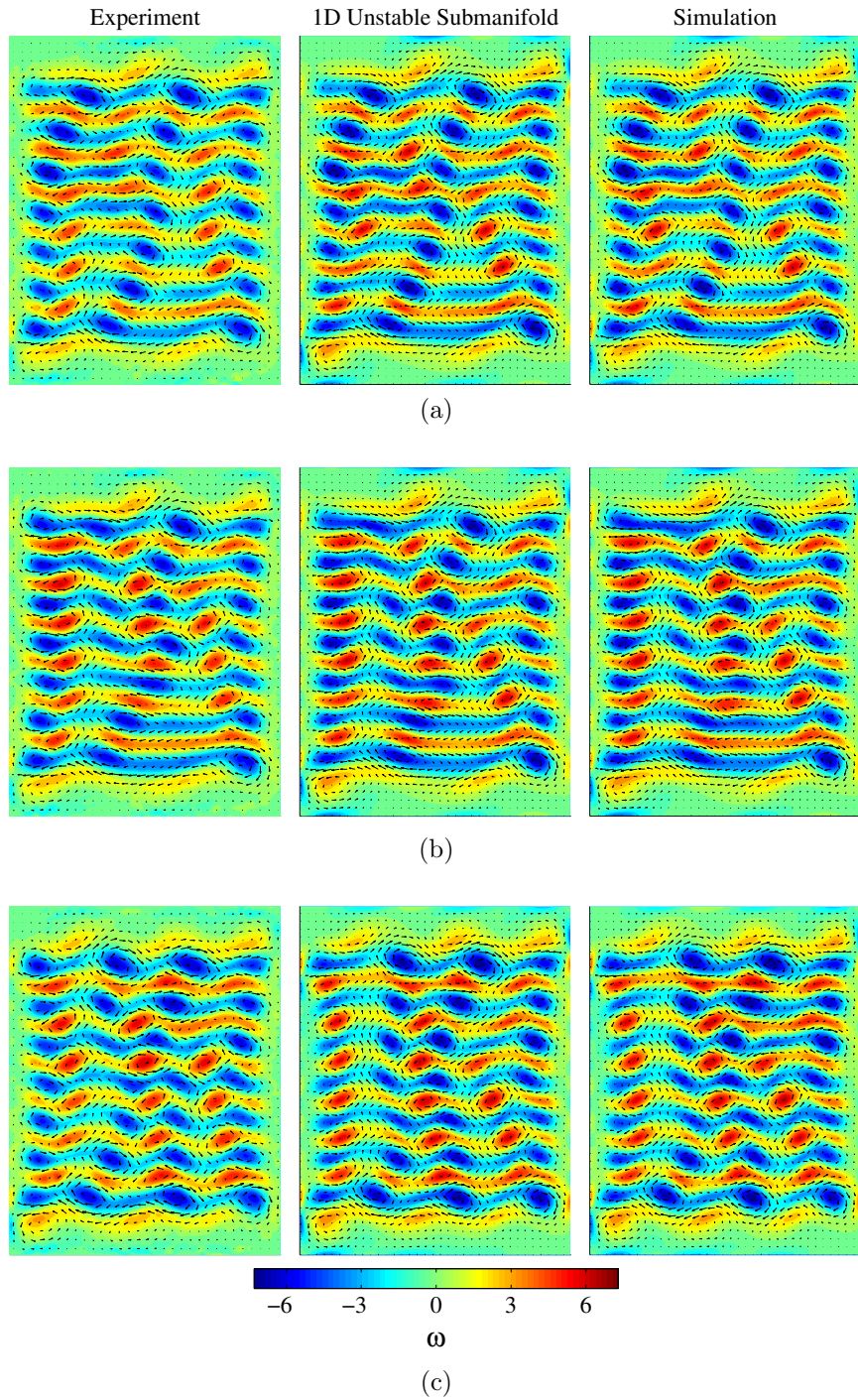


Figure 5.8: Representative flow fields from the experimental turbulent trajectory (left column), 1D dominant submanifold (middle column), and the numerical turbulent trajectory (right column) at three different instances of time separated by about  $0.7\tau$ . Each instance is indicated in Figure 5.7 by (a) a circle, (b) a triangle, and (c) a square.

(b)) which would allow forecasting over longer periods of time.

# CHAPTER VI

## APPLICATION OF PERSISTENT HOMOLOGY

In this chapter, persistent homology is used as a dimensionality reduction tool to study sets of flow fields from the doubly-periodic simulation (DPS) of the Kolmogorov-like flow. The DPS, which has two discrete symmetries as well as a continuous translational symmetry (described below), is the subject of this study for the purpose of highlighting how persistent homology handles these symmetries. In Section 6.1, the data from the DPS is introduced which will be analyzed throughout this chapter. In Section 6.2, persistence diagrams are generated for flow fields from the DPS and their features are highlighted. Section 6.3 introduces how metrics can be applied to probe the dynamics of a time series of flow fields. Finally, in Section 6.4, the concept of a point cloud is introduced and used to compare flow fields and identify periodic dynamics.

### 6.1 *The Dynamical Regimes Studied*

As mentioned briefly at the end of Chapter 3, flow fields from the DPS are generated by using the vorticity-stream function formulation [165]. By taking the curl of equation (3.9), one obtains:

$$\frac{\partial \omega}{\partial t} + \beta \mathbf{u} \cdot \nabla \omega = \nu \nabla^2 \omega - \alpha \omega + A \kappa \cos(\kappa y). \quad (6.1)$$

where  $\omega$  is the  $z$ -component of the scalar vorticity field  $\omega = (\nabla \times \mathbf{u}) \cdot \hat{\mathbf{z}}$ , and the forcing is sinusoidal with amplitude  $A$ . Equation (6.1) is solved numerically by using a semi-discrete spectral method [157] assuming periodic boundary conditions in both the  $x$ - and  $y$ -directions, i.e.,  $\omega(x, y) = \omega(x + L_x, y) = \omega(x, y + L_y)$ , where  $L_x = 6.7$  and  $L_y = 8.0$  are the dimensions of the domain in the  $x$ - and  $y$ -directions, respectively.

It is important to note that equation (6.1), with periodic boundary conditions, is equivariant under any combination of three distinct coordinate transformations: (i) a translation along  $x$ :  $\mathcal{T}_{\delta x}(x, y) = (x + \delta x, y)$ ,  $\delta x \in [0, L_x]$ , (ii) a rotation by  $\pi$ :  $\mathcal{R}(x, y) = (-x, -y)$ , and (iii) a reflection and a shift:  $\mathcal{S}(x, y) = (-x, y + 1)$ . Because of these symmetries, each particular solution to equation (6.1) generates a “group orbit” of solutions which are dynamically equivalent. Physically, equivariance under continuous translation  $\mathcal{T}_{\delta x}$  means that in addition to equilibrium (EQ) and periodic orbit (PO) solutions, there are also relative equilibrium (REQ) and relative periodic orbit (RPO) solutions. The REQ and RPO solutions only differ from EQ and PO solutions in that they also translate along the continuous symmetry as they evolve.

For  $Re = 23.55$ , the flow is characterized by a steady RPO; Figure 6.1 (a) shows a projection, plotted using the three dominant Fourier modes of this RPO. The RPO has a period 17.9 and a slow drift speed of  $2.07 \times 10^{-4}$ . The tunnel-like structure is a result of the periodic motion superposed over the slow drift along the  $x$ -direction. At higher driving ( $Re = 24.90$ ), the flow becomes weakly turbulent, as can be seen from the Fourier projection in Figure 6.1 (b). The weakly turbulent dynamics in this regime are of great interest as the flow explores a region of the state space which contains weakly unstable EQ, PO, REQ, and RPO solutions. The turbulent trajectory depicted in Figure 6.1 (b) passes close to unstable EQ and REQ solutions which have been calculated and are indicated by the red circles.

## 6.2 Generating and Interpreting PDs

To analyze the dynamics from the DPS as described in the previous section, persistent homology is used as a nonlinear dimensionality reduction method. In this method, the structure of the sublevel sets of the scalar vorticity field  $\omega: D \rightarrow \mathbb{R}$  is analyzed, where  $D$  is a topological space. The sublevel sets are defined as:

$$\mathbb{C}(f, \theta) = \{x \in D \mid f(x) \leq \theta\}, \quad (6.2)$$

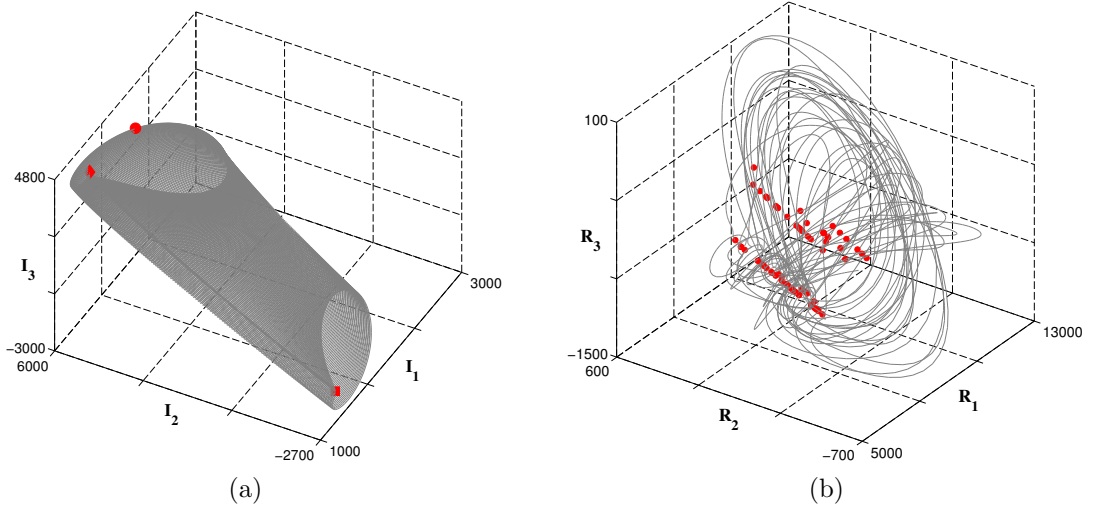


Figure 6.1: (a) Three-dimensional projections of a stable RPO at  $Re = 23.55$  from the DPS using the imaginary part of the three dominant Fourier modes,  $I_1$ ,  $I_2$ , and  $I_3$ . The gray line indicates the evolution of a RPO; three snapshots sampled from that orbit are indicated by a red diamond, a red circle, and a red square, which are analyzed below. (b) Three-dimensional projections of a turbulent trajectory, at  $Re = 24.90$ , using the real parts of the three dominant Fourier modes,  $R_1$ ,  $R_2$ , and  $R_3$ . The gray line indicates the chaotic evolution of the flow, which is influenced by the presence of unstable equilibria, indicated by red circles, which are also analyzed below.

where  $\theta \in \mathbb{R}$  can be thought of as the sublevel ‘‘threshold.’’ As  $\theta$  is varied, the number of components, holes, and cavities in  $C(f, \theta)$  change. Information regarding the *births*, *deaths*, and *life span* of these features are encoded into three separate PDs, denoted  $\text{PD}_0$ ,  $\text{PD}_1$ , and  $\text{PD}_2$ , which are associated with components, holes, and cavities, respectively. An introduction to these concepts is available in Sections 2.2.1 and 2.2.2. Note that only  $\text{PD}_0$  and  $\text{PD}_1$  are associated with a 2D domain, but because of the periodic boundary conditions,  $D$  is a torus enclosing a three-dimensional cavity, which requires that  $\text{PD}_2$  also be considered. Points with longer life spans in the PDs (i.e., points far from the diagonal) are associated with geometric features that exist through larger variations of  $\theta$ , and are therefore considered dominant features. It is important to point out that separate features might be represented by persistence points with the same coordinates. Therefore, the multiplicity of each persistence

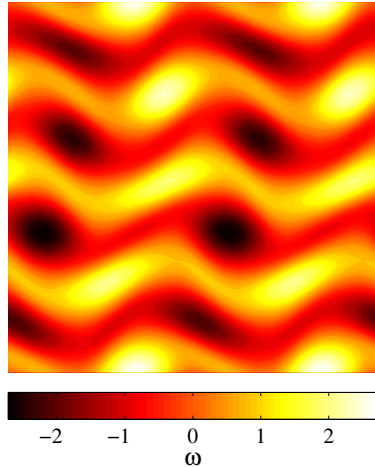


Figure 6.2: A snapshot of the  $z$ -component of the vorticity field  $\omega$  for the Kolmogorov-like flow DPS. This flow field is sampled from the stable relative periodic orbit found at  $Re = 23.55$ .

point corresponds to the number of features represented by the persistence point. Moreover, every PD contains infinitely many points along the diagonal  $\theta_b = \theta_d$ , which is important to keep in mind when metrics are applied to PDs.

The numerical data for the vorticity fields is discretized in double precision on a rectangular grid of dimensions  $128 \times 128$ . Because of the discretization, the vorticity field should be thought of as a piecewise-constant function defined on a rectangular grid. Furthermore, this discretization allows for a finite set  $\Theta$  to be defined, corresponding to the values of  $\omega$  which are attained for a given flow field. The Perseus software [166] is used to compute the corresponding  $\text{PD}_k(\omega)$  for  $k = 0, 1, 2$  using only the values  $\theta \in \Theta$ .

To begin the persistent homology analysis, consider the example flow field shown in Figure 6.2. Four sublevel sets for this vorticity field are shown in Figure 6.3 (a-d), which help illustrate the features of the associated diagrams  $\text{PD}_0(\omega)$  and  $\text{PD}_1(\omega)$

shown in Figure 6.3 (e-f), respectively. Recall that  $\text{PD}_0(\omega)$  is associated with connected components. The minimum value of the vorticity field is  $-2.7206$ , and therefore,  $C(\omega, \theta) = \emptyset$  for all  $\theta < -2.7206$ . At  $\theta = -2.7206$ , two components simultaneously appear, indicated by the two persistence points with birth value  $\theta_b = -2.7206$ . These components grow as  $\theta$  increases, and eventually merge at  $\theta_d = -0.697$ . By convention, when a death occurs it is paired with the highest adjacent birth and a point  $(\theta_b, \theta_d)$  is plotted in  $\text{PD}_0$ . Since both adjacent births occur at  $\theta = -2.7206$ , the choice is arbitrary, and a single persistence point is plotted at  $(-2.7206, -0.697)$ . At higher  $\theta$ , there is no death which can be matched with the second birth which occurred at  $\theta = -2.7206$ ; hence, it persists to  $\theta_d = \infty$ , and a point is plotted at  $(-2.7206, \infty)$ . Note that a single point is plotted with  $\theta_d = \infty$ , which is consistent with the homology of a torus, for which Betti number  $\beta_0 = 1$ .

Figure 6.3 (a) indicates the subset of  $D$  corresponding to  $C(\omega, -1.5)$ . Since  $D$  is a torus,  $C(\omega, -1.5)$  consists of eight distinct connected components instead of nine. The existence of these eight connected components can also be extracted from  $\text{PD}_0(\omega)$ , shown in Figure 6.3 (e). These connected components correspond to the connected regions with birth value  $\theta_b \leq -1.5$  and death value  $\theta_d > -1.5$ , which clearly form the 8 dominant points in Figure 6.3 (e). Figure 6.3 (b) indicates that  $C(\omega, 0)$  consists of four connected horizontal bands, which agrees with the number of persistence points in the rectangular region defined by  $\theta_b \leq 0$  and  $\theta_d > 0$ . Each stripe is created as two distinct components present in Figure 6.3 (a) grow and merge horizontally, causing one component to die each time. The deaths of these components are captured by the points for which  $\theta_b \leq -1.5$  and  $\theta_d \leq 0$ .

Now, considering Figure 6.3 (c), it is clear that three horizontal stripes merge together before  $\theta = 0.75$ , as indicated by the two points inside the rectangle defined by  $\theta_b \leq 0$  and  $0 \leq \theta_d \leq 0.75$ . The two remaining connected components merge together soon thereafter, and for all greater threshold values, there is only one connected

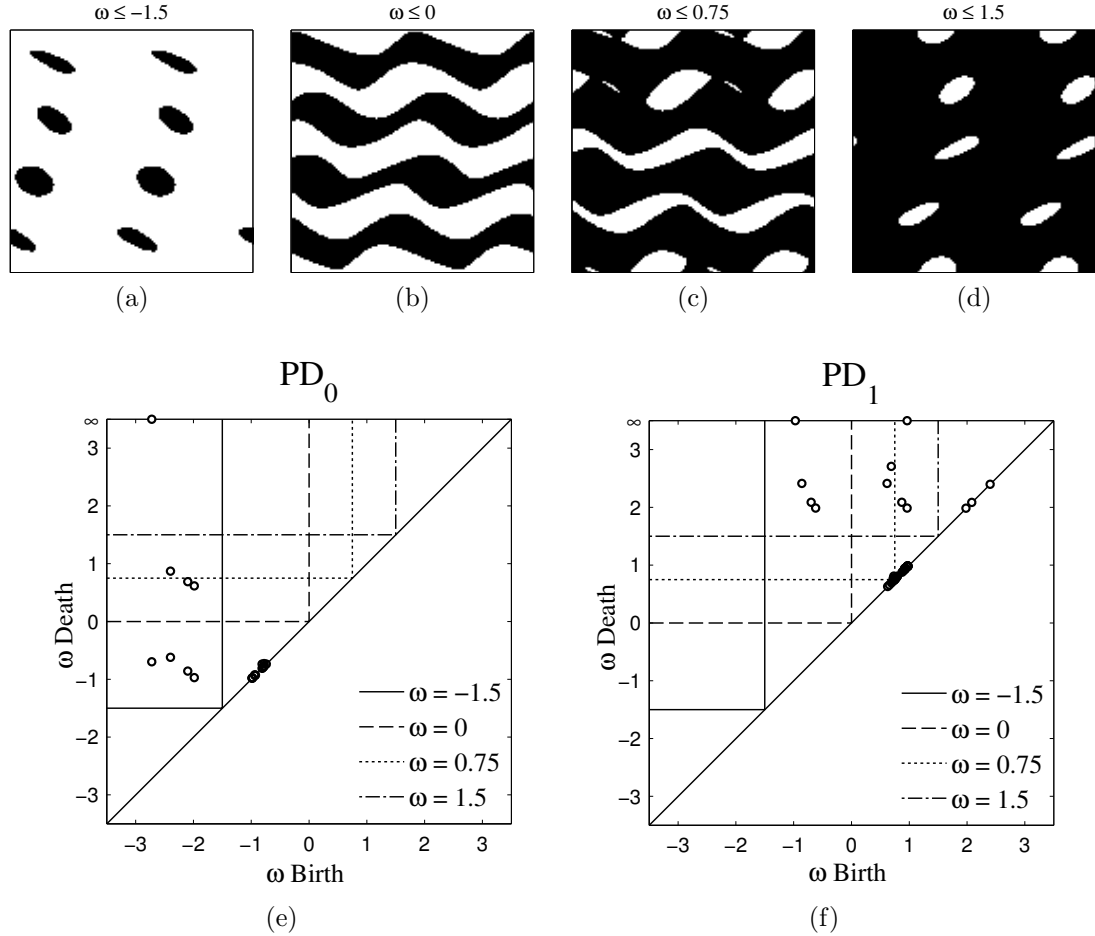


Figure 6.3: (a-d) Sublevel sets  $C(\omega, \theta) = \{x \in D : \omega(x) \leq \theta\}$  of the vorticity field shown in Figure 6.2, for different values of  $\theta$ , depicted in black. (e)  $\text{PD}_0(\omega)$  and (f)  $\text{PD}_1(\omega)$  persistence diagrams of the vorticity field indicate the values of  $\theta$  at which the connected components and holes appear and disappear (merge together). Every point  $(\theta_b, \theta_d)$  in the  $\text{PD}_0(\omega)$  ( $\text{PD}_1(\omega)$ ) persistence diagram corresponds to a connected component (hole) that is present in every set  $C(\omega, \theta)$ , for  $\theta_b \leq \theta < \theta_d$ . A connected component disappears by merging with a previously existing component and a hole disappears when it is filled in.

component. Finally, to conclude the discussion of  $\text{PD}_0(\omega)$ , the persistence points close to the diagonal are discussed. These points have very short life spans, which suggests that they may arise due to numerical artifacts. The points are generated from very small spatial fluctuations of the vorticity field as the groups of two connected components (Figure 6.3 (a)) merge to form the thin horizontal bands (Figure 6.3 (b)).

Now recall that the diagram  $\text{PD}_1(\omega)$  is associated with holes (or loops) in  $C(\omega, \theta)$ . A hole corresponds to a region of white completely surrounded by black. Keeping in mind that the domain is doubly-periodic, then Figure 6.3 (d), for example, has 8 holes. From  $\text{PD}_1(\omega)$ , it is clear that the first hole appears at threshold  $\theta = -0.963$ . It corresponds to one of the four horizontal white bands shown in Figure 6.3 (b). Each horizontal white band generates a single independent hole, corroborated by the existence of four persistence points in the rectangle defined by  $-1.5 \leq \theta_b \leq 0$  and  $\theta_d > 1.5$  of  $\text{PD}_1(\omega)$ .

It is noted that the full torus has two holes captured by homology (i.e., recall that  $\beta_1 = 2$  in Figure 2.3). This is expressed in  $\text{PD}_1(\omega)$  by the two persistence points with  $\theta_d = \infty$ . Observe that the first hole that appears at  $\theta = -0.963$  is associated with the toroidal hole (the “center of the donut”), thus it cannot be killed and is hence captured by the persistence point  $(-0.963, \infty)$ . The other three holes present at  $\theta = 0$  are also associated with the toroidal direction and thus must die. In fact, they do so by  $\theta = 2.5$ . Note that the birth values  $\theta_b$  of these persistence points are close to the death values  $\theta_d$  of the persistence points in the rectangle defined by  $\theta_b > -1.5$  and  $-1.5 \leq \theta_d \leq 0$  of  $\text{PD}_0(\omega)$ . This implies that shortly after the components merge, they form horizontal bands across the entire domain.

New holes are also created as the black bands start merging. If two horizontal bands are connected by  $n$  links, then the number of holes generated by this object (two bands plus the links) is  $(n + 1)$ . Thus, the first additional hole appears when a second link is created. In the example flow field, this happens near the threshold

0.75.

In Figure 6.3 (c), there are four distinct links between the two horizontal bands at the top of the figure. The small holes visible in Figure 6.3 (c) are filled in almost immediately, and the four links merge into two distinct links. The points in  $\text{PD}_1(\omega)$  that are close to the diagonal capture this behavior. The other two links are present for a wider range of thresholds, and the hole they generate is represented by one of the persistence points in  $\text{PD}_1(\omega)$  with birth coordinate slightly smaller than 0.75. The horizontal band at the top and the horizontal band at the bottom are linked in a similar fashion. This explains the presence of another point with birth coordinate slightly smaller than 0.75.

At  $\theta = 0.932$ , a connection from the top to the bottom boundary is created. This hole is homologically equivalent to the second of the two independent holes of the torus (i.e., the hole associated with the poloidal direction of the torus), and hence is identified by the persistence point  $(0.932, \infty)$ . As the threshold passes the value 1.988, the remaining holes shown in Figure 6.3 (d) start filling in and dying. Since the maximum value of  $\omega$  is 2.7092, the sublevel set is the whole torus for any threshold above this, i.e.,  $C(\omega, \theta) = D$  for all  $\theta \geq 2.7092$ . In this case, there are no more punctures; hence, for  $\theta_d > 2.7092$  there are only two persistence points.

Finally, the  $\text{PD}_2(\omega)$  persistence diagram is considered, but not shown for brevity. This diagram contains a single persistence point at  $(\theta_b, \infty) = (2.7092, \infty)$ . The birth coordinate,  $\theta_b$ , corresponds to the minimum value of  $\theta$  for which  $C(\omega, \theta) = D$ , and since  $C(\omega, \theta) = D$  for all  $\theta \geq \theta_b$ , this point never dies. In other words, there is one cavity associated with the torus which does not appear until  $\theta$  has reached the maximum value of  $\omega$ , 2.7092. When  $\theta$  reaches 2.7092, the remaining portion of the torus appears and encloses a cavity. As  $\theta$  continues to increase, no further changes occur, so the cavity never dies; hence,  $\text{PD}_2(\omega)$  contains a single point at  $(2.7092, \infty)$ .

### 6.3 Applying Metrics to the Space of PDs

As illustrated in the previous section, a PD codifies, in a reasonably compact form, considerable information about the geometry of a scalar function. As suggested by the examples, PDs provide a reduced description of the state of the dynamical system of interest at any given point in time. Therefore, to analyze the dynamics, we need to be able to compare one collection of diagrams  $\text{PD}$  (corresponding to a snapshot of the flow pattern at an instant of time) to another collection of diagrams  $\text{PD}'$  (from another flow snapshot). The reader is reminded that the calculations of the bottleneck and Wasserstein distances were introduced in Section 2.2.2. Here, a more general equation for these distances is provided which accounts for  $k$  PDs. The *bottleneck distance* is defined between  $\text{PD}$  and  $\text{PD}'$  as:

$$d_B(\text{PD}, \text{PD}') = \max_k \inf_{\gamma: \text{PD}_k \rightarrow \text{PD}'_k} \sup_{p \in \text{PD}_k} \|p - \gamma(p)\|_\infty, \quad (6.3)$$

where  $\|(a_0, b_0) - (a_1, b_1)\|_\infty := \max \{|a_0 - a_1|, |b_0 - b_1|\}$  and  $\gamma$  ranges over all bijections between persistence points. Similarly, the *degree- $q$  Wasserstein distance* is defined as:

$$d_{W^q}(\text{PD}, \text{PD}') = \left[ \sum_k \inf_{\gamma: \text{PD}_k \rightarrow \text{PD}'_k} \sum_{p \in \text{PD}_k} \|p - \gamma(p)\|_\infty^q \right]^{1/q}. \quad (6.4)$$

It is highlighted that the bottleneck distance  $d_B$  measures only the single largest difference between the persistence diagrams and ignores the rest. The Wasserstein distance  $d_{W^q}$ , on the other hand, includes all differences between the diagrams. Thus, it is always true that:

$$d_B \leq d_{W^q}. \quad (6.5)$$

The sensitivity of the Wasserstein metric to small differences (possibly due to noise) can be modulated by the choice of the value of  $q$ , i.e., if  $q > r$  then one expects  $d_{W^q}$  to be less sensitive to small changes than  $d_{W^r}$ . It is emphasized that the application of the Wasserstein or bottleneck metrics is a Lipschitz-continuous function [167]. This

implies that, assuming bounded errors from numerical discretization in the simulation (or even bounded noise in experimental data), the associated errors from the distance calculations are also bounded.

In Section 6.3.1, these metrics (bottleneck and Wasserstein with  $q = 1, 2$ ) are applied to compare example flow fields with an emphasis on symmetry reduction. Then, in Section 6.3.2, two flow fields are compared and the number of different small-scale and large-scale features are estimated. Finally, Section 6.3.3 includes a discussion of how metrics can be used to quantify the rate of evolution from a time series of flow fields.

### 6.3.1 Comparing Flow Fields

The most obvious use of the bottleneck and Wasserstein metrics is to distinguish patterns. As an example, patterns along the RPO from the Kolmogorov-like flow are considered. As mentioned earlier, this particular trajectory arises from a periodic orbit with a slow drift along the continuous symmetry. In particular, three sample points are indicated in Figure 6.1 (a): two that appear to differ by the continuous symmetry, and a third that lies on the “opposite” side of the periodic orbit. Plots of the associated vorticity fields at these points (see Figure 6.4) agree with this characterization of the time points. The intent is to identify this information through the associated diagrams  $\text{PD}^a$ ,  $\text{PD}^b$ , and  $\text{PD}^c$ , shown in Figure 6.5. Indeed, the plots of  $\text{PD}_k^a$  and  $\text{PD}_k^b$  are difficult to distinguish, but  $\text{PD}_k^c$  is clearly distinct. This illustrates that symmetry reduction of the continuous symmetry is automatically performed in the process of generating a PD.

To quantify the difference between these flow fields, the distances between the PDs using  $d_B$ ,  $d_{W^2}$ , and  $d_{W^1}$  are utilized. These values are recorded in Table 6.1. Not surprisingly, the distances between  $\text{PD}^a$  and  $\text{PD}^b$  are much smaller than the distances between  $\text{PD}^a$  and  $\text{PD}^c$ . Using these distances, as opposed to the detailed information

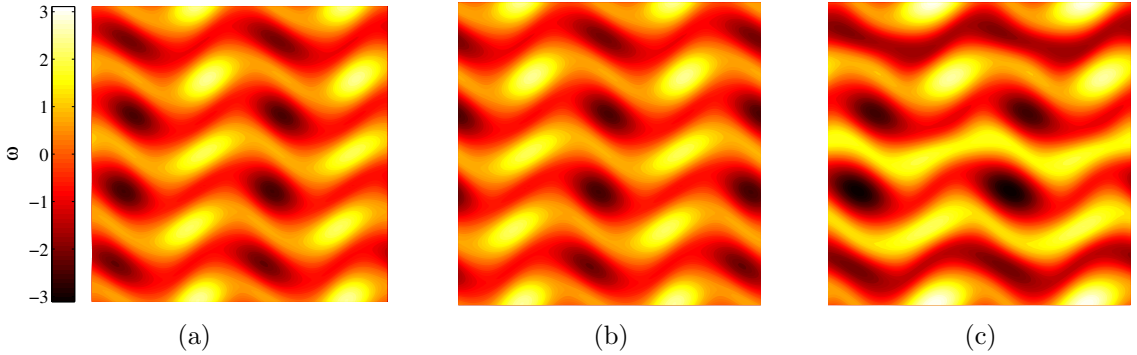


Figure 6.4: Three snapshots of the vorticity fields  $\omega$  from the stable RPO of the Kolmogorov-like flow found at  $Re = 23.55$ . The vorticity fields correspond to the (a) diamond, (b) square, and (c) circle in Figure 6.1 (a). The persistence diagrams for these three snapshots are generated and compared in Figure 6.5. Differences between the persistence diagrams are qualitatively measured by the distances shown in Table 6.1.

Table 6.1: Distances between selected persistence diagrams (rounded to 3 decimal places) in Figure 6.5, corresponding to the vorticity fields shown in Figure 6.4.

	$d_B$	$d_{W^2}$	$d_{W^1}$
$(\text{PD}^a, \text{PD}^b)$	0.01	0.049	0.497
$(\text{PD}^a, \text{PD}^c)$	0.864	2.648	12.35
ratio $\frac{(\text{PD}^a, \text{PD}^c)}{(\text{PD}^a, \text{PD}^b)}$	86.4	54.05	24.85

in the PDs, one can obtain a rough estimate of what number of small-scale and large-scale features have changed between Figure 6.4 (a) and Figure 6.4 (c). This is demonstrated in the next section.

### 6.3.2 Estimating the Number of Changes in Small-Scale and Large-Scale Features

Recall that the bottleneck distance measures only the single largest difference between the persistence diagrams and ignores the rest. Since the patterns shown in Figure 6.4 (a) and (b) differ by a symmetry transformation,  $d_B(\text{PD}^a, \text{PD}^b)$  can be interpreted as a rough estimate of the distance associated with a change in a small-scale feature (i.e., numerical error arising from discretization). The patterns shown in Figure 6.4 (a) and (c), however, are *not* symmetry-related and thus have large-scale changes which are comparable to  $d_B(\text{PD}^a, \text{PD}^c)$ , as well as small-scale changes. The

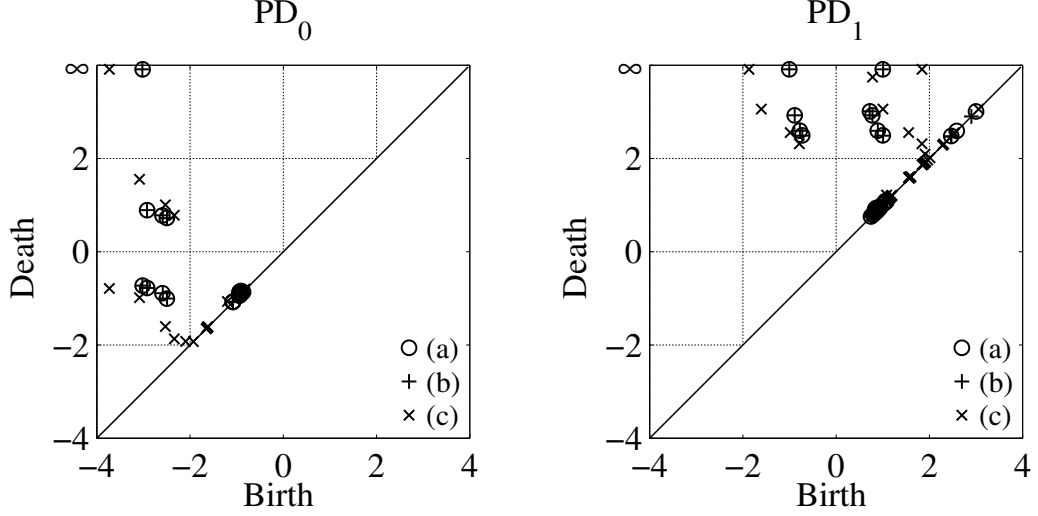


Figure 6.5:  $\text{PD}_0$  persistence diagrams  $\text{PD}^a$ ,  $\text{PD}^b$ , and  $\text{PD}^c$  for the vorticity fields shown in Figure 6.4. The points in  $\text{PD}^a$  and  $\text{PD}^b$  are almost identical because the corresponding vorticity fields are related by a symmetry operation. The points in  $\text{PD}^c$  are more spread out and do not resemble the points in  $\text{PD}^a$  as well. The same is true for the  $\text{PD}_1$  persistence diagrams. Consequently,  $d_*(\text{PD}^a, \text{PD}^b) < d_*(\text{PD}^a, \text{PD}^c)$ , for  $* \in \{B, W^2, W^1\}$ , as indicated by Table 6.1.

ratio  $d_B(\text{PD}^a, \text{PD}^c)/d_B(\text{PD}^a, \text{PD}^b)$  is 86.4, which supports the claim that there is a significant distinction between the changing small-scale features (due to numerical error) and the changing large-scale features (due to significant geometric changes).

In this analysis, it is assumed that there are only two different scales at which the geometric features evolve: one scale corresponding to the large-scale features (of order  $d_B(\text{PD}^a, \text{PD}^c)$ ) and the other representing the noise fluctuations (of order  $d_B(\text{PD}^a, \text{PD}^b)$ ). The distances  $d_{W^1}(\text{PD}^a, \text{PD}^c)$  and  $d_{W^2}(\text{PD}^a, \text{PD}^c)$  can then be approximated as follows:

$$d_{W^1}(\text{PD}^a, \text{PD}^c) \approx n \cdot d_B(\text{PD}^a, \text{PD}^c) + k \cdot d_B(\text{PD}^a, \text{PD}^b), \quad (6.6)$$

$$d_{W^2}(\text{PD}^a, \text{PD}^c) \approx \sqrt{n(d_B(\text{PD}^a, \text{PD}^c))^2 + k(d_B(\text{PD}^a, \text{PD}^b))^2}, \quad (6.7)$$

where  $n$  and  $k$  are the number of large-scale and small-scale features that change, respectively. Now, since  $d_B(\text{PD}^a, \text{PD}^b) \ll d_B(\text{PD}^a, \text{PD}^c)$  (as indicated in Table 6.1),  $(d_B(\text{PD}^a, \text{PD}^b))^2$  will be negligible compared to  $(d_B(\text{PD}^a, \text{PD}^c))^2$ . Hence, equation

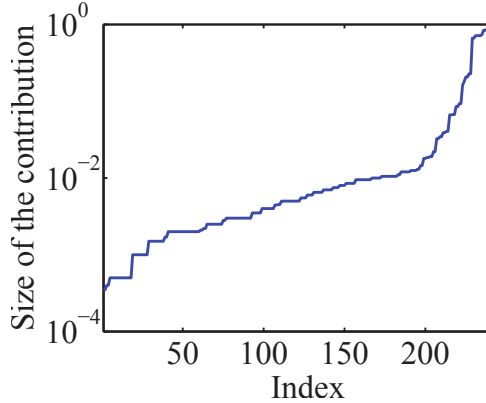


Figure 6.6: Contributions to the  $d_{W^1}(\text{PD}^a, \text{PD}^c)$  distance.

(6.7) can be rewritten as:

$$d_{W^2}(\text{PD}^a, \text{PD}^c) \approx \sqrt{n(d_B(\text{PD}^a, \text{PD}^c))^2}. \quad (6.8)$$

By solving equations (6.6) and (6.8), one obtains  $n \approx 9$  (large-scale changing features) and  $k \approx 400$  (small-scale changing features).

These results are confirmed as good estimates by plotting the sorted sizes of the individual contributions to  $d_{W^1}(\text{PD}^a, \text{PD}^c)$ , as shown in Figure 6.6. From this plot, it is clear that there are approximately 200 changing features of order equal to or smaller than  $d_B(\text{PD}^a, \text{PD}^b)$  and 11 dominant changes of order  $d_B(\text{PD}^a, \text{PD}^c)$ . Approximately 28 changes occurring on intermediate scales can be identified, and their sizes are at least an order of magnitude smaller than  $d_B(\text{PD}^a, \text{PD}^c)$ . In fact, most of them are not much larger than  $d_B(\text{PD}^a, \text{PD}^b)$ . Hence, the assumption that the changes can be roughly divided into two classes of different order seems reasonable. The fact that the division is not absolutely sharp leads to the discrepancy between the estimates and the observations from Figure 6.6, but the prediction for the number of changing large-scale features is very close. This section demonstrates that by comparing measurements made using different metrics, one can gain insight into the differences in geometry between two flow fields.

### 6.3.3 Measuring the Rate of Evolution

In Section 2.2.2, the concept of a persistent homology state space  $\text{Per}$  was introduced. In this section, it is demonstrated how viewing a time series in  $\text{Per}$  can provide insight into the underlying dynamics. Let  $f_i$  denote the scalar field of the system at time  $t_i$ . If  $\Delta t = t_{i+1} - t_i$  is small and the evolution of the system is continuous, then because  $d_*$  (for  $*$   $\in \{B, W^2, W^1\}$ ) is a metric,

$$s_*(t_i) = \frac{d_*(\text{PD}(f_i), \text{PD}(f_{i+1}))}{\Delta t} \quad (6.9)$$

can be interpreted as an average speed in the space of PDs over the time interval  $[t_i, t_{i+1}]$ . Note that this equation is analogous to equation (5.2), but calculated using a different metric in a different space. The value of  $s_*$  depends on the particular choice of metric. For example,  $s_{d_B}$  is the rate at which the largest change between the geometric features of the scalar fields occurs. The speeds measured by  $d_{W^q}$ ,  $q = 1, 2$ , keep track of the rate of change between all geometric features, though to some extent,  $d_{W^2}$  suppresses the effect of noise.

Figure 6.7 shows distances  $d_*$  between consecutive sample points, normalized by the maximum distance, using samples taken along almost four periods of the stable RPO. Normalizing  $s_*$  by the maximum speed allows for a straightforward comparison of the different speed profiles. Each of the graphs of  $s_*$  indicate that speed is not uniform along the orbit; there are parts of the orbit where the geometry is changing slowly, separated by intervals of relatively fast evolution. The evolution is extremely slow around the instants corresponding to sample points 100, 240, and 380. The values of the speed (before normalizing) are below the small-scale noise levels given by the first row of Table 6.1. This suggests that the orbit may be passing close to an unstable equilibrium.

While the general shapes of the speed profiles for different distances are similar, there are places where the signs of their derivatives differ. As the system starts

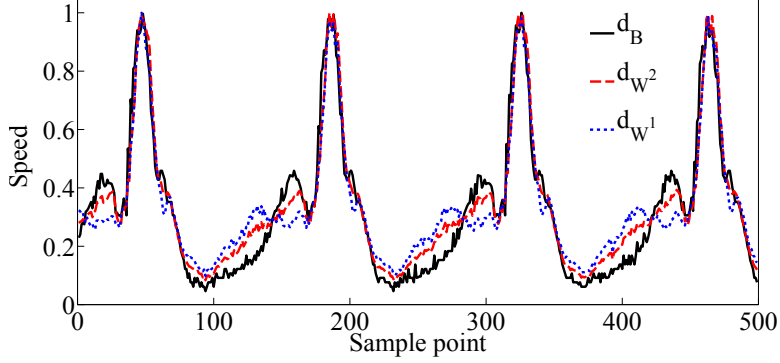


Figure 6.7: The speed  $s_*$ , estimated from the distances  $d_*$  between the consecutive sample points along the stable RPO, plotted for almost four periods. Distances are normalized by their maximum value which is 0.0654 for  $d_B$ , 0.2266 for  $d_{W^2}$ , and 1.9143 for  $d_{W^1}$ . The speed is not uniform along the orbit. Instead, there are parts of the orbit where the dynamics are slow, separated by relatively fast evolution.

accelerating around  $t = 100$ , all three speeds are increasing. Around  $t = 130$ , the speed  $s_{W^1}$  starts decreasing while the other two speeds are still increasing. Note that around  $t = 130$ , the speeds rise above the level of small-scale features (i.e., noise). The fact that  $s_B$  and  $s_{W^2}$  are both increasing means that the changes between the prominent geometric features are growing in this region. The speed  $s_{W^1}$  is decreasing in this region and so the effect of noisy features is decreasing. At  $t = 170$ , the dominant geometric features start to evolve considerably. Changes of the dominant features are the most important contributions to all three metrics. Therefore, the derivatives of the speeds  $s_*$  have the same sign again.

The plots of  $s_*$  hint at the underlying dynamics being that of a periodic orbit. However, it is important to keep in mind that  $\text{Per}$  is an infinite-dimensional space, and thus periodicity in the speed of a trajectory does not imply that the trajectory lies on a closed curve. To conclusively determine that these dynamics are periodic requires a more global geometric analysis of the time series, which is discussed shortly.

With the same data set used to generate Figure 6.7 and letting  $\omega_j$  denote the vorticity field at time  $t_j$ , Figure 6.8 shows the  $d_{W^2}$  distance matrix  $\mathcal{M}$ , with color-coded entries  $\mathcal{M}(i, j) := d_{W^2}(\text{PD}(\omega_i), \text{PD}(\omega_j))$ . (The  $d_B$  and  $d_{W^1}$  distance matrices

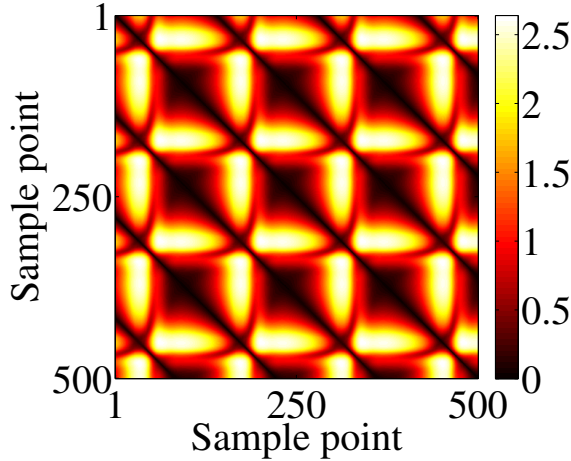


Figure 6.8: A distance matrix  $\mathcal{M}$ , generated by the  $d_{W^2}$  metric, for approximately three periods of the stable RPO. The large black patches correspond to the parts of the orbit with slow dynamics. Equally spaced black lines parallel to the diagonal suggest periodicity of the orbit with period equal to the distance between these lines.

look very similar and are not shown.) Observe that  $\mathcal{M}(i, i) = 0$  and  $\mathcal{M}$  is symmetric since  $\mathcal{M}(i, j) = \mathcal{M}(j, i)$ . Furthermore, Figure 6.7 can be interpreted as a plot of the immediate off-diagonal entries. A striking feature of the distance matrix in Figure 6.8 is the existence of dark lines parallel to the diagonal, spaced at intervals of roughly 110 samples. This indicates that, in the space of persistence diagrams, the trajectory periodically repeats the same, or nearly the same, state. Since the diagonals are spaced at roughly 110 samples, we can indeed say that the orbit revisits very similar states at intervals of roughly 110 samples. Similarly, the light regions close to the diagonal in Figure 6.8 correspond to the times in Figure 6.7 at which the speed is large, indicating significant changes in the pattern at these times. Distance matrices provide a convenient way to visualize dynamics and identify recurrent behavior of a time series of data.

#### 6.4 Analyzing a Point Cloud

The discussion in the previous section suggests that interesting information concerning the dynamics of the geometry of the time-evolving vorticity fields can be obtained

by studying the time series in persistent homology state space,  $\text{Per}$ . Note that each vorticity field is represented by a set of persistence diagrams  $\text{PD}_k(f)$ ,  $k = 1, 2, 3$  which correspond to a single point in  $\text{Per}$ . This time series, with discrete sample points, then forms a *point cloud*  $X$  in  $\text{Per}$  (as introduced in Section 2.2.2). By studying the geometry of this point cloud, useful information about the dynamics can be obtained.

#### 6.4.1 Introduction to the Analysis of Point Clouds

To characterize the geometry of a given point cloud, persistent homology is applied a *second* time by studying the connectivity of the points comprising the point cloud in  $\text{Per}$  as a distance threshold is increased. One can imagine this could be done by growing balls (i.e.,  $N$ -dimensional solid spheres) around each point in the point cloud and tracking the connectivity of the points as the balls intersect one another. The radius of the balls is then the distance threshold  $\theta$ , and as  $\theta$  increases, one can conduct an analysis of the births and deaths of connected components and holes in the point cloud (note that cavities and higher-dimensional homological structures are not considered here). Mathematically, the sublevel sets can now be defined for a new scalar function  $g: \text{Per} \rightarrow [0, \infty)$ . This function gives the distance from any point in  $\text{Per}$  to the point cloud  $X$  and is defined by:

$$g(x) := d(x, X) := \min_{x_i \in X} d(x, x_i), \quad (6.10)$$

where  $d$  is a given metric (bottleneck or Wasserstein with  $q = 1, 2$ ). The sublevel sets  $C(g, \theta)$  in  $\text{Per}$  are then a union of balls:

$$C(g, \theta) = \bigcup_{\text{PD} \in X} B(\text{PD}, \theta), \quad (6.11)$$

where  $B(\text{PD}, \theta) = \{\text{PD}' \in \text{Per} \mid d(\text{PD}', \text{PD}) \leq \theta\}$ , and  $d$  is a given metric.

In general, one should expect that the sets  $C(g, \theta)$  are complicated. Furthermore, tracking the intersections of several  $N$ -dimensional hyperspheres as  $\theta$  is continuously

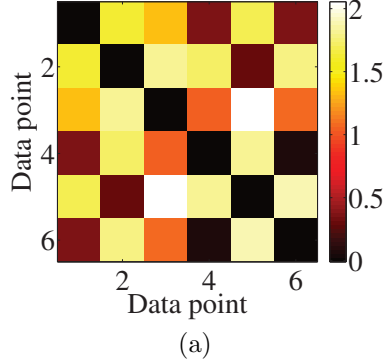
increased could be very computationally expensive. Hence, to carry out the persistent homology analysis of the point cloud, a discrete representation of  $C(g, \theta)$  is used which is known as the *Vietoris-Rips complex*. The Vietoris-Rips complex is nothing more than a discrete collection of *simplexes* which indicate the connectivity of the points. Simplexes are an  $N$ -dimensional generalization of triangles, i.e., for two connected points the simplex is a line, for three a triangle, for four a tetrahedron, and so on. Each union of connected points, lines, triangles, etc. is known as a *simplicial complex*, and the Vietoris-Rips complex is then a collection of all the distinct simplicial complexes as  $\theta$  varies.

Mathematically, the Vietoris-Rips complex is defined as follows. Given a point cloud  $X = \{x_0, \dots, x_N\}$  in a metric space with distance function  $d$ , the Vietoris-Rips complex at scale  $\theta$ , denoted  $R(X, \theta)$ , is defined by the the simplicial complex defined by the collection of simplexes:

$$\{\langle x_{n_0}, \dots, x_{n_k} \rangle \mid d(x_{n_i}, x_{n_j}) \leq 2\theta, \text{ for all } i, j \in \{0, 1, 2, \dots, k\}\}. \quad (6.12)$$

The computations involving the Vietoris-Rips complex were also performed using the Perseus software [166]. Note that there are a variety of references which discuss these concepts in more detail: e.g., [167] for Vietoris-Rips complexes, [168] for discussions of issues related to approximations, and [167, 169] for how one proceeds from a complex to computing persistent homology.

It is worth noting that the Vietoris-Rips complex is determined solely by the distance matrix associated with  $X$ , and hence, there is a finite set of threshold values  $\Theta = \{\theta_i\}$  at which the complex changes. Thus, given a point cloud  $X$  in a metric space with metric  $d$ , the associated persistence diagrams  $PD(X, d)$  are determined by the Vietoris-Rips complexes  $R(X, \theta)$  for  $\theta \in \Theta$ . It is emphasized that the only data used to analyze a point cloud based on the persistent homology of Vietoris-Rips complexes are the pairwise distances between the points given by the distance matrix associated with  $X$ . Two separate examples involving point clouds, one concerned



(a)

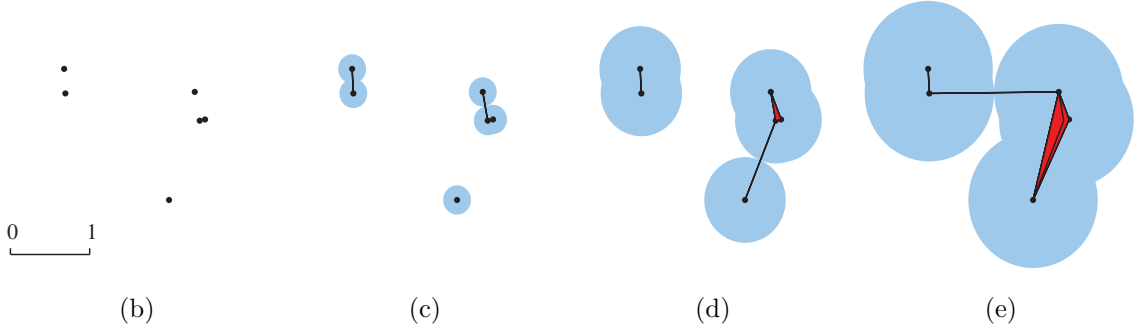


Figure 6.9: (a) A distance matrix representing the pairwise Euclidean distances  $d_E$  between the points in (b), which is a point cloud  $X$ . (c-e) The balls (blue shaded regions) indicate the sublevel sets  $C(X, \theta)$  for  $\theta = 0, 0.1755, 0.5135$ , and  $0.816$ , while the points, lines, and triangles indicate the Vietoris-Rips complexes  $R(X, \theta)$ . For  $\theta = 0.1755$ , as shown in (c), the set  $C(g, \theta)$  consist of three distinct connected clusters; the same is true for  $R(X, \theta)$ . The three components remain distinct until  $\theta = 0.5135$ , shown in (d), at which point two components of  $C(g, \theta)$  merge and a line connecting the points in the merged components appears in  $R(X, \theta)$ . The last merger occurs at  $\theta = 0.816$ , as shown in (e).

with connected components and the other holes, are provided next.

This first example, which is concerned with connected components, illustrates the use of persistent homology as a clustering tool. This idea is demonstrated on a point cloud with pairwise distances given by the distance matrix shown in Figure 6.9 (a). A possible configuration of six points in  $\mathbb{R}^2$  is depicted in Figure 6.9 (b). Using the length scale presented in Figure 6.9 (b) as an indicator of the order of magnitude at which one may want to declare a separation length for the clusters, there are three clusters of points.

Geometric information about the point cloud shown in Figure 6.9 (b-e) is also

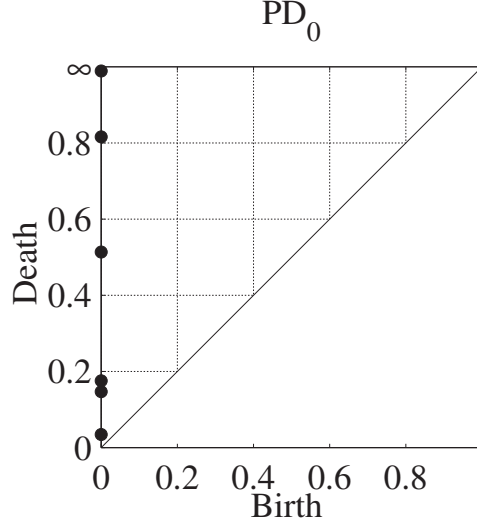


Figure 6.10: Persistence diagram  $\text{PD}_0(X, d_E)$  corresponding to the distance matrix shown in Figure 6.9 (a).

conveyed by  $\text{PD}_0(X, d_E)$  shown in Figure 6.10, where  $d_E$  is the Euclidean distance. Observe that  $C(g, 0) = R(X, 0)$  consists of 6 points. As  $\theta$  increases, the distinct connected components of  $C(g, \theta)$  start merging together. In fact, when the balls  $B(x_i, \theta)$  and  $B(x_j, \theta)$  merge together, a line  $\langle x_i, x_j \rangle$  appears in  $R(X, \theta)$ . Therefore, the connectivity of  $C(g, \theta)$  and  $R(X, \theta)$  are equivalent for all  $\theta \in \mathbb{R}$ , and  $\text{PD}_0(g) = \text{PD}_0(X, d_E)$ . Note that it is impossible for a new connected component to appear for  $\theta > 0$ . Hence, all persistence points in  $\text{PD}_0(X, d_E)$  have a birth value equal to zero. The death coordinates represent the spatial scales at which distinct connected components (clusters) merge together. If one is interested in identifying clusters where the minimal separation is on the order of length scale 1, these clusters correspond to the points in  $\text{PD}_0(X, d_E)$  with the death coordinate greater than approximately 0.5, for which there are three persistence points. Thus, one may conclude that there are three clusters. If the relevant scale for separation is of an order of magnitude smaller, then there are five clusters, since, in addition to the three points with death values greater than 0.5, two points have death values slightly larger than 0.05.

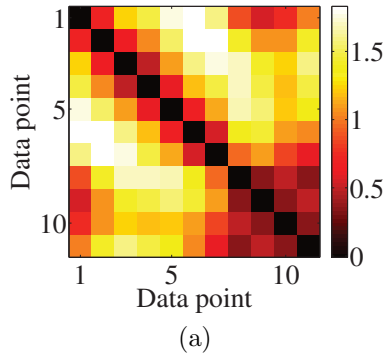
Alternatively, if one was interested in dividing the data into two clusters, then

$\text{PD}_0(X, d_E)$  could be used to determine the magnitude of the separation between the clusters. Observe that the persistence point  $(0, \infty)$  corresponds to the final connected component. The persistence point  $(0, 0.816)$ , with the largest finite death coordinate, indicates that the components merged at a distance 0.816. Hence, the minimal distance between points from the point cloud  $X$  that belong to two distinct clusters is 1.632.

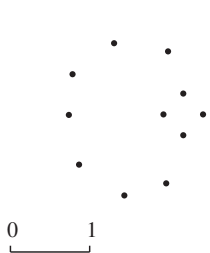
The second example illustrates the use of persistent homology as a tool for identifying periodicity that arises in the dynamics. This periodicity is associated with holes/loops. Consider any point cloud that generates a distance matrix such as the one shown in Figure 6.11 (a). Again, for the sake of intuition, Figure 6.11 (b) provides an example of a point cloud  $X \subset \mathbb{R}^2$  with pairwise distances given by the distance matrix shown. The persistence diagrams for the associated Vietoris-Rips complex filtrations are shown in Figure 6.12.

Applying the reasoning from the previous section, one can ask whether there is a natural or interesting clustering of the data. If, as before, the interest is in clusters where the minimal separation is on the order of length scale 1, shown in Figure 6.11 (b), then  $(0, \infty)$  is the only persistence point with death value greater than 0.5, i.e., at this scale there is only one component. Thus, we conclude that from a geometric perspective the point cloud may be treated as arising from a single dynamical structure.

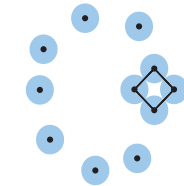
To look for periodic structures, observe that  $\text{PD}_1(X, d_E)$  contains two persistence points. One point occurs at  $(0.177, 0.250)$ , whose birth is shown in Figure 6.11 (b) and whose death occurs at a value of  $\theta$  between that of Figure 6.11 (b) and (c). The other persistence point occurs at  $(0.343, 0.596)$ , whose birth is shown in Figure 6.11 (c) and whose death is shown in Figure 6.11 (d). From this example, it is clear that births of holes/loops occur when lines in the Vietoris-Rips complex form a complete loop, and deaths occur when triangles completely fill in the loop.



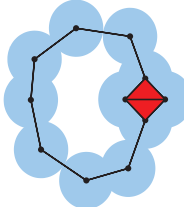
(a)



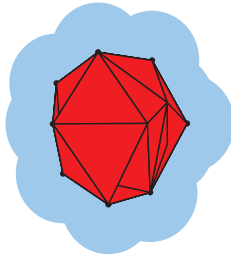
(b)



(c)



(d)



(e)

Figure 6.11: (a) A distance matrix representing the pairwise Euclidean distances  $d_E$  between the points in (b), which is a point cloud  $X$ . (c-e) Sets  $C(f, \theta)$  for  $\theta = 0, 0.177, 0.343$ , and  $0.596$ . The homology of  $C(f, \theta)$  can be approximated using the Vietoris-Rips complex  $R(X, \theta)$  given by the points, lines, and triangles shown in (b-e). The first hole in  $C(f, \theta)$  is created at  $\theta = 0.177$  (corresponding to (c)). This hole is due to the noisy sampling and is filled in almost immediately. The dominant hole is born at  $\theta = 0.343$  (corresponding to (d)) and persists until  $\theta = 0.596$  (corresponding to (e)).

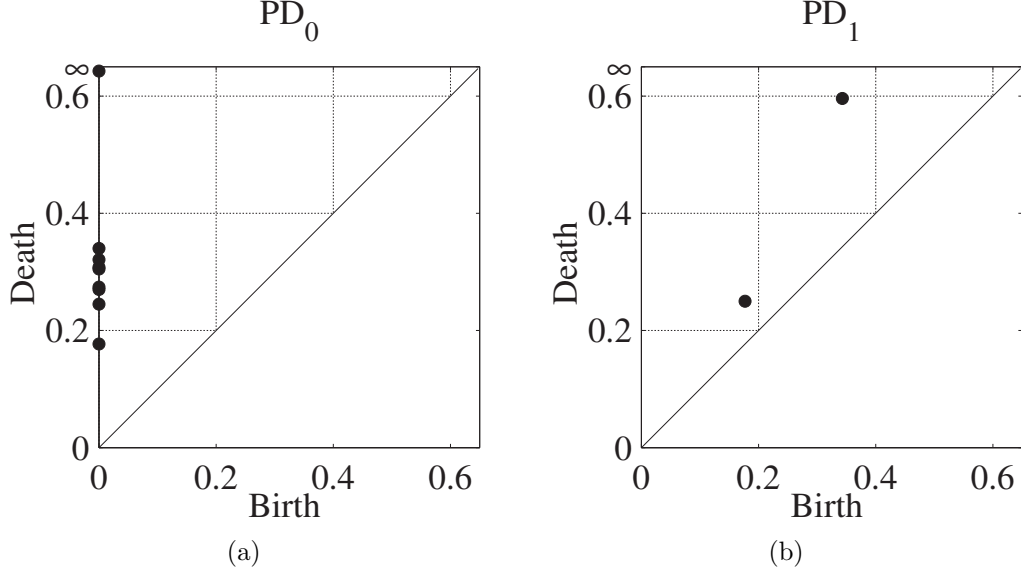


Figure 6.12: Persistence diagrams (a)  $\text{PD}_0(X, d_E)$  and (b)  $\text{PD}_1(X, d_E)$  corresponding to the distance matrix in Figure 6.11 (a). The persistence diagram  $\text{PD}_1(X, d_E)$  contains a dominant point  $(0.343, 0.596)$  corresponding to the robust loop whose birth is shown in Figure 6.11 (d), while the point  $(0.177, 0.25)$  represents the small loop whose birth is shown in Figure 6.11 (c).

To study the importance of these loop features, consider that the life span of point  $(0.177, 0.250)$  is 0.06, which is short compared to the order 1 length scale. Thus it is reasonable to think of this as a result of noise in the data. The life span of point  $(0.343, 0.596)$  is 0.253 and suggests that the point cloud is generated by a loop with a minimal radius of 0.596, which is on the order of the scale of the data. This suggests that the associated loop, whose birth is shown in Figure 6.11 (d), represents an observable, robust dynamical feature.

Characterizing the geometry of a continuous orbit via an approximation by a discrete time series depends on the frequency of sampling, and thus becomes a challenge in the setting of dynamics with multiple time scales, i.e., when the rate of change of the patterns is far from constant. If the sampling rate is too slow, then parts of the orbit will be poorly sampled (or not sampled at all). Note that the geometry of the continuous trajectory may be more complicated than that of a circle; secondary structures might occur if the orbit is twisted, pinched, or bent in  $\text{Per}$ . Thus, the missing

parts of the orbit could distort (or entirely miss) significant features in the geometry of the sampled trajectory as compared to the geometry of the underlying (continuous) dynamics. Thus, in order to obtain a description of the geometry on all relevant spatial scales, including information about secondary structures, the sampling rate needs to be fast enough.

To determine if a trajectory has been sampled densely enough to resolve the geometry of the underlying dynamics, it is useful to compare the following three values related to the point cloud in **Per**: the noise threshold of the system, the maximum consecutive distance in the sampled trajectory, and the diameter of the point cloud. Ideally, once a noise threshold has been computed, one would like distances between consecutive points from the sampled trajectory to be on the length scale of the noise. If sampling faster than this, the features detected from the sample that are on the scale of the noise would be indistinguishable from artifacts generated from the noise in the sample. Thus, ideally, the distance profiles (e.g., Figure 6.7) should have maxima no larger than the noise. Unfortunately, this is not practical for reasons that will be explained next, and fortunately it is often not necessary.

Consider, for example, the case where the length scale of the computational noise is much smaller than the relevant length scale of interest for studying the geometry of the dynamics. In this case, a comparison of the maximum consecutive distance in the sample to the diameter of the point cloud in **Per** is often useful. For instance, if a point cloud has diameter 100 and the smallest relevant length scale for the geometry to be studied is 10, then a maximum consecutive distance of 10 is sufficient for the sampling of the time series, even if the noise threshold is on length scale 1. Thus, it is the interplay of these three numbers that determine if one has sampled a continuous time series densely enough. This interplay has been taking into account in sampling the time evolving dynamics presented below in Section 6.4.3.

### 6.4.2 Distinguishing Flow Fields

The ideas presented in the previous section are now applied to the problem of clustering symmetry-related unstable equilibria of the Kolmogorov-like flow at  $Re = 24.90$ . As discussed in Section 6.1, the turbulent trajectory shown in Figure 6.1 (b) is sampled and EQ and REQ solutions are calculated using a Newton solver. The initial guesses for the Newton solver are the vorticity fields  $\omega$  that are local minima of the  $L_2$  norm of  $\partial\omega/\partial t$ . These converged solutions form a point cloud  $X = \{\text{PD}(\omega_n) \mid n = 1, \dots, 67\}$  of PDs from vorticity fields corresponding to EQ and REQ solutions of the Kolmogorov-like flow. These 67 solutions may be related to one another through any combination of the coordinate transformations listed in Section 6.1. Hence, it is non-trivial to determine how many unique classes of solutions there are and which solutions belong to which class. Persistent homology is used to perform this analysis.

To begin,  $\text{PD}_0(X, d_B)$  is analyzed. The pairwise distances between the points in  $X$  are shown in Figure 6.13 (a). The distance between PDs of vorticity fields related by symmetry is small (but nonzero due to discretization), while PDs corresponding to the vorticity fields that are not symmetry-related differ by a larger amount. This implies that the question of identifying symmetry-related classes of unstable equilibria can be reformulated as a clustering problem.

The diagram  $\text{PD}_0(X, d_B)$ , depicted in Figure 6.13 (b), shows a clear gap between the persistence point with death value  $\theta_d = 0.0285$  and the persistence point with death value  $\theta_d = 0.1215$ . This gap is interpreted as the separation between the signal and noise (numerical errors). Indeed, 0.0285 is just twice the estimate of the lower bound on numerical errors obtained in Section 6.3.1. There are 7 points in  $\text{PD}_0(X, d_B)$  with a death coordinate greater than 0.12, and so it is concluded that there are 7 distinct classes of solutions.

These results from the persistent homology analysis are validated by performing clustering using the Fourier amplitudes as follows. If  $\hat{\omega}(k_x, k_y)$  is the Fourier amplitude

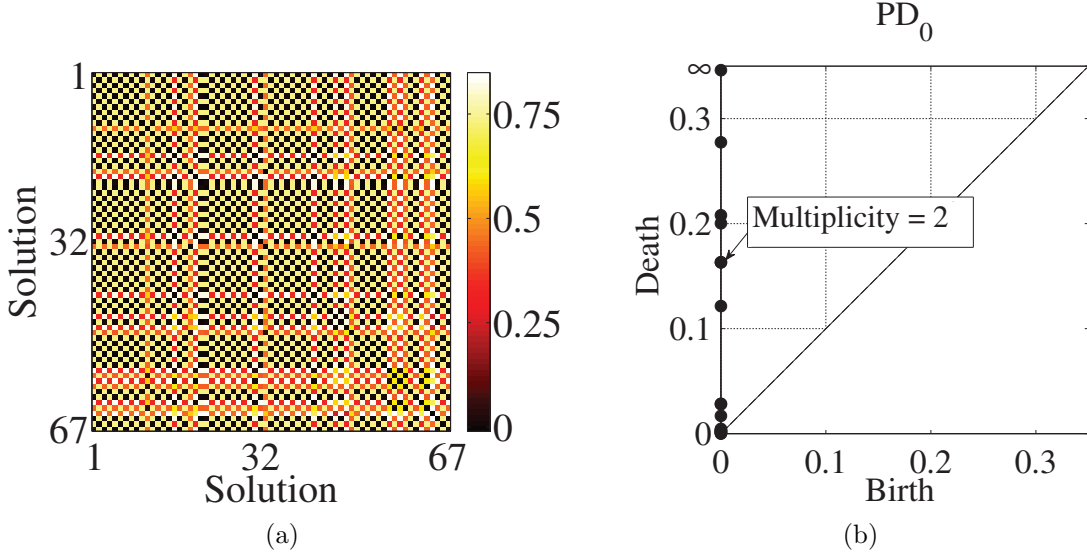


Figure 6.13: (a) Pairwise  $d_B$  distances between the EQ and REQ points in  $X = \{\text{PD}(\omega_n) \mid n = 1, \dots, 67\}$  found at  $Re = 24.90$  using a Newton solver. (b) The corresponding persistence diagram  $\text{PD}_0(X, d_B)$  shows a clear gap between the points with death value  $\theta_d = 0.1215$  and  $\theta_d = 0.0285$ . This gap is interpreted as the separation between the signal and noise.

of a mode  $(k_x, k_y)$ , then a translation of the pattern in the  $x$ - or  $y$ -directions in real space merely adds to the phase of  $\hat{\omega}(k_x, k_y)$ , leaving the magnitude unchanged. Hence, by comparing the amplitudes of the Fourier modes, the vorticity fields which are related by translations can be grouped. Since the conjugate modes  $\hat{\omega}(\pm k_x, \pm k_y)$  relate fields which are related by inversion, to group the vorticity fields which are related by a combination of inversion and translation, the amplitudes of the conjugate modes are summed. Adding the amplitudes of conjugate modes yields a “reduced matrix,” which is unique for all the vorticity fields related by the coordinate transformations that leave equation (6.1) equivariant. This approach also yields 7 distinct classes of solutions.

An analysis of  $\text{PD}_0(X, d_{W^q})$ ,  $q = 1, 2$  yields the same results. There are several gaps between the death values of the points in the PDs. Again one of the gaps starts at roughly twice the value of the estimated lower bound of the noise. However, the separation is less pronounced. As discussed in Section 6.3.1, the  $d_{W^q}$  metrics capture

all the differences between the PDs, and the local numerical errors are summed together. Thus, a large number of small errors can obscure the distinction between the signal and noise.

### 6.4.3 Identifying Periodic Dynamics

The previous section demonstrated the practicality of using persistent homology to perform symmetry reduction and cluster equilibria. In this section, these ideas are extended to the setting of periodic orbits observed in the Kolmogorov-like flow DPS. As is indicated in Figure 6.1 (a), the projection of the orbit onto the imaginary parts of the three dominant Fourier modes suggests a periodic orbit that is undergoing a slow drift in the direction of the continuous symmetry. Since persistent homology is invariant under continuous translation, this type of drift is not present in  $\text{Per}$ . As a result, it is expected that the time series will lie on a closed loop in  $\text{Per}$ . This is consistent with the information provided by the distance matrix shown in Figure 6.7, in which the dark lines parallel to the diagonal indicate that the distance between PDs becomes very small at regular time intervals.

For the remainder of this section, the focus is on verifying that a circle provides a good description of the geometry of the point cloud  $X \subset \text{Per}$  generated by the time series sampled from the RPO. More precisely, it is shown that there is a single dominant feature in  $\text{PD}_0(X, d_B)$  and a single dominant feature in  $\text{PD}_1(X, d_B)$ , which agrees with the PDs corresponding to a circle.

There are two issues that need to be considered: the first is the size of the data set, and the second is the spacing between the data points. As is indicated in Section 6.4, the Vietoris-Rips complex is used to compute persistent homology of point clouds. Given  $n$  data points, the full Vietoris-Rips complex has  $2^n$  cells. Considering this, the analysis herein is performed with the distance matrices corresponding to  $d_B$ ,  $d_{W^1}$ , and  $d_{W^2}$  for 500 points, or roughly three periods of the RPO.

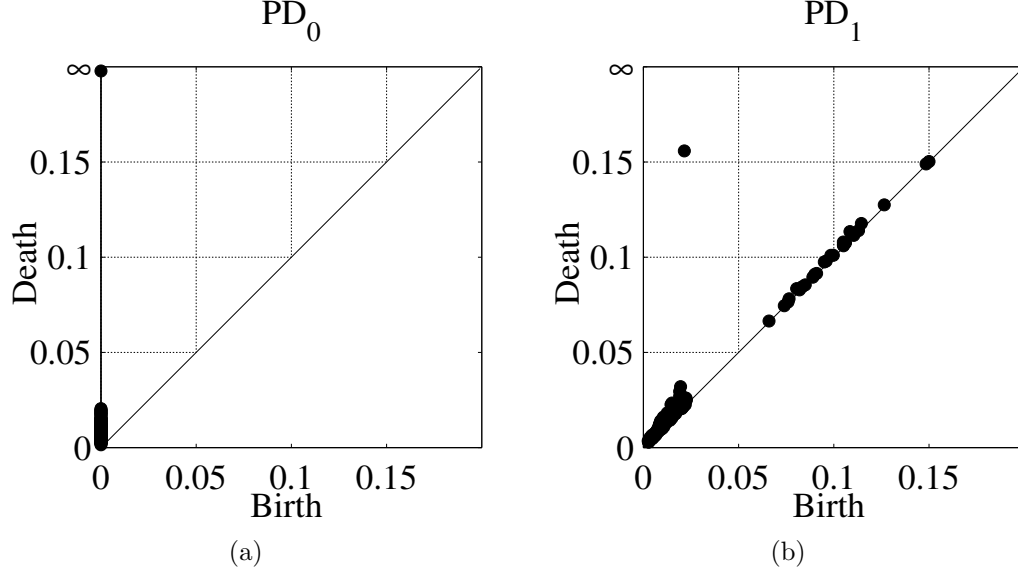


Figure 6.14: (a) The persistence diagram  $\text{PD}_0(X, d_B)$  for RPO at  $Re = 24.90$ . Since all points with finite death coordinates die before 0.025, there is only a single dominant point. (b) The persistence diagram  $\text{PD}_1(X, d_B)$ , showing the single dominant generator at  $(0.0215, 0.1559)$ .

Since a single continuous trajectory is being sampled, it is expected that  $\text{PD}_0(X, d_B)$ , as shown in Figure 6.14 (a), suggests the existence of a single component. The diagrams  $\text{PD}_0(X, d_{W^q})$ ,  $q = 1, 2$ , yield similar results and are not shown. However, it is worth noting that this is not a foregone conclusion as the location of and spacing between the points of the time series are dependent upon the speed along the periodic orbit. As is clear from Figure 6.7, the speed of the trajectory is not constant. However, it is fairly smooth; thus, there is no expectation for extreme differences in the spacings between points.

It is mentioned that the maximum distance between consecutive samples is more than six times larger than the length scale of the noise for this system. However, the diameter of the point cloud is more than forty times larger than the consecutive sample distance. Thus, features on the length scale of one fortieth of the diameter of the entire point cloud will be resolved, which is sufficiently small to consider this an adequate sampling.

Table 6.2: The coordinate of the dominant point in the persistence diagram  $\text{PD}_1(X, d_\star)$  for  $\star = B, W^2, W^1$ , its life span, and the second largest life span.

$\text{PD}_1$	Dominant coordinate	Max life span	$2^{nd}$ largest life span
$d_B$	(0.022, 0.156)	0.134	0.013
$d_{W^2}$	(0.075, 0.405)	1.366	0.105
$d_{W^1}$	(0.703, 2.069)	0.330	0.016

As indicated in Figure 6.14 (b), the persistence diagram  $\text{PD}_1(X, d_B)$  clearly detects a single dominant loop along which the data is organized. Thus, it is concluded that in  $\text{Per}$ , equipped with the metric  $d_B$ , the point cloud  $X$  generated by the time series forms a loop with a minimal radius of 0.1344. Table 6.2 shows the coordinates of the point with the longest life span, its life span value, and the second longest life span for each of the diagrams  $\text{PD}_1(X, d_\star)$ ,  $\star \in B, W^2, W^1$ . As the table indicates, the life span of the dominant point is an order of magnitude larger than the next longest life span in each case, and so there is a single dominant feature in  $\text{PD}_1(X, d_\star)$ . Additionally, note that the second longest life span values are as small or smaller than the lower bounds on numerical errors indicated by the first row of Table 6.1.

## 6.5 Discussion

Persistent homology provides a powerful mathematical formalism for dimensionality reduction. By encoding the topological features of a scalar function into a set of PDs, a substantial reduction is performed. In the case of the snapshot shown in Figure 6.2, the associated PDs (show in Figure 6.3 (d-f)) have less than 10 dominant points each. However, despite this reduced description, one can still apply a metric to the space of PDs which allows for quantitative characterization of the dynamics with bounded errors. In particular, three different metrics on the space of PDs have been used for studying pattern evolution on large versus small spatial scales. These metrics offer an estimate of the numerical error in the space of PDs.

Constructing a set of PDs for a given flow field can be thought of as plotting a

single point in the persistent homology state space,  $\text{Per}$ . A collection of flow fields, then, corresponds to a point cloud in  $\text{Per}$ . With a chosen metric in hand, one can then use the Vietoris-Rips complex to study the structure of this point cloud. By studying point clouds in two-dimensional Euclidean space, one can develop intuition for this approach. In  $\text{Per}$ , this second application of persistent homology can be used to cluster equilibria and identify periodic dynamics, as demonstrated. This method is particularly useful when solutions must be identified that lie on a group orbit.

The efficacy of these methods has been demonstrated using a Kolmogorov-like flow simulation with doubly-periodic boundary conditions, and the results have been compared to traditional Fourier methods where appropriate. These results show that the geometry of the dynamics are recovered in each case. An extension of this analysis to the other simulations (the SPS and NPS) would be very straightforward. Furthermore, this method is robust to noise, suggesting that it is appropriate for studying dynamics on data sets obtained experimentally.

## CHAPTER VII

### CONCLUSIONS

In the research presented in this dissertation, two dimensionality reduction methods have been used to describe the dynamics of a canonical two-dimensional (2D) flow known as Kolmogorov flow. The experiment, which is quasi-two-dimensional, approximates Kolmogorov flow by driving two thin fluid layers with electromagnetic forces. The fact that the experimental flow can be treated as effectively 2D is very appealing in comparison to more onerous three-dimensional (3D) flows. Specifically, imaging 2D flows is substantially easier and the computational costs associated with performing PIV and simulating the flow are considerably less. Hence, this more tractable 2D flow provides a convenient platform for testing new approaches to understanding turbulence.

In modeling the experimental flow, numerous aspects have been considered in order to obtain a simulation which quantitatively captures the dynamics of the experiment. The model, introduced in Chapter 3, was derived by depth-averaging the full 3D Navier-Stokes equation over the confined direction. The resulting equation has a prefactor to the advection term,  $\beta$ , which has been unaccounted for in all previous studies. Additionally, this derivation produces analytical expressions which provide estimates for all parameters in the model; these parameters are calculated using properties of the fluid layers. The boundary conditions have also been chosen carefully. Many dynamical studies of turbulence, in both 2D [79–81] and 3D [61, 65–71], have employed periodic boundary conditions. However, it was found that the periodic simulations explored here hardly offer qualitative agreement with the experiment.

Rather, it is necessary to impose no-slip boundary conditions along all lateral boundaries, as is the case for the non-periodic simulation. When comparing the experiment and non-periodic simulation, the flow fields for both the straight and modulated flows look virtually indistinguishable. Furthermore, the critical Reynolds numbers for the first two bifurcations observed in the experiment and non-periodic simulation agree to within a few percent. The purpose of this validation in the preturbulent regime was to obtain a version of the simulation which would capture the dynamics of the experiment in the weakly turbulent regime as closely as possible.

The results presented in Chapter 5 provide unambiguous evidence supporting the claim that the experimental turbulent trajectory visits the neighborhoods of unstable equilibrium ECS in state space. In this approach, unstable equilibria have been calculated directly from experimental flow fields based on a dynamical criterion—that the rate of evolution be a local minimum, as it should when a turbulent trajectory passes near such a solution. These ECS closely resemble the experimental flow fields at these instants. Furthermore, this chapter presents the first demonstration of deterministic forecasting of a weakly turbulent fluid flow in the laboratory. This was done by calculating the unstable manifold associated with an unstable equilibrium. Although it cannot be expected that the eigenvalues associated with an ECS will always show a hierarchy, it is a general result that when this does happen, the local dynamics are guided by an even lower-dimensional *submanifold*. For the particular unstable equilibrium considered here, the seven-dimensional (7D) unstable manifold can be reduced to an effectively one-dimensional (1D) unstable submanifold because the leading eigenvalue is much larger than the rest. The dimensionality reduction offered by ECS is tremendous. In this demonstration, the flow is evolving in essentially a  $10^6$ -dimensional space (the number of grid points in the simulation), but in the vicinity of this unstable equilibrium the dynamics are reduced to a 7D subspace, which is in turn reduced even further to a 1D subspace.

The forecasting demonstrated in this dissertation is only a small step towards building a predictive framework. There are several important extensions which have yet to be made. Perhaps most importantly, it is necessary to include unstable periodic orbits in these calculations, which are thought to be dynamically more important than unstable equilibria [170]. In particular, such calculations would enable experimental testing of *periodic orbit theory* [171], which provides a framework for calculating dynamical averages of observables (e.g., dissipation or turbulent drag [77]) from ECS. The calculation of heteroclinic and homoclinic connections between ECS should allow for forecasting over longer periods of time. In fact, by constructing a network of such connections between the dynamically-relevant ECS, it may be possible to describe turbulent evolution using *symbolic dynamics* [78, 171].

This picture also hints at the possibility for very effective control. Knowledge of the structure of heteroclinic and homoclinic connections between ECS in state space would allow one to apply low cost, highly effective perturbations to “steer” a turbulent trajectory towards a desired state. Ultimately, this approach could enable relaminarization of turbulent flows at high Reynolds numbers, which would be revolutionary throughout industry and engineering. Beyond the development of a deterministic framework for prediction and control of turbulence, there is still immense value in calculating ECS, in that each solution can be thought of as a fundamental process driving turbulence [79]. Therefore, the spatial and temporal properties of these solutions can be studied to gain insight into the underlying physics. Studies of ECS have already uncovered many physical mechanisms generating and sustaining turbulence [73].

Unlike the ECS-based approach, which has been gaining momentum over the last 15 years or so, persistent homology is a much newer method for characterizing turbulence, and hence requires careful consideration to ensure that the proper conclusions are drawn from the results. For this reason, Chapter 6 was largely restricted to

analyses which could be verified via alternative methods. The results of this chapter show that persistent homology can be used to compare flow fields, probe the geometric features of patterns on different scales, and measure the rate of evolution of a time series. Although such analyses can be performed using alternative methods, persistent homology is perhaps preferable for characterizing fluid flows because it automatically removes any redundancies that may arise due to the symmetries of a system's governing equations.

Persistent homology offers an approach to dimensionality reduction that is quite different from that of the ECS-based approach. This method relies on the generation of persistence diagrams, in which each point corresponds to a unique, well-defined geometric feature. The points that have the largest life span, i.e. those farthest from the diagonal, are considered the most dominant features, while those close to the diagonal can be considered noisy features which may be neglected. This allows for a substantial dimensionality reduction. For example, the flow field shown in Figure 6.2 is in principle 16,384-dimensional (it is generated using  $128^2$  Fourier modes); however, a collection of fewer than 20 dominant points in the persistence diagrams capture the geometric features of this pattern. Beyond the analysis conducted here, persistence diagrams provide a powerful tool for characterizing patterns in  $N$  dimensions. This suggests that persistent homology may prove useful in probing the physical structure of 2D and 3D turbulent flows at arbitrarily high Reynolds numbers.

Perhaps the most useful feature of persistent homology demonstrated here is the ability to identify structures in persistent homology state space,  $\text{Per}$ . In the example from Section 6.4.3, a relative periodic orbit is identified as a loop structure in  $\text{Per}$ . This deduction is based purely on a series of observations of the flow fields. Extension of this analysis to experimental data should be very straightforward, as persistent homology is known to be robust to the noise associated with experimental measurements. In future research, applying this methodology in the turbulent regime

may offer insight into the low-dimensional attractor guiding the turbulent dynamics. An attractive feature is that this can be achieved directly from experimental observations, with no modeling required. This is very much in the same spirit as the time delay embedding, but more powerful because this methodology uses the full spatial and temporal information available.

There are many open questions remaining and the possibility for complementary overlap between these two approaches to dimensionality reduction. For example, the two measures of the rate of evolution given by equations (5.2) and (6.9) offer different results when applied to the same time series. It is not yet known which quantity offers a better measure of the proximity to an unstable equilibrium. Additionally, the use of persistent homology to identify periodic structures in the turbulent regime may prove useful in identifying optimal initial conditions for calculating periodic orbit ECS. The utility of these methods is currently being studied in the context of fluid turbulence, but such tools may prove useful in many other systems which exhibit dynamics that are complicated in space and time. Specifically, future extensions of these approaches may enable better weather forecasting, improve engineering process control, or offer insight into the dynamics of biological systems (e.g., epilepsy and cardiac arrhythmias).

## APPENDIX A

### PARTICLE IMAGE VELOCIMETRY

Particle image velocimetry (PIV) refers to a methodology which has emerged in the last two decades in which the instantaneous velocity field of a fluid flow is determined by measuring the displacements in flow patterns arising from several tracer particles which follow the motion of the fluid. Some general PIV concepts will be discussed here, but for a thorough introduction to PIV, see references [148, 149]. In 2D, the general concept of PIV is the following. A pair of images of the seeded flow is collected with some known amount of time  $dt$  between the frames. The first image is then divided into several smaller interrogation windows. For each window, a cross-correlation is performed with the second image to determine how much that region of flow has been displaced. This results in an array of displacement fields along each direction,  $d_x$  and  $d_y$ . Since  $dt$  is known and the relation between physical length and pixels can be determined using a calibration target, these displacement fields can be converted to velocity fields. By analyzing a time series of images, one can obtain temporally and spatially resolved velocity fields.

A few PIV parameters are first introduced before proceeding to discussion of the PIV software. The *correlation step* is a PIV parameter which must be chosen for each PIV processing job. For a fixed camera frame rate of 15 Hz, choosing a correlation step of 1, 2, 3, etc. corresponds to setting  $dt$  equal to 1/15 s, 2/15 s, 3/15 s, etc. It is necessary to carefully choose the correlation step by taking into account the speed of the flow in pixels. This is generally not known *a priori* but rather a few PIV trial runs must be conducted to determine a good correlation step. As a general rule of thumb, the correlation step should be chosen such that the “one-quarter rule” [148]

is approximately satisfied. This rule states that the maximum pixel displacement should approximately equal one-quarter of the size of the interrogation window. For example, if the interrogation window is  $24 \times 24$  pixels, then the correlation step should be chosen such that the maximum pixel displacement is about 6.

The *frame step* is a PIV parameter which should not be confused with the correlation step. The frame step is simply the number of images to skip when performing PIV on a time series. For example, in a time series of 45 images, a correlation step of 2 and a frame step of 15 means that images 1 and 3, images 16 and 18, and images 31 and 33 will be correlated. Typically, for Kolmogorov-like flow, a frame step of 15 is acceptable, as the flow does not change significantly in 1 s. If necessary, smaller frame steps can be used and then the velocity fields can be averaged over small windows to reduce noise.

## A.1 Prana

The Prana software package has many appealing features. It comes complete with a graphic user interface, as well as the option for running PIV jobs from the command line. It offers an option for parallel computing and a mask can be applied to exclude regions outside the flow domain from the PIV calculations. Prana has several PIV methods, but the one that is best for Kolmogorov-like flow is the “Multigrid - Deform (CWO)” option. This method iteratively deforms images to better resolve the high shear in the flow. Two sets of Prana parameters are provided below. The first is a “standard” set of parameters, which has been used for the experimental data presented in Chapter 4. The second is a “fine” set of parameters which results in velocity fields with considerably higher spatial resolution. This second set of parameters has been used for the experimental data presented in Chapter 5, particularly for the experimental velocity fields which were used as initial conditions in the Newton solver.

### A.1.1 “Standard” Parameters

#### -----PIV Processing-----

Algorithm: Multigrid - Deform (DWO)  
Velocity Interp Function: Cubic  
Image Interpolation Function: Cardinal Function w/ Blackman Filter

#### -----Pass 1 Setup-----

Window Resolution (first image) (pix): 32,32; 32,32  
Window Resolution (second image) (pix): 32,32; 32,32  
Window Size (pix): 64,64  
Grid Resolution (pix): 8,8  
Window Overlap Percentage: 75,75  
Grid Buffer (pix): 8,8  
Bulk Window Offset (pix): 0,0  
Correlation:  
    RPC Diameter: 2.8,2.8  
Zero-Mean Image Windows: Yes  
Subpixel Peak Location Method: Three-Point Gaussian  
Smoothing:  
    Smoothing Weight (STD): 2  
Deformation Information:  
    Minimum Number of Iterations: 2  
    Maximum Number of Iterations: 5  
    Convergence Error: 0.1  
Validation Type(s): UOD  
UOD Type: Median  
UOD Window Sizes: 3,3;3,3

UOD Thresholds:	3,2
Try Additional Peaks:	No
Write Output:	No

-----Pass 2 Setup-----

Window Resolution (first image) (pix):	24,24;24,24
Window Resolution (second image) (pix):	24,24;24,24
Window Size (pix):	64,64
Grid Resolution (pix):	8,8
Window Overlap Percentage:	66.6667,66.6667
Grid Buffer (pix):	8,8
Bulk Window Offset (pix):	0,0
Correlation:	RPC
RPC Diameter:	2.8,2.8
Zero-Mean Image Windows:	Yes
Subpixel Peak Location Method:	Three-Point Gaussian
Smoothing:	No
Deformation Information:	
Minimum Number of Iterations:	2
Maximum Number of Iterations:	5
Convergence Error:	0.1
Validation Type(s):	UOD
UOD Type:	Median
UOD Window Sizes:	3,3;3,3
UOD Thresholds:	3,2
Try Additional Peaks:	No
Write Output:	Yes

Output Basename:	PIV_pass2_
Save Add. Peak Info:	No
Save Correlation Planes:	No

### A.1.2 “Fine” Parameters

-----PIV Processing-----

Algorithm:	Multigrid - Deform (DWO)
Velocity Interp Function:	Cubic
Image Interpolation Function:	Cardinal Function w/ Blackman Filter

-----Pass 1 Setup-----

Window Resolution (first image) (pix):	32,32; 32,32
Window Resolution (second image) (pix):	32,32; 32,32
Window Size (pix):	64,64
Grid Resolution (pix):	8,8
Window Overlap Percentage:	75,75
Grid Buffer (pix):	8,8
Bulk Window Offset (pix):	0,0
Correlation:	RPC
RPC Diameter:	2.8,2.8
Zero-Mean Image Windows:	Yes
Subpixel Peak Location Method:	Three-Point Gaussian
Smoothing:	Yes
Smoothing Weight (STD):	2
Deformation Information:	
Minimum Number of Iterations:	2

Maximum Number of Iterations:	5
Convergence Error:	0.08
Validation Type(s):	UOD
UOD Type:	Median
UOD Window Sizes:	3,3;3,3
UOD Thresholds:	3,2
Try Additional Peaks:	No
Write Output:	No

-----Pass 2 Setup-----

Window Resolution (first image) (pix):	24,24;24,24
Window Resolution (second image) (pix):	24,24;24,24
Window Size (pix):	64,64
Grid Resolution (pix):	8,8
Window Overlap Percentage:	66.6667,66.6667
Grid Buffer (pix):	8,8
Bulk Window Offset (pix):	0,0
Correlation:	RPC
RPC Diameter:	2.8,2.8
Zero-Mean Image Windows:	Yes
Subpixel Peak Location Method:	Three-Point Gaussian
Smoothing:	Yes
Smoothing Weight (STD):	2
Deformation Information:	
Minimum Number of Iterations:	2
Maximum Number of Iterations:	5
Convergence Error:	0.08

Validation Type(s):	UOD
UOD Type:	Median
UOD Window Sizes:	3,3;3,3
UOD Thresholds:	3,2
Try Additional Peaks:	No
Write Output:	No

-----Pass 3 Setup-----

Window Resolution (first image) (pix):	24,24;24,24
Window Resolution (second image) (pix):	24,24;24,24
Window Size (pix):	64,64
Grid Resolution (pix):	6,6
Window Overlap Percentage:	75,75
Grid Buffer (pix):	8,8
Bulk Window Offset (pix):	0,0
Correlation:	RPC
RPC Diameter:	2.8,2.8
Zero-Mean Image Windows:	Yes
Subpixel Peak Location Method:	Three-Point Gaussian
Smoothing:	No
Deformation Information:	
Minimum Number of Iterations:	2
Maximum Number of Iterations:	5
Convergence Error:	0.08
Validation Type(s):	UOD
UOD Type:	Median
UOD Window Sizes:	3,3;3,3

UOD Thresholds:	3,2
Try Additional Peaks:	No
Write Output:	Yes
Output Basename:	PIV_pass3_
Save Add. Peak Info:	No
Save Correlation Planes:	No

## APPENDIX B

### UNIDIRECTIONAL FLOW

In this appendix, a derivation for the vertical profile  $P(z)$  of the horizontal velocity is provided for the case of unidirectional flow. Although the unidirectional flow cannot be realized in the experiment, it allows for the derivation of simple expressions for  $\alpha$ ,  $\bar{\nu}$ ,  $\bar{\rho}$ , and  $\beta$  in equation (3.9), which are helpful in understanding the parametric dependence of these coefficients. As mentioned in Section 3.2.3, the unidirectional flow can be interpreted as the limiting case of very wide magnets where the  $y$ -dependence of the magnetic field  $B_z$  is ignored (i.e.,  $\kappa \rightarrow 0$ ). The form of  $\mathbf{u}(x, y, t)$  is then also unidirectional, i.e.,  $\mathbf{u}(x, y, t) = u_0 \hat{\mathbf{x}}$ .

Substituting this into equations (3.8) yields a hydrostatic pressure distribution and a boundary value problem for the vertical profile  $P(z)$ :

$$\begin{aligned} P'' &= -\frac{J}{u_0 \mu_e} (B_1 z + B_0), \quad h_d < z < h_d + h_e, \\ P'' &= 0, \quad \quad \quad 0 < z < h_d \end{aligned} \tag{B.1}$$

where the prime denotes differentiation with respect to  $z$ . The solution to equations (B.1) is given by:

$$P = \begin{cases} -\frac{JB_1}{6u_0\mu_e} z^3 - \frac{JB_0}{2u_0\mu_e} z^2 + Cz + D, & h_d < z < h_d + h_e, \\ Ez + F, & 0 < z < h_d. \end{cases} \tag{B.2}$$

To solve for  $u_0$ ,  $C$ ,  $D$ ,  $E$ , and  $F$ , one must use the boundary conditions that  $P(z)$  must satisfy. These are the no-slip boundary condition at the bottom of the dielectric ( $z = 0$ ), the continuity of the velocity and stress at the dielectric-electrolyte interface ( $z = h_d$ ), and the stress-free and normalization boundary conditions at the top (free)

surface of the electrolyte ( $z = h_d + h_e$ ):

$$\begin{aligned} P(0) &= 0, & P(h_d^-) &= P(h_d^+), & \mu_d P'(h_d^-) &= \mu_e P'(h_d^+), \\ P'(h_d + h_e) &= 0, & P(h_d + h_e) &= 1. \end{aligned} \quad (\text{B.3})$$

Using these boundary conditions to solve equations (B.2), one obtains:

$$u_0 = S \frac{h_e h_d}{\mu_d} J \langle B \rangle, \quad (\text{B.4})$$

$$C = \frac{1}{S} \frac{\mu_d}{\mu_e} \left( \frac{h_e + h_d}{h_e h_d} \right) \left( 1 - \frac{1}{2} \frac{h_d}{h_e} \frac{\Delta B}{\langle B \rangle} \right), \quad (\text{B.5})$$

$$D = \frac{1}{S} \frac{\mu_d h_d}{\mu_e h_e} \left[ \frac{\mu_e h_e}{\mu_d h_d} - \frac{h_e}{h_d} - \frac{1}{2} + \left( \frac{1}{4} + \frac{1}{6} \frac{h_d}{h_e} \right) \frac{\Delta B}{\langle B \rangle} \right], \quad (\text{B.6})$$

$$E = \frac{1}{h_d S} \quad \text{and} \quad F = 0. \quad (\text{B.7})$$

It turns out that the shape of the vertical profile in the case of unidirectional flow is virtually indistinguishable from that of Kolmogorov flow, as illustrated in Figure B.1. This suggests that Q2D flows with arbitrary horizontal flow profiles  $\mathbf{u}(x, y, t)$  and moderately high Reynolds numbers (up to  $Re \approx 40$ ) may be accurately described using the velocity profile from the simpler, unidirectional case.

Using  $P(z)$ , analytical expression are now provided for  $S$  and the parameters in equation (3.9). The measure of two-dimensionality,  $S$ , is given by:

$$S = 1 + \frac{1}{2} \frac{\mu_d h_e}{\mu_e h_d} \left( 1 + \frac{1}{6} \frac{\Delta B}{\langle B \rangle} \right), \quad (\text{B.8})$$

where  $\Delta B = B_1 h_e$  is the change in magnetic field across the electrolyte and  $\langle B \rangle = B_0 + B_1 h_d + \frac{1}{2} B_1 h_e$  is the mean magnetic field in the electrolyte. For the Rayleigh friction coefficient, one obtains:

$$\alpha = \frac{\frac{\mu_d}{\rho_e} \frac{1}{h_d h_e}}{1 + \frac{1}{2} \frac{h_d}{h_e} \frac{\rho_d}{\rho_e} + \frac{1}{3} \frac{h_e}{h_d} \frac{\mu_d}{\mu_e} \left( 1 + \frac{1}{8} \frac{\Delta B}{\langle B \rangle} \right)}. \quad (\text{B.9})$$

For the depth-averaged kinematic viscosity, one obtains:

$$\bar{\nu} = \nu_e \frac{1 + \frac{1}{2} \frac{h_d}{h_e} \frac{\mu_d}{\mu_e} + \frac{1}{3} \frac{h_e}{h_d} \frac{\mu_d}{\mu_e} \left( 1 + \frac{1}{8} \frac{\Delta B}{\langle B \rangle} \right)}{1 + \frac{1}{2} \frac{h_d}{h_e} \frac{\rho_d}{\rho_e} + \frac{1}{3} \frac{h_e}{h_d} \frac{\mu_d}{\mu_e} \left( 1 + \frac{1}{8} \frac{\Delta B}{\langle B \rangle} \right)}. \quad (\text{B.10})$$

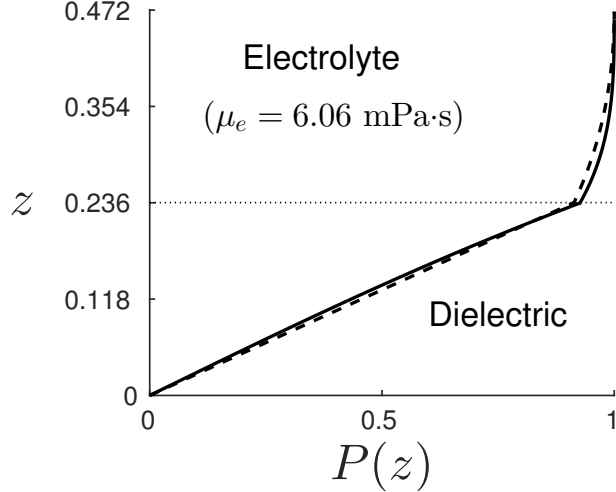


Figure B.1: Analytical results for the vertical profile of the horizontal flow field in both layers, with  $h_d = h_e = 0.236$ . The Kolmogorov flow corresponds to the solid line, while the unidirectional flow corresponds to the dashed line. The ratios of the velocities, as defined by equation (3.13), are:  $S = 1.10$  for unidirectional flow and  $S = 1.08$  for Kolmogorov flow.

For the depth-averaged density, one obtains:

$$\bar{\rho} = \frac{\rho_e}{h_d + h_e} \left[ 1 + \frac{1}{2} \frac{h_d \rho_d}{h_e \rho_e} + \frac{1}{3} \frac{h_e \mu_d}{h_d \mu_e} \left( 1 + \frac{1}{8} \frac{\Delta B}{\langle B \rangle} \right) \right]. \quad (\text{B.11})$$

The exact expression for  $\beta$  is too complicated to yield much insight, but it can be evaluated using the profile  $P(z)$  and the coefficients for any set of experimental parameters. It should be noted that, for the values of parameters used in the experiment, the coefficients  $S$ ,  $\alpha$ ,  $\bar{\nu}$ ,  $\bar{\rho}$ , and  $\beta$  have a very weak dependence on  $\epsilon = \Delta B/\langle B \rangle$ : setting  $\epsilon = 0$  changes the values by less than 5%. In the limit where  $\epsilon = 0$ , one finds:

$$\beta = \frac{1 + \frac{1}{3} \frac{h_d \rho_d}{h_e \rho_e} + \frac{2}{3} \frac{h_e \mu_d}{h_d \mu_e} + \frac{2}{15} \frac{h_e^2 \mu_d^2}{h_d^2 \mu_e^2}}{1 + \frac{1}{2} \frac{h_d \rho_d}{h_e \rho_e} + \frac{5}{6} \frac{h_e \mu_d}{h_d \mu_e} + \frac{1}{4} \frac{\rho_d \mu_d}{\rho_e \mu_e} + \frac{1}{6} \frac{h_e^2 \mu_d^2}{h_d^2 \mu_e^2}}. \quad (\text{B.12})$$

Similarly, for the case of Kolmogorov flow, the dependence on  $\kappa$  is also very weak. Evaluating the coefficients using  $P(z)$  from Kolmogorov flow instead of unidirectional flow changes their values by less than 6%.

Expression (B.8) suggests that even if the magnetic field across the electrolyte were uniform, i.e.  $\Delta B = 0$ , the flow in the electrolyte would still deviate significantly

from being perfectly 2D. For a typical case where  $\mu_e = \mu_d$  and  $h_e = h_d$ , one obtains  $S = 1.5$ . Using instead the value  $\epsilon = -0.6$  corresponding to the experiment gives  $S = 1.45$ . Hence, the decay in the magnetic field does *not* contribute significantly to the deviation from two-dimensionality. Expression (B.8) also suggests that the shallower the electrolyte layer is (relative to the dielectric layer), the closer one comes to a vertically uniform profile in the electrolyte ( $S = 1$ ). However, electrolyte layers with thickness less than about 0.236 (dimensionally, 0.3 cm) are found to be unstable in the experiment, as they break up to form configurations that correspond to lower total surface energy. Alternatively, one may increase the thickness  $h_d$  of the dielectric layer. This has the drawback that one moves farther from the magnets, requiring larger currents to drive the flow. Also, the Q2D approximation, an assumption whose validity depends partially on strong geometric confinement, is compromised. Hence, the most straightforward way to improve the two-dimensionality of the electrolyte is by increasing the ratio of viscosities. The optimal choice of the electrolyte viscosity is not obvious. For the variation in the velocity of the electrolyte to be at most 10%,  $\mu_e$  should exceed the solution of equation (B.8) with  $S = 1.1$ . Substituting the typical values of  $\mu_d = 1.30$  mPa·s,  $\epsilon = -0.6$ , and  $h_d = h_e$  gives  $\mu_e \geq 5.85$  mPa·s.

## APPENDIX C

### NUMERICAL METHODS

In this Appendix, details are provided concerning the spatial and temporal discretizations and the numerical integration schemes employed in the Kolmogorov-like flow simulations.

#### C.0.3 Non-Periodic Simulation (NPS) and Singly-Periodic Simulation (SPS)

Since the NPS, as well as the SPS, require prescribing no-slip (e.g., Dirichlet) boundary conditions on the velocity field  $\mathbf{u}$ , numerical simulations are performed using the primitive variable ( $u_x$ ,  $v_x$ , and  $p$ ) formulation by employing a semi-implicit fractional-step method detailed in [158]. To begin with, equation (3.9) is discretized in time to obtain the following difference equation:

$$\frac{\mathbf{u}_{n+1} - \mathbf{u}_n}{\Delta t} + \frac{3}{2}\mathcal{N}\mathbf{u}_n - \frac{1}{2}\mathcal{N}\mathbf{u}_{n-1} = -\frac{1}{\rho}\nabla p_{n+1} + \frac{1}{2}\mathcal{L}(\mathbf{u}_{n+1} + \mathbf{u}_n) + \mathbf{f}. \quad (\text{C.1})$$

In the above equation  $\mathbf{u}_n$  and  $p_{n+1}$  are the velocity and kinematic pressure fields with the subscript  $n$  indicating a discrete time instant  $t_n = n\Delta t$ , where  $\Delta t$  is the time step for the update. For purposes of brevity, the notation  $\mathcal{N}\mathbf{u}_n = \beta\mathbf{u}_n \cdot \nabla\mathbf{u}_n$  and  $\mathcal{L}\mathbf{u}_n = \nabla^2\mathbf{u}_n - \alpha\mathbf{u}_n$  have been used to represent the nonlinear and linear terms, respectively. The above equation results from a semi-implicit approximation for the temporal evolution described by equation (3.9), where the linear terms in the update are treated implicitly using the Crank-Nicholson scheme, while the nonlinear term is handled explicitly using the Adams-Basforth scheme. The velocity field  $\mathbf{u}_{n+1}$  at every instant satisfies the incompressibility condition:

$$\nabla \cdot \mathbf{u}_{n+1} = 0, \quad (\text{C.2})$$

which is enforced on each update through the three-fractional-step P2 (pressure correction) projection method discussed in [158].

Spatial discretization of the velocity and pressure fields is carried out using the standard marker and cell (MAC) staggered grid [172]. The spatial derivatives in equation (C.1) are approximated using finite differences; the 2D Laplacian operator ( $\nabla^2$ ) uses a five-point stencil formula and the nonlinear term uses a modified MAC formula [173].

For both the NPS and the SPS, 20 cells per magnet width  $w$  have been chosen discretizing the velocity and pressure fields. Since the dimensions of the NPS are identical to the lateral dimensions of the experiment, i.e.,  $14w \times 18w$ , a total of  $280 \times 360$  cells were used to sample the flow domain. The SPS, however, corresponds to a domain of dimensions  $14w \times 8w$ , which maps to a region including the central eight magnets in the experiment. Hence, a total of  $280 \times 160$  cells were used to discretize the SPS domain. For both the SPS and NPS, a time step of  $\Delta t = 1/40$  s was used for all the numerical simulations.

#### C.0.4 Doubly-Periodic Simulation (DPS)

Simulations on the doubly-periodic domain can be sped up significantly using a spectral method [157]. Since solving linear equations involving the Laplacian is very cheap in the spectral method, it is convenient to use the vorticity-stream function formulation instead of the velocity-pressure formulation. Taking the curl of equation (3.9), one obtains the following equation for the  $z$ -component of vorticity  $\omega = (\nabla \times \mathbf{u}) \cdot \hat{\mathbf{z}}$ :

$$\partial_t \omega + \beta \mathbf{u} \cdot \nabla \omega = \nu \nabla^2 \omega - \alpha \omega + W, \quad (\text{C.3})$$

where  $W = (\nabla \times \mathbf{f}) \cdot \hat{\mathbf{z}}$ . The horizontal components of the velocity field  $u_x = \partial \psi / \partial y$  and  $u_y = -\partial \psi / \partial x$  can be computed using the stream function  $\psi$ , which satisfies the Poisson equation  $\nabla^2 \psi = -\omega$ .

The vorticity field  $\omega$  is discretized in the Fourier space using 128 modes along each

of the  $x$ - and  $y$ -directions. Since the lateral dimensions of the periodic domain are  $8w \times 8w$  units, the spatial resolution associated with the Fourier grid corresponds to 16 grid points per magnet width  $w$ . Taking the Fourier transform of equation (C.3), one obtains:

$$\partial_t \Omega = -\beta \mathcal{F}[\mathbf{u} \cdot \nabla \omega] + \nu \nabla^2 \Omega - \alpha \Omega + \mathcal{F}[W], \quad (\text{C.4})$$

where  $\mathcal{F}[\cdot]$  represents the Fourier transform and  $\Omega = \mathcal{F}[\omega]$ .

Equation (C.4) is stepped forward in time ( $t \rightarrow t + \Delta t$ ) using a 3-substep semi-implicit Strang-Marchuk splitting algorithm [174] where the first and last substeps advance the vorticity field using the nonlinear term by means of a second-order explicit Runge-Kutta scheme (using a time step  $\Delta t/2$ ), while the intermediate substep advances the vorticity field using the Crank-Nicholson scheme (using a time step  $\Delta t$ ). A time step of  $\Delta t = 1/32$  s has been used.

## Bibliography

- [1] H. Edelsbrunner and J. Harer, “Persistent homology—a survey,” *Contemp. Math.* **453**, 257 (2008).
- [2] E. Munch, *Applications of persistent homology to time varying systems*, PhD thesis Duke University 2013.
- [3] J. P. Richter, *The Notebooks of Leonardo da Vinci*, volume 1 (Courier, 1970), Plate 20 and Note 389.
- [4] R. Ecke, “The Turbulence Problem,” *Los Alamos Science* (2005).
- [5] O. Reynolds, “An experimental investigation of the circumstances which determine whether the motion of water shall be direct or sinuous, and of the law of resistance in parallel channels,” *P. R. Soc. London* **35**, 84 (1883).
- [6] L. D. Landau and E. M. Lifshitz, *Fluid Mechanics* (Pergamon, 1959).
- [7] J.-C. Roux, R. H. Simoyi, and H. L. Swinney, “Observation of a strange attractor,” *Physica D* **8**, 257 (1983).
- [8] F. T. Arecchi, R. Meucci, G. Puccioni, and J. Tredicce, “Experimental evidence of subharmonic bifurcations, multistability, and turbulence in a Q-switched gas laser,” *Phys. Rev. Lett.* **49**, 1217 (1982).
- [9] F. C. Moon, “Experiments on chaotic motions of a forced nonlinear oscillator: strange attractors,” *J. Appl. Mech.* **47**, 638 (1980).
- [10] P. S. Lindsay, “Period doubling and chaotic behavior in a driven anharmonic oscillator,” *Phys. Rev. Lett.* **47**, 1349 (1981).

- [11] J. Testa, J. Pérez, and C. Jeffries, “Evidence for universal chaotic behavior of a driven nonlinear oscillator,” *Phys. Rev. Lett.* **48**, 714 (1982).
- [12] L. Glass, M. R. Guevara, A. Shrier, and R. Perez, “Bifurcation and chaos in a periodically stimulated cardiac oscillator,” *Physica D* **7**, 89 (1983).
- [13] R. M. May, “Biological populations with nonoverlapping generations: stable points, stable cycles, and chaos,” *Science* **186**, 645 (1974).
- [14] Y. Kuang, *Delay differential equations: with applications in population dynamics*volume 191 (Academic Press, 1993).
- [15] T. Puu, *Attractors, bifurcations, & chaos: Nonlinear phenomena in economics* (Springer Science & Business Media, 2013).
- [16] J. D. Farmer and J. J. Sidorowich, “Predicting chaotic time series,” *Phys. Rev. Lett.* **59**, 845 (1987).
- [17] M. Casdagli, “Nonlinear prediction of chaotic time series,” *Physica D* **35**, 335 (1989).
- [18] E. Ott, C. Grebogi, and J. A. Yorke, “Controlling chaos,” *Phys. Rev. Lett.* **64**, 1196 (1990).
- [19] R. Roy, T. W. Murphy Jr., T. D. Maier, Z. Gills, and E. R. Hunt, “Dynamical control of a chaotic laser: Experimental stabilization of a globally coupled system,” *Phys. Rev. Lett.* **68**, 1259 (1992).
- [20] V. Petrov, V. Gaspar, J. Masere, and K. Showalter, “Controlling chaos in the Belousov–Zhabotinsky reaction,” *Nature* **361**, 240 (1993).
- [21] D. Ruelle and F. Takens, “On the nature of turbulence,” *Commun. Math. Phys.* **20**, 167 (1971).

- [22] J. P. Gollub and H. L. Swinney, “Onset of turbulence in a rotating fluid,” *Phys. Rev. Lett.* **35**, 927 (1975).
- [23] M. J. Feigenbaum, “Quantitative universality for a class of nonlinear transformations,” *J. Stat. Phys.* **19**, 25 (1978).
- [24] Y. Pomeau and P. Manneville, “Intermittent transition to turbulence in dissipative dynamical systems,” *Commun. Math. Phys.* **74**, 189 (1980).
- [25] P. R. Fenstermacher, H. L. Swinney, and J. P. Gollub, “Dynamical instabilities and the transition to chaotic Taylor vortex flow,” *J. Fluid Mech.* **94**, 103 (1979).
- [26] J. P. Gollub and S. V. Benson, “Many routes to turbulent convection,” *J. Fluid Mech.* **100**, 449 (1980).
- [27] P. Bergé, M. Dubois, P. Manneville, and Y. Pomeau, “Intermittency in Rayleigh-Bénard convection,” *J. Phys. Lett.-Paris* **41**, 341 (1980).
- [28] E. Hopf, “A mathematical example displaying features of turbulence,” *Commun. Pur. Appl. Math.* **1**, 303 (1948).
- [29] N. H. Packard, J. P. Crutchfield, J. D. Farmer, and R. S. Shaw, “Geometry from a time series,” *Phys. Rev. Lett.* **45**, 712 (1980).
- [30] H. Froehling, J. P. Crutchfield, D. Farmer, N. H. Packard, and R. Shaw, “On determining the dimension of chaotic flows,” *Physica D* **3**, 605 (1981).
- [31] F. Takens, *Detecting strange attractors in turbulence* (Springer, 1981).
- [32] P. Grassberger and I. Procaccia, “Characterization of strange attractors,” *Phys. Rev. Lett.* **50**, 346 (1983).
- [33] J. P. Eckmann and D. Ruelle, “Ergodic theory of chaos and strange attractors,” *Rev. Mod. Phys.* **57**, 617 (1985).

- [34] T. Sauer, J. A. Yorke, and M. Casdagli, “Embedology,” *J. Stat. Phys.* **65**, 579 (1991).
- [35] J. C. Roux, A. Rossi, S. Bachelart, and C. Vidal, “Representation of a strange attractor from an experimental study of chemical turbulence,” *Phys. Lett. A* **77**, 391 (1980).
- [36] A. Brandstater and H. L. Swinney, “Strange attractors in weakly turbulent Couette-Taylor flow,” *Phys. Rev. A* **35**, 2207 (1987).
- [37] O. Lüthje, S. Wolff, and G. Pfister, “Control of chaotic Taylor-Couette flow with time-delayed feedback,” *Phys. Rev. Lett.* **86**, 1745 (2001).
- [38] B. Malraison, P. Atten, P. Berge, and M. Dubois, “Dimension of strange attractors: an experimental determination for the chaotic regime of two convective systems,” *J. Phys. Lett.-Paris* **44**, 897 (1983).
- [39] T. Ondarçuhu, G. Mindlin, H. Mancini, and C. Perez-Garcia, “The chaotic evolution of patterns in Benard-Marangoni convection with square symmetry,” *J. Phys.-Condens. Mat.* **6**, A427 (1994).
- [40] L. Xin, H. Fei, and L. Gang, “Characteristics of chaotic attractors in atmospheric boundary-layer turbulence,” *Boundary-layer meteorology* **99**, 335 (2001).
- [41] A. Brandstater, H. L. Swinney, and G. T. Chapman, “Characterizing turbulent channel flow,” in *Dimensions and Entropies in Chaotic systems* pp. 150–157 Springer 1986.
- [42] A. M. Fraser and H. L. Swinney, “Independent coordinates for strange attractors from mutual information,” *Phys. Rev. A* **33**, 1134 (1986).

- [43] M. Casdagli, S. Eubank, J. D. Farmer, and J. Gibson, “State space reconstruction in the presence of noise,” *Physica D* **51**, 52 (1991).
- [44] E. J. Kostelich and T. Schreiber, “Noise reduction in chaotic time-series data: A survey of common methods,” *Phys. Rev. E* **48**, 1752 (1993).
- [45] S. H. Strogatz, *Nonlinear dynamics and chaos: with applications to physics, biology, chemistry, and engineering* (Westview press, 2014).
- [46] A. K. M. F. Hussain, “Coherent structures and turbulence,” *J. Fluid Mech.* **173**, 303 (1986).
- [47] J. L. Lumley, “The structure of inhomogeneous turbulent flows,” *Atmos. Turb. and Radio Wave Prop.* , 166 (1967).
- [48] P. Holmes, J. L. Lumley, and G. Berkooz, *Turbulence, coherent structures, dynamical systems and symmetry* (Cambridge, 1998).
- [49] N. Aubry, P. Holmes, J. L. Lumley, and E. Stone, “The dynamics of coherent structures in the wall region of a turbulent boundary layer,” *J. Fluid Mech.* **192**, 115 (1988).
- [50] D. Rempfer and H. F. Fasel, “Evolution of three-dimensional coherent structures in a flat-plate boundary layer,” *J. Fluid Mech.* **260**, 351 (1994).
- [51] D. Rempfer and H. F. Fasel, “Dynamics of three-dimensional coherent structures in a flat-plate boundary layer,” *J. Fluid Mech.* **275**, 257 (1994).
- [52] P. Moin and R. D. Moser, “Characteristic-eddy decomposition of turbulence in a channel,” *J. Fluid Mech.* **200**, 471 (1989).
- [53] L. Sirovich, K. S. Ball, and R. A. Handler, “Propagating structures in wall-bounded turbulent flows,” *Theor. Comp. Fluid Dyn.* **2**, 307 (1991).

- [54] L. Keefe, P. Moin, and J. Kim, “The dimension of attractors underlying periodic turbulent Poiseuille flow,” *J. Fluid Mech.* **242**, 1 (1992).
- [55] A. E. Deane, I. G. Kevrekidis, G. E. Karniadakis, and S. A. Orszag, “Low-dimensional models for complex geometry flows: Application to grooved channels and circular cylinders,” *Phys. Fluids A* **3**, 2337 (1991).
- [56] B. R. Noack, K. Afanasiev, M. Morzynski, G. Tadmor, and F. Thiele, “A hierarchy of low-dimensional models for the transient and post-transient cylinder wake,” *J. Fluid Mech.* **497**, 335 (2003).
- [57] A. Liakopoulos, P. A. Blythe, and H. Gunes, “A reduced dynamical model of convective flows in tall laterally heated cavities,” in *Proc. R. Soc. Lond. A* volume 453 pp. 663–672 The Royal Society 1997.
- [58] J. Moehlis, T. R. Smith, P. Holmes, and H. Faisst, “Models for turbulent plane Couette flow using the proper orthogonal decomposition,” *Phys. Fluids* **14**, 2493 (2002).
- [59] S. J. Kline, W. C. Reynolds, F. A. Schraub, and P. W. Runstadler, “The structure of turbulent boundary layers,” *J. Fluid Mech.* **30**, 741 (1967).
- [60] F. Waleffe, “Three-dimensional coherent states in plane shear flows,” *Phys. Rev. Lett.* **81**, 4140 (1998).
- [61] F. Waleffe, “Exact coherent structures in channel flow,” *J. Fluid Mech.* **435**, 93 (2001).
- [62] J. Jimenez, “Coherent structures and dynamical systems,” p. 323 (1987).
- [63] S. Weinberger, “What is... persistent homology?,” *Not. Am. Math. Soc.* **58**, 36 (2011).

- [64] M. Nagata, “Three-dimensional finite-amplitude solutions in plane Couette flow: bifurcation from infinity,” *J. Fluid Mech.* **217**, 519 (1990).
- [65] G. Kawahara and S. Kida, “Periodic motion embedded in plane Couette turbulence: regeneration cycle and burst,” *J. Fluid Mech.* **449**, 291 (2001).
- [66] D. Viswanath, “Recurrent motions within plane Couette turbulence,” *J. Fluid Mech.* **580**, 339 (2007).
- [67] P. Cvitanović and J. F. Gibson, “Geometry of the turbulence in wall-bounded shear flows: periodic orbits,” *Phys. Scripta* **2010**, 014007 (2010).
- [68] T. Itano and S. Toh, “The dynamics of bursting process in wall turbulence,” *J. Phys. Soc. Jpn.* **70**, 703 (2001).
- [69] H. Faisst and B. Eckhardt, “Traveling waves in pipe flow,” *Phys. Rev. Lett.* **91**, 224502 (2003).
- [70] Y. Duguet, C. C. T. Pringle, and R. R. Kerswell, “Relative periodic orbits in transitional pipe flow,” *Phys. Fluids* **20**, 114102 (2008).
- [71] A. P. Willis, P. Cvitanović, and M. Avila, “Revealing the state space of turbulent pipe flow by symmetry reduction,” *J. Fluid Mech.* **721**, 514 (2013).
- [72] B. Eckhardt, T. M. Schneider, B. Hof, and J. Westerweel, “Turbulence Transition in Pipe Flow,” *Annu. Rev. Fluid Mech.* **39**, 447 (2007).
- [73] G. Kawahara, M. Uhlmann, and L. van Veen, “The Significance of Simple Invariant Solutions in Turbulent Flows,” *Annu. Rev. Fluid Mech.* **44**, 203 (2012).
- [74] B. Hof, C. W. H. van Doorne, J. Westerweel, F. T. M. Nieuwstadt, H. Faisst, B. Eckhardt, H. Wedin, R. R. Kerswell, and F. Waleffe, “Experimental Observation of Nonlinear Traveling Waves in Turbulent Pipe Flow,” *Science* **305**, 1594 (2004).

- [75] A. de Lozar, F. Mellibovsky, M. Avila, and B. Hof, “Edge State in Pipe Flow Experiments,” *Phys. Rev. Lett.* **108**, 214502 (2012).
- [76] D. J. C. Dennis and F. M. Sogaro, “Distinct Organizational States of Fully Developed Turbulent Pipe Flow,” *Phys. Rev. Lett.* **113**, 234501 (2014).
- [77] J. F. Gibson, J. Halcrow, and P. Cvitanović, “Visualizing the geometry of state space in plane Couette flow,” *J. Fluid Mech.* **611**, 107 (2008).
- [78] J. Halcrow, J. F. Gibson, P. Cvitanović, and D. Viswanath, “Heteroclinic connections in plane Couette flow,” *J. Fluid Mech.* **621**, 365 (2009).
- [79] G. J. Chandler and R. R. Kerswell, “Invariant recurrent solutions embedded in a turbulent two-dimensional Kolmogorov flow,” *J. Fluid Mech.* **722**, 554 (2013).
- [80] D. Lucas and R. R. Kerswell, “Spatiotemporal dynamics in two-dimensional Kolmogorov flow over large domains,” *J. Fluid Mech.* **750**, 518 (2014).
- [81] D. Lucas and R. R. Kerswell, “Recurrent flow analysis in spatiotemporally chaotic 2-dimensional Kolmogorov flow,” *Phys. Fluids* **27**, 045106 (2015).
- [82] P. Cvitanović, “Recurrent flows: the clockwork behind turbulence,” *J. Fluid Mech.* **726**, 1 (2013).
- [83] CHomP, “Computational Homology Project,” 2010, Available at: <http://chomp.rutgers.edu>.
- [84] F. Chazal, L. J. Guibas, S. Y. Oudot, and P. Skraba, “Scalar field analysis over point cloud data,” *Discret. & Comput. Geom.* **46**, 743 (2011).
- [85] F. Chazal, V. De Silva, M. Glisse, and S. Oudot, “The structure and stability of persistence modules,” *arXiv preprint arXiv:1207.3674* (2012).

- [86] F. Chazal, V. De Silva, and S. Oudot, “Persistence stability for geometric complexes,” *Geometriae Dedicata* **173**, 193 (2014).
- [87] P. Bubenik and J. A. Scott, “Categorification of persistent homology,” *Discrete & Comput. Geom.* **51**, 600 (2014).
- [88] K. Krishan, H. Kurtuldu, M. F. Schatz, M. Gameiro, K. Mischaikow, and S. Madruga, “Homology and symmetry breaking in Rayleigh-Bénard convection: Experiments and simulations,” *Phys. Fluids* **19**, 117105 (2007).
- [89] H. Kurtuldu, K. Mischaikow, and M. F. Schatz, “Measuring the departures from the Boussinesq approximation in Rayleigh-Bénard convection experiments,” *J. Fluid Mech.* **682**, 543 (2011).
- [90] H. Kurtuldu, K. Mischaikow, and M. F. Schatz, “Extensive scaling from computational homology and Karhunen-Loeve decomposition analysis of Rayleigh-Bénard convection experiments,” *Phys. Rev. Lett.* **107**, 034503 (2011).
- [91] J. Huang, J. Xu, X. Sang, H. Wang, and H. Wang, “Quantifying the synergy of bubble swarm patterns and heat transfer performance using computational homology,” *Int. J. Heat Mass Tran.* **75**, 497 (2014).
- [92] B. A. Carreras, I. Llerena, L. Garcia, and I. Calvo, “Topological characterization of flow structures in resistive pressure-gradient-driven turbulence,” *Phys. Rev. E* **78**, 066402 (2008).
- [93] L. Garcia, B. A. Carreras, I. Llerena, and I. Calvo, “Topological characterization of the transition from laminar regime to fully developed turbulence in the resistive pressure-gradient-driven turbulence model,” *Phys. Rev. E* **80**, 046410 (2009).

- [94] D. Laney, P.-T. Bremer, A. Mascarenhas, P. Miller, and V. Pascucci, “Understanding the structure of the turbulent mixing layer in hydrodynamic instabilities,” *IEEE Trans. Vis. Comput. Graph.* **13**, 1053 (2006).
- [95] S. Kulp, C. Chen, D. Metaxas, and L. Axel, “Ventricular blood flow analysis using topological methods,” in *2015 IEEE 12th Int. Symp. on Biomed. Imag.* pp. 663–666 IEEE 2015.
- [96] M. Kramár, R. Levanger, J. Tithof, B. Suri, M. Xu, M. Paul, M. F. Schatz, and K. Mischaikow, “Analysis of Kolmogorov flow and Rayleigh-Bénard convection using persistent homology,” *Physica D* (2016).
- [97] P. Cvitanović, D. Borrero-Echeverry, K. M. Carroll, B. Robbins, and E. Siminos, “Cartography of high-dimensional flows: A visual guide to sections and slices,” *Chaos* **22**, 047506 (2012).
- [98] D. G. Dritschel and B. Legras, “Modeling oceanic and atmospheric vortices,” *Phys. Today* **46**, 44 (2008).
- [99] V. I. Arnold and L. D. Meshalkin, “Seminar led by A. N. Kolmogorov on selected problems of analysis (1958-1959),” *Usp. Mat. Nauk* **15**, 20 (1960).
- [100] F. V. Dolzhanskii, V. A. Krymov, and D. Y. Manin, “Stability and vortex structures of quasi-two-dimensional shear flows,” *Sov. Phys. Usp.* **33**, 495 (1990).
- [101] N. F. Bondarenko, M. Z. Gak, and F. V. Dolzhanskiy, “Laboratory and theoretical models of plane periodic flows,” *Izv. Akad. Nauk SSSR, Fiz. Atmos. Okeana* **15**, 711 (1979).
- [102] L. J. Campbell and R. M. Ziff, “Vortex patterns and energies in a rotating superfluid,” *Phys. Rev. B* **20**, 1886 (1979).

- [103] J. Sommeria and R. Moreau, “Why, how, and when, MHD turbulence becomes two-dimensional,” *J. Fluid Mech.* **118**, 507 (1982).
- [104] A. Pothérat, “Three-dimensionality in quasi-two-dimensional flows: Recirculations and Barrel effects,” *Europhys. Lett.* **98**, 64003 (2012).
- [105] Y. Couder, “Two-dimensional grid turbulence in a thin liquid film,” *J. Phys. Lett.* **45**, 353 (1984).
- [106] T. B. Mitchell, C. F. Driscoll, and K. S. Fine, “Experiments on stability of equilibria of two vortices in a cylindrical trap,” *Phys. Rev. Lett.* **71**, 1371 (1993).
- [107] L. D. Meshalkin and I. G. Sinai, “Investigation of the stability of a stationary solution of a system of equations for the plane movement of an incompressible viscous liquid,” *J. Appl. Math. Mech.* **25**, 1700 (1961).
- [108] V. I. Iudovich, “Example of the generation of a secondary stationary or periodic flow when there is loss of stability of the laminar flow of a viscous incompressible fluid,” *J. Appl. Math. Mech.* **29**, 527 (1965).
- [109] V. I. Kliatskin, “On the nonlinear theory of stability of periodic flows,” *J. Appl. Math. Mech.* **36**, 243 (1972).
- [110] A. A. Nepomniashchii, “On stability of secondary flows of a viscous fluid in unbounded space,” *J. Appl. Math. Mech.* **40**, 886 (1976).
- [111] J. S. A. Green, “Two-dimensional turbulence near the viscous limit,” *J. Fluid Mech.* **62**, 273 (1974).
- [112] D. Armbruster, R. Heiland, E. J. Kostelich, and B. Nicolaenko, “Phase-space analysis of bursting behavior in Kolmogorov flow,” *Physica D* **58**, 392 (1992).
- [113] N. Smaoui, “A Model for the Unstable Manifold of the Bursting Behavior in the 2D Navier–Stokes Flow,” *SIAM J. Sci. Comp.* **23**, 824 (2001).

- [114] J. M. Burgess, C. Bizon, W. D. McCormick, J. B. Swift, and H. L. Swinney, “Instability of the Kolmogorov flow in a soap film,” *Phys. Rev. E* **60**, 715 (1999).
- [115] E. B. Gledzer, F. V. Dolzhanskii, and A. M. Obukhov, “Hydrodynamic-Type Systems and Their Applications,” 1981.
- [116] A. M. Batchaev and V. A. Dowzhenko, “Experimental modeling of stability loss in periodic zonal flows,” in *Dokl. Akad. Nauk* volume 273 p. 582 1983.
- [117] Y. Kolesnikov, “Investigation of flat shear flow instability in a magnetic field,” *Magn. Gidrodin.* **1**, 60 (1985).
- [118] Y. B. Kolesnikov, *Instabilities and turbulence in liquid metal magnetohydrodynamics*, PhD thesis University of Riga 1985.
- [119] A. M. Batchaev and V. M. Ponomarev, “Experimental and theoretical investigation of Kolmogorov flow on a cylindrical surface,” *Fluid Dyn.* **24**, 675 (1989).
- [120] P. Tabeling, O. Cardoso, and B. Perrin, “Chaos in a linear array of vortices,” *J. Fluid Mech.* **213**, 511 (1990).
- [121] P. Tabeling, S. Burkhardt, O. Cardoso, and H. Willaime, “Experimental study of freely decaying two-dimensional turbulence,” *Phys. Rev. Lett.* **67**, 3772 (1991).
- [122] O. Cardoso, D. Marteau, and P. Tabeling, “Quantitative experimental study of the free decay of quasi-two-dimensional turbulence,” *Phys. Rev. E* **49**, 454 (1994).
- [123] H. J. H. Clercx, G. J. F. Van Heijst, and M. L. Zoeteweij, “Quasi-two-dimensional turbulence in shallow fluid layers: the role of bottom friction and fluid layer depth,” *Phys. Rev. E* **67**, 066303 (2003).

- [124] R. A. D. Akkermans, A. R. Cieslik, L. P. J. Kamp, R. R. Trieling, H. J. H. Clercx, and G. J. F. van Heijst, “The three-dimensional structure of an electromagnetically generated dipolar vortex in a shallow fluid layer,” *Phys. Fluids* **20**, 116601 (2008).
- [125] L. Rossi, S. Bocquet, S. Ferrari, J. M. G. de la Cruz, and S. Lardeau, “Control of flow geometry using electromagnetic body forcing,” *Int. J. Heat Fluid Fl.* **30**, 505 (2009).
- [126] A. Figueroa, F. Demiaux, S. Cuevas, and E. Ramos, “Electrically driven vortices in a weak dipolar magnetic field in a shallow electrolytic layer,” *J. Fluid Mech.* **641**, 245 (2009).
- [127] D. H. Kelley and N. T. Ouellette, “Using particle tracking to measure flow instabilities in an undergraduate laboratory experiment,” *Am. J. Phys.* **79**, 267 (2011).
- [128] T. H. Solomon and I. Mezić, “Uniform resonant chaotic mixing in fluid flows,” *Nature* **425**, 376 (2003).
- [129] D. H. Kelley and N. T. Ouellette, “Onset of three-dimensionality in electromagnetically driven thin-layer flows,” *Phys. Fluids* **23**, 045103 (2011).
- [130] D. Marteau, O. Cardoso, and P. Tabeling, “Equilibrium states of two-dimensional turbulence: An experimental study,” *Phys. Rev. E* **51**, 5124 (1995).
- [131] B. S. Williams, D. Marteau, and J. P. Gollub, “Mixing of a passive scalar in magnetically forced two-dimensional turbulence,” *Phys. Fluids* **9**, 2061 (1997).
- [132] D. Rothstein, E. Henry, and J. P. Gollub, “Persistent patterns in transient chaotic fluid mixing,” *Nature* **401**, 770 (1999).

- [133] G. A. Voth, G. Haller, and J. P. Gollub, “Experimental measurements of stretching fields in fluid mixing,” *Phys. Rev. Lett.* **88**, 254501 (2002).
- [134] N. T. Ouellette, P. J. J. OMalley, and J. P. Gollub, “Transport of finite-sized particles in chaotic flow,” *Phys. Rev. Lett.* **101**, 174504 (2008).
- [135] D. H. Kelley and N. T. Ouellette, “Separating stretching from folding in fluid mixing,” *Nat. Phys.* **7**, 477 (2011).
- [136] D. H. Kelley, M. R. Allshouse, and N. T. Ouellette, “Lagrangian coherent structures separate dynamically distinct regions in fluid flows,” *Phys. Rev. E* **88**, 013017 (2013).
- [137] J. Paret and P. Tabeling, “Experimental Observation of the Two-Dimensional Inverse Energy Cascade,” *Phys. Rev. Lett.* **79**, 4162 (1997).
- [138] M.-C. Jullien, J. Paret, and P. Tabeling, “Richardson pair dispersion in two-dimensional turbulence,” *Phys. Rev. Lett.* **82**, 2872 (1999).
- [139] G. Boffetta, A. Cenedese, S. Espa, and S. Musacchio, “Effects of friction on 2D turbulence: An experimental study of the direct cascade,” *Europhys. Lett.* **71**, 590 (2005).
- [140] M. K. Rivera and R. E. Ecke, “Pair Dispersion and Doubling Time Statistics in Two-Dimensional Turbulence,” *Phys. Rev. Lett.* **95**, 194503 (2005).
- [141] M. J. Twardos, P. E. Arratia, M. K. Rivera, G. A. Voth, J. P. Gollub, and R. E. Ecke, “Stretching fields and mixing near the transition to nonperiodic two-dimensional flow,” *Phys. Rev. E* **77**, 056315 (2008).
- [142] S. Chen, R. E. Ecke, G. L. Eyink, M. Rivera, M. Wan, and Z. Xiao, “Physical mechanism of the two-dimensional inverse energy cascade,” *Phys. Rev. Lett.* **96**, 084502 (2006).

- [143] M. K. Rivera and R. E. Ecke, “Lagrangian statistics in weakly forced two-dimensional turbulence,” *Chaos* **26**, 013103 (2016).
- [144] B. Jüttner, D. Marteau, P. Tabeling, and A. Thess, “Numerical simulations of experiments on quasi-two-dimensional turbulence,” *Phys. Rev. E* **55**, 5479 (1997).
- [145] M. P. Satijn, A. W. Cense, R. Verzicco, H. J. H. Clercx, and G. J. F. van Heijst, “Three-dimensional structure and decay properties of vortices in shallow fluid layers,” *Phys. Fluids* **13**, 1932 (2001).
- [146] R. A. D. Akkermans, L. P. J. Kamp, H. J. H. Clercx, and G. J. F. Van Heijst, “Intrinsic three-dimensionality in electromagnetically driven shallow flows,” *Europhys. Lett.* **83**, 24001 (2008).
- [147] R. A. D. Akkermans, L. P. J. Kamp, H. J. H. Clercx, and G. J. F. van Heijst, “Three-dimensional flow in electromagnetically driven shallow two-layer fluids,” *Phys. Rev. E* **82**, 026314 (2010).
- [148] R. J. Adrian and J. Westerweel, *Particle image velocimetry* (Cambridge, 2011).
- [149] M. Raffel, C. E. Willert, and J. Kompenhans, *Particle image velocimetry: A practical guide* (Springer, 2013).
- [150] A. Eckstein and P. P. Vlachos, “Digital particle image velocimetry (DPIV) robust phase correlation,” *Meas. Sci. Technol.* **20**, 055401 (2009).
- [151] B. Drew, J. Charonko, and P. P. Vlachos, “QI – Quantitative Imaging (PIV and more),” 2013, Software available at <http://sourceforge.net/projects/qi-tools/>.
- [152] M. Shats, D. Byrne, and H. Xia, “Turbulence decay rate as a measure of flow dimensionality,” *Phys. Rev. Lett.* **105**, 264501 (2010).

- [153] G. Boffetta and R. E. Ecke, “Two-dimensional turbulence,” *Annu. Rev. Fluid Mech.* **44**, 427 (2012).
- [154] B. Suri, J. Tithof, R. Mitchell, R. O. Grigoriev, and M. F. Schatz, “Velocity profile in a two-layer Kolmogorov-like flow,” *Phys. Fluids* **26**, 053601 (2014).
- [155] V. A. Dovzhenko, A. M. Obukhov, and V. M. Ponomarev, “Generation of vortices in an axisymmetric shear flow,” *Fluid Dyn.* **16**, 510 (1981).
- [156] A. Thess, “Instabilities in two-dimensional spatially periodic flows. Part I: Kolmogorov flow,” *Phys. Fluids A* **4**, 1385 (1992).
- [157] R. Mitchell, *Transition to turbulence and mixing in a quasi-two-dimensional Lorentz force-driven Kolmogorov flow*, PhD thesis Georgia Institute of Technology 2013.
- [158] S. Armfield and R. Street, “The Fractional-Step Method for the Navier-Stokes Equations on Staggered Grids: The Accuracy of Three Variations,” *J. Comput. Phys.* **153**, 660 (1999).
- [159] A. M. Obukhov, “Kolmogorov flow and laboratory simulation of it,” *Russ. Math. Surv.* **38**, 113 (1983).
- [160] F. V. Dolzhansky and B. Khesin, *Fundamentals of geophysical hydrodynamics* volume 103 (Springer Science & Business Media, 2012).
- [161] J. Tithof, B. Suri, R. Pallantla, R. O. Grigoriev, and M. F. Schatz, “Bifurcations in a Quasi-Two-Dimensional Kolmogorov-Like Flow,” *In preparation for submission to J. Fluid Mech.* (2016), Available at <http://arXiv.org/abs/1601.00243>.
- [162] R. Temam, “Inertial manifolds,” *Math. Intell.* **12**, 68 (1990).

- [163] B. Legras and M. Ghil, “Persistent anomalies, blocking and variations in atmospheric predictability,” *J. Atmos. Sci.* **42**, 433 (1985).
- [164] C. Kelley, *Solving Nonlinear Equations with Newton’s Method* (SIAM, 2003) <http://epubs.siam.org/doi/pdf/10.1137/1.9780898718898>.
- [165] R. L. Panton, *Incompressible flow* (John Wiley & Sons, 2006).
- [166] V. Nanda, “Perseus, the Persistent Homology Software,” 2015, Software available at <http://www.sas.upenn.edu/~vnanda/perseus/>.
- [167] H. Edelsbrunner and J. L. Harer, *Computational topology* (American Mathematical Society, 2010).
- [168] M. Kramar, A. Goullet, L. Kondic, and K. Mischaikow, “Quantifying force networks in particulate systems,” *Physica D* **283**, 37 (2014).
- [169] K. Mischaikow and V. Nanda, “Morse theory for filtrations and efficient computation of persistent homology,” *Discret. & Comput. Geom.* **50**, 330 (2013).
- [170] P. Cvitanović, R. Artuso, R. Mainieri, G. Tanner, and G. Vattay, *Chaos: Classical and Quantum* (Niels Bohr Institute, Copenhagen, 2012), <http://ChaosBook.org>.
- [171] Y. Lan, “Cycle expansions: From maps to turbulence,” *Commun. Nonlinear Sci. Sci.* **15**, 502 (2010).
- [172] F. H. Harlow and J. E. Welch, “Numerical Calculation of Time Dependent Viscous Incompressible Flow of Fluid with Free Surface,” *Phys. Fluids* **8**, 2182 (1965).
- [173] M. Griebel, T. Dornseifer, and T. Neunhoeffer, *Numerical Simulation in Fluid Dynamics* (SIAM, 1998) <http://epubs.siam.org/doi/pdf/10.1137/1.9780898719703>.

- [174] U. M. Ascher, S. J. Ruuth, and B. T. R. Wetton, “Implicit-explicit methods for time-dependent partial differential equations,” *SIAM J. Numer. Anal.* **32**, 797 (1995).